SIGNIFICANT SHEAR STRESSES AND VELOCITY DISTRIBUTION IN ARRESTED SALINE WEDGES

By

VASSILIOS DERMISSIS

A DISSERTATION PRESENTED TO THE GRADUATE SCHOOL
OF THE UNIVERSITY OF FLORIDA
IN PARTIAL FULFILLMENT OF THE REQUIREMENTS
FOR THE DEGREE OF DOCTOR OF PHILOSOPHY

UNIVERSITY OF FLORIDA

1984

Copyright 1984

by

Vassilios Dermissis

to my wife Nikoula

and

my daughter Sophia

ACKNOWLEDGMENTS

The primary support for this study was provided by the National Science Foundation under Grant No. ENG. 76-11537. This support is gratefully acknowledged.

Dr. E. Partheniades, professor of engineering sciences at the University of Florida in Gainesville and professor of hydraulic structures at the Aristoteles University of Thessaloniki in Greece, was the project supervisor. I wish to thank him sincerely for his continuous support, encouragement, and personal interest.

Next, I wish to acknowledge the contribution of Dr. Cheng-Han Tsai for his assistance in carrying out the experiments.

Thanks are due to Messrs. George Jones, Vernon Sparkman, and the Coastal Engineering Laboratory staff of the University of Florida for constructing the apparatus and for their valuable assistance and contributions during the experiments.

I wish also to thank Mrs. Anna Kiriakidou, Mrs. Danae Polyzoe, and Mrs. Stella Ioakimidou, staff of the University of Thessaloniki, for the typing of the manuscript and drafting of the graphs. Also I would like to thank Miss Sofia Kohli for the typing of the final text.

In conclusion, I wish to express my deep appreciation and thanks to my wife, Nikoula, for her moral support and for doing her best to contribute to the final stages of this dissertation. The patience of my daughter, Sophia, should finally be acknowledged.

TABLE OF CONTENTS

		Page
ACKNOWLEDGMENTS		iv
LIST OF TABLES		vii
LIST OF FIGURES		viii
LIST OF SYMBOLS		xv
ABSTRACT		xviii
CHAPTER		
I	INTRODUCTION	1
II	BACKGROUND AND REVIEW OF EARLIER INVESTIGATIONS	6
	2.1 Basic Parameters	6
	2.2 Mixing Mechanisms and Density Interface	9
	2.3 Velocity Interface	10
	2.4 Review and Discussion of Earlier Investigations	10
	2.4.1 The Interfacial Friction Coefficient	10
	2.4.2 Bed Shear Stresses in Arrested Saline Wedge	32
	2.4.3 Velocity Profiles at the Interfacial Zone	32
III	THEORETICAL BACKGROUND	39
	3.1 Fundamental Equations	30
	3.2 The One-Dimensional Model	43
	3.3 Integration of the Equations of Motion: Complete Intrusion	49
	3.4 Integration of the Equations of Motion: Partial Intrusion	57
IV	EXPERIMENTAL APPARATUS AND INSTRUMENTATION	66
	4.1 Introduction	66
	4.2 The Main Experimental Apparatus	66
	4.3 Instrumentation	75

CHAPTER Page

V EXPERIMENTAL PROCEDURE AND CALIBRATION OF THE INSTRUMENTS 83

5.1 Introduction 83
5.2 Preparation of the Salt Water in Tank T_1 84
5.3 Calibrations 86
5.4 The placing of the Instruments on the Carriage 94
5.5 Experiments 96

VI ANALYSIS OF EXPERIMENTAL DATA 106

6.1 Introduction 106
6.2 Density Distribution Law 106
6.3 Velocity Distribution 109
6.4 Laws of Variation of Interfacial and Bed Friction Coefficients 125
6.5 Velocity Distribution Laws 163

VII SUMMARY AND CONCLUSIONS 181

APPENDIX 191

REFERENCES 219

BIOGRAPHICAL SKETCH 223

LIST OF TABLES

Table		Page
1	Grouping of experiments	112
2	Values of parameters introduced in Equation (3.4.16)	142
3	Correlation of k and c coefficients with the flow and salinity parameters	174
4	Geometrical and flow parameters of each experiment	193

LIST OF FIGURES

Figure		Page
2.1	Gravity flow in a two-layered system	7
2.2	The effect of width of interfacial zone on the Richardson number	11
2.3	Arrested saline wedge	13
2.4	Mean interfacial shear stresses	13
2.5	Mean shear stresses at the bottom	16
2.6	Variation of $2T_i/\rho V_0^2$ and $2T_0/\rho V_0^2$ with Reynolds number	16
2.7	Correlation of f_i with Reynolds number for upper layer motion and semi-stagnant lower layer	18
2.8	Correlation of f_i with Reynolds number for underflows	19
2.9	Variation of f_i with $ReFr^2$ and $\Delta\rho/\rho$	20
2.10	Extrapolation of the $\Delta\rho/\rho = 0.020$ line of Figure 2.9 and comparison with earlier laboratory and field data	21
2.11	Tentative extrapolation of the curves of Figure 2.9	23
2.12	Variation of the average f_i for underflows according to Lofquist's experimental data	29
2.13	Variation of the average f_i for underflows according to Lofquist's experimental data	29
2.14	Velocity profile	33
2.15	Normalized mean velocity profile from Powell's data	35

Figure		Page
2.16	Velocity distribution in a cross section of arrested saline wedge, after Keulegan	37
3.1	Definition sketch of an arrested saline wedge	44
3.2	Dimensionless shape of arrested saline wedges	54
3.3	Variation of the integrals I with respect to Fr_0'	58
3.4	Definition sketch for partial intrusion of an arrested saline wedge	61
4.1	Main experimental apparatus	69
4.2	Downstream side of the apparatus	70
4.3	Front view of the apparatus	70
4.4	Rear view of the apparatus	71
4.5	Rear view of the apparatus with gate	71
4.6	Rear view of the apparatus showing the laser instrument	76
4.7	Black box schematic outline of instrumentation	77
4.8	Outline of electronic instrumentation	78
4.9	Cross-section of conductivity probe	80
5.1	Calibration curve for the thermistor	87
5.2	Calibration of hot film sensors	89
5.3	Instruments used for calibration of thermistor and sensor	90
5.4	Calibration curves for the conductivity probe for various temperatures	91
5.5	Calibration of the conductivity probe for T = 20.4°C	92
5.6	Calibration of the conductivity probe for $\Delta\rho/(\rho + \Delta\rho)$ up to 85 °/oo	97

Figure		Page
5.7	Orifice calibration curve for D = 2.5 cm	95
5.8	Establishment of bottom elevation of the channel before starting the experiments	97
5.9	Upstream motion of salt water front	99
5.10	Example of smooth interface	99
5.11	Example of wavy interface	101
5.12	(a) Eddy formation due to the interfacial wave breaking; (b) beginning of gradual mixing of the two layers	102
6.1	Defintion sketch for the interfacial zone	108
6.2	Nondimensional density distribution, Powell's data	110
6.3	Nondimensional density distribution (data from present study)	111
6.4	Definition sketch for velocity profiles	114
6.5	Dimensionless velocity distribution	116
6.6	Dimensionless velocity distribution $[\Delta\rho/(\rho + \Delta\rho) \leq 20\ ^{o}/_{oo}]$	117
6.7	Dimensionless velocity distribution $[\Delta\rho/(\rho + \Delta\rho) > 20\ ^{o}/_{oo}]$	118
6.8	Dimensionless velocity distribution (data from Figure 6.5)	120
6.9	Dimensionless velocity distribution (data from Figures 6.6 and 6.7)	121
6.10	Dimensionless velocity distribution in the immediate neighborhood of velocity interface, for $\Delta\rho/(\rho + \Delta\rho) \leq 20\ ^{o}/_{oo}$	123
6.11	Dimensionless velocity distribution in the immediate neighborhood of velocity interface, for $\Delta\rho/(\rho + \Delta\rho) > 20\ ^{o}/_{oo}$	124

Figure		Page
6.12	Dimensionless velocity distribution outside of the linear zone (group 1)	126
6.13	Dimensionless velocity distribution outside of the linear zone (group 2)	127
6.14	Dimensionless velocity distribution outside of the linear zone (group 3)	128
6.15	Dimensionless velocity distribution outside of the linear zone (group 4)	129
6.16	Dimensionless velocity distribution outside of the linear zone (group 5)	130
6.17	Dimensionless velocity distribution outside of the linear zone (group 6)	131
6.18	Dimensionless velocity distribution outside of the linear zone (group 7)	132
6.19	Dimensionless velocity distribution outside of the linear zone (group 8)	133
6.20	Definition sketch for the velocity distribution laws	136
6.21	Dimensionless values of Reynolds and viscous stresses for $\Delta\rho/(\rho + \Delta\rho) \leq 20$ $^{o}/_{oo}$	139
6.22	Dimensionless values of Reynolds and viscous stresses for $\Delta\rho/(\rho + \Delta\rho) > 20$ $^{o}/_{oo}$	141
6.23	Correlation of f_i with $ReFr^2$ and $[\overline{(\Delta\rho)/(\rho + \Delta\rho)}]$ (group 1)	148
6.24	Correlation of f_i with $ReFr^2$ and $[\overline{(\Delta\rho)/(\rho + \Delta\rho)}]$ (group 2)	149
6.25	Correlation of f_i with $ReFr^2$ and $[\overline{(\Delta\rho)/(\rho + \Delta\rho)}]$ (group 3)	150
6.26	Correlation of f_i with $ReFr^2$ and $[\overline{(\Delta\rho)/(\rho + \Delta\rho)}]$ (group 4)	151
6.27	Correlation of f_i with $ReFr^2$ and $[\overline{(\Delta\rho)/(\rho + \Delta\rho)}]$ (group 5)	152

Figure		Page
6.28	Correlation of f_i with $ReFr^2$ and $[\overline{(\Delta\rho)/(\rho + \Delta\rho)}]$ (group 6)	153
6.29	Correlation of f_i with $ReFr^2$ and $[\overline{(\Delta\rho)/(\rho + \Delta\rho)}]$ (group 7)	154
6.30	Correlation of f_i with $ReFr^2$ and $[\overline{(\Delta\rho)/(\rho + \Delta\rho)}]$ (group 8)	155
6.31	Variation of f_i with $ReFr^2$ and $[\overline{(\Delta\rho)/(\rho + \Delta\rho)}]$ for $T_0 \neq 0$	156
6.32	Variation of f_i with $ReFr^2$ and $[\overline{(\Delta\rho)/(\rho + \Delta\rho)}]$ for $T = 0$	157
6.33	Comparison of data from other investigations with the corresponding data of the present study	158
6.34	Variation of T_0/T_i with $ReFr^2$	161
6.35	Variation of f_0 with $ReFr^2$ and $[\overline{(\Delta\rho)/(\rho + \Delta\rho)}]$	162
6.36	Dimensionless velocity distribution outside of the linear zone (group 1)	164
6.37	Dimensionless velocity distribution outside of the linear zone (group 2)	165
6.38	Dimensionless velocity distribution outside of the linear zone (group 3)	166
6.39	Dimensionless velocity distribution outside of the linear zone (group 4)	167
6.40	Dimensionless velocity distribution outside of the linear zone (group 5)	168
6.41	Dimensionless velocity distribution outside of the linear zone (group 6)	169
6.42	Dimensionless velocity distribution outside of the linear zone (group 7)	170
6.43	Dimensionless velocity distribution outside of the linear zone (group 8)	171
6.44	Correlation of k_2 with the flow and salinity parameters	177

Figure		Page
6.45	Correlation of k_3 with the flow and salinity parameters	178
6.46	Correlation of k_2 and k_3 with c_2 and c_3	179
A.1	Dimensional velocity distribution (experiments S_1 and S_2)	200
A.2	Dimensional velocity distribution (experiment S_4)	201
A.3	Dimensional velocity distribution (experiments U_4 and U_5)	202
A.4	Dimensional velocity distribution (experiment AA_1)	203
A.5	Dimensional velocity distribution (experiment AA_2)	204
A.6	Dimensionless velocity distribution outside of the linear zone (experiment S_1)	205
A.7	Dimensionless velocity distribution outside of the linear zone (experiment S_2)	206
A.8	Dimensionless velocity distribution outside of the linear zone (experiment S_4)	207
A.9	Dimensionless velocity distribution outside of the linear zone (experiment U_4)	208
A.10	Dimensionless velocity distribution outside of the linear zone (experiment U_5)	209
A.11	Dimensionless velocity distribution outside of the linear zone (experiment AA_1)	210
A.12	Dimensionless velocity distribution outside of the linear zone (experiment AA_2)	211
A.13	Dimensionless velocity distribution outside of the linear zone (experiment S_1)	212
A.14	Dimensionless velocity distribution outside of the linear zone (experiment S_2)	213
A.15	Dimensionless velocity distribution outside of the linear zone (experiment S_4)	214

Figure		Page
A.16	Dimensionless velocity distribution outside of the linear zone (experiment U_4)	215
A.17	Dimensionless velocity distribution outside of the linear zone (experiment U_5)	216
A.18	Dimensionless velocity distribution outside of the linear zone (experiment AA_1)	217
A.19	Dimensionless velocity distribution outside of the linear zone (experiment AA_2)	218

LIST OF SYMBOLS

Symbols	Definition
A	Cross-section
a	Constant
b	Width of channel or constant
c	Constant
D	Diameter of pipe
E	Voltage
f	Friction coefficient
Fr	Froude number
g	Gravitational acceleration
H	Piezometric head
h	Depth of water
I	Integral depended on densimetric Froude number
K	Keulegan number
L	Length of arrested saline wedge (complete intrusion)
L_0	Length of arrested saline wedge (partial intrusion)
P	Pressure
p	Time averaged pressure
p_0	Pressure of reference
Q	Flow rate
R	Correlation coefficient or electric resistance

Symbol	Definition
Re	Reynolds number
Ri	Richardson number
R_h	Hydraulic radius
S_0	Slope of the bottom of the channel
T	Average shear stresses or temperature
U	Free surface velocity
u,v,w	Components of velocity in Cartesian coordinates
u_*	Friction velocity
V	Cross-sectional velocity
y_0	Distance between the bottom and the velocity interface ($y_0 = h_s + \eta$)
z_0	Height of the bottom of channel above datum
α,β	Momentum correction coefficients
ΔH	Piezometric head difference
$\Delta\rho$	Density difference
δ	Interfacial zone width
δu	Distance between the velocity interface and the upper limit of the zone of shear flow
δu_1	Distance between the velocity interface and the lower inflection point of the velocity distribution curve
δu_2	Sum of δu and δu_1
ε	$\varepsilon = 5\delta u_1$ or $\varepsilon = V_i/V_1$
η	Distance between the velocity and the density interface
κ	Von Karman's Constant
λ	$\lambda = (T_0/T_i) + 1$

Symbols	Definition
μ	Dynamic viscosity
ν	Kinematic viscosity
$\tilde{\rho}$	Fluid density
ρ_{ℓ}	Time averaged local density
τ	Shear stresses
0	(subscript) Upstream quantity
1	(subscript) Upper layer quantity
c	(subscript) Critical quantity
i	(subscript) Interfacial quantity
ℓ	(subscript) Local quantity
s	(subscript) Lower layer quantity
w	(subscript) Wall quantity
-	(above symbol) Average over x direction
'	(superscript) Densimetric quantity or fluctuating quantity about the mean

Abstract of Dissertation Presented to the Graduate School
of the University of Florida in Partial Fulfillment of the
Requirements for the Degree of Doctor of Philosophy

SIGNIFICANT SHEAR STRESSES AND VELOCITY DISTRIBUTION IN ARRESTED SALINE WEDGES

By

Vassilios Dermissis

April 1984

Chairman: E. Partheniades
Major Department: Engineering Sciences

The objective of the present study is the systematic experimental investigation of interfacial and bed shear stresses together with the shear flow structure of an arrested saline wedge. A special experimental apparatus was used. This apparatus was designed at the Aristoteles University of Thessaloniki in Greece and at the University of Florida in Gainesville and was constructed at the Coastal and Oceanographic Engineering Laboratory of the latter university. The apparatus consists of an open tilting flume 45.7 cm wide, 45.7 cm deep, and 20.24 m long, supplemented with all the pertinent units for the formation of arrested saline wedges over a large range of flow and salinity conditions. The apparatus was equipped with a constant temperature hot film anemometer, a high resolution electronic conductivity meter, and some other instruments for operation and measurements.

A number of 74 experiments have been carried out. The analysis of the experimental results led to the following conclusions: (1) The best correlation of the interfacial and bed friction coefficients with the flow parameters and fluid properties has been obtained when these coefficients were plotted against the dimensionless parameter $ReFr^2$, where Re is the Reynolds number and Fr is the nondensimetric Froude number, with the relative density difference $\Delta\rho/(\rho + \Delta\rho)$ as an independent parameter. (2) The ratio of interfacial and bed shear stresses is independent of $\Delta\rho/(\rho + \Delta\rho)$. (3) Within a core of about 4 mm thickness, in the interfacial zone, the nondimensional velocity distribution is linear. (4) Outside the linear zone the velocity distribution law for the two layers is logarithmic. In these zones we distinguish the law of interface and the law of the outer region, corresponding to wall law and outer region law for fixed boundaries, respectively.

CHAPTER I
INTRODUCTION

Density stratification occurs in the atmosphere, oceans, lakes, estuaries, rivers, and reservoirs as a result of compressibility, heat, dissolved salts, and suspended matter. It can be natural or induced by man-made activities, such as discharge of heated water and other effluents. The induced density differences may strongly affect the dynamics of the system as well as its dispersive and transport properties; therefore, they play a dominant role in the environmental quality control.

Density stratification can be either continuous or discontinuous. In the latter case the system is composed of a finite number of distinct layers of constant density separated by relatively thin zones of sharp density gradients. For modeling purposes these zones are normally simulated by surfaces through which densities and sometimes velocities are assumed to vary discontinuously. The simplest two-layered system has been extensively studied for two reasons: first, a large number of natural systems and problems in the domain of hydraulic, coastal, and environmental engineering can be simulated and treated as two-layered systems; second, its study can often lead to an understanding and mathematical formulation of more complicated cases. Some of the most common occurrences of stratified flows are the warm and salinity wedges, the formation and evolution of the thermocline in oceans and lakes, the lock exchange flow, the density and turbidity currents in estuaries, oceans,

and lakes and the motion of fluid fronts. In this study the term "stratified flow" refers to the two-layered system and the interface is considered as a thin zone of finite width.

In the modeling of stratified flow systems and in the analysis of the associated problems, the interfacial shear stresses, τ_i, as well as the associated coefficient, f_i, has to be introduced. For this reason, τ_i and f_i have been studied extensively during the last thirty years through theoretical analysis, laboratory research, and field investigations. Some of these studies aimed at a mere correlation of f_i with the pertinent gross flow parameters and fluid properties, while some others concentrated in the detailed flow structure on the neighborhood and within the interfacial zone. The first group of studies resulted in a number of semi-empirical laws for f_i. The application of these laws to laboratory and field data obtained by other investigations leads, sometimes, to values of f_i which may differ by orders of magnitude. The reason for these discrepancies lies in the basic assumptions, the methodology of approach, and the range of variation of the controlling parameters. The reliability of the up to 1975 semi-empirical laws for f_i and the derivation of a relationship of general validity linking the interfacial friction coefficient, f_i, to the pertinent gross flow and density parameters were the main objectives of the author's doctoral dissertation [11],* which for the first time led to satisfactory generalized correlations for f_i.

Stratified flows can be divided into the following three general types:

---

*Numbers in brackets indicate references at the end of the dissertation.

a. Flow of lighter fluid over a quasi-stagnant denser fluid, as in the case of arrested saline wedges in stratified estuaries

b. Flow of heavier fluid under a quasi-stagnant lighter fluid, as in arrested thermal wedges in rivers and estuaries, in density and turbidity currents in oceans, lakes, and reservoirs, and in advancing density fronts

c. Motion of both layers in opposite directions, as in the case of lock exchange flow (counter flow)

The hydrodynamic behavior of arrested saline wedges has been theoretically and experimentally studied in the last thirty years. Among the best known studies are Schijf and Schönfeld's theoretical analysis [37] and Keulegan's theoretical and experimental research [22, 24]. The fundamental difference between these two approaches lies in the introduction of bed shear stresses. Schijf and Schönfeld [37] defined the bed shear stresses as a function of the mean velocity of the lower layer. This velocity goes to zero in each cross section of the wedge; therefore, the bed shear stresses by definition are zero. Keulegan [22, 24], on the other hand, through an integration of the equations of motion in each layer and using the actual velocity profiles, derived expressions for the bed and interfacial shear stresses τ_0 and τ_i, respectively, and the associated friction coefficients f_0 and f_i. His experiments showed that the bed shear stresses are substantial. The bed shear stresses distribution is important since these stresses control the overall flow dynamics and specifically the sediment erosion and deposition [28, 29]. Therefore,

a reliable estimate of this distribution would contribute to an improved design of navigation canals and to a better environmental control.

In the analysis of any problem which is associated with mass, energy, and momentum transport, a knowledge of the vertical velocity distribution is of primary importance. From the analysis of the first experimental results, it became obvious that the nondimensional velocity distribution in the vicinity of the interface follows a logarithmic law as in the case of fixed boundaries. These first results were reinforced by Csanady's [9] and Powell's [34] data. In general, there are limited studies on the laws which govern the nondimensional velocity distribution in strongly stratified flows. Among the most interesting of them are the studies by Csanady [9], Powell [34], and Hino et al. [17].

Csanady [9] elaborated on Lofquist's experimental results [26] on stratified flows where there was uniform motion of the lower denser layer under a quasi-stagnant upper lighter layer. These experiments took place before 1960 without any use of modern electronic instrumentation. Csanady [9], in his effort to give a universal law for the nondimensional velocity distribution, defined a constant coefficient κ analogous to the von Karman universal constant κ. Powell [34], in his study on fresh water flow over a quasi-stagnant salt water layer, found that the velocity distribution law in the upper layer is logarithmic and claimed that the distribution depends on an equivalent von Karman constant. His data, however, were not sufficient to permit the derivation of the pertinent law. Hino et al. [17] studied the dynamics of arrested saline wedges and they considered a logarthmic-linear velocity

distribution for the upper layer according to Monin-Obukov similarity theory. Keulegan [22, 24] and some other investigators gave a dimensional or nondimensional velocity distribution without making an effort to find the governing law.

The objectives of the present study were (1) the experimental investigation of interfacial and bed shear stresses and especially the derivation of generalized laws linking these stresses to the pertinent gross flow parameters and fluid properties and (2) the study of the flow structure in the vicinity of the interface and in the upper and lower layer, for the purpose of obtaining a velocity distribution law of universal validity.

The experiments were conducted in an open salinity flume constructed in the Coastal and Oceanographic Laboratory of the University of Florida, in Gainesville, Florida, U.S.A. The apparatus consists of a 20.24 m long open channel of a square cross section 45.7 cm x 45.7 cm constructed of transparent plexiglass, and of the accessory tanks for recirculation of fresh water and the supply of salt water. The system was equipped with the necessary electronic instrumentation for the measurements of velocities, salinities, temperatures, and Reynolds stresses.

The investigation herein described led to original correlations for the interfacial and bed shear stress coefficient and to equally original velocity distribution laws in the neighborhood and within the interfacial zone. Useful and interesting results have also been obtained regarding the nature and the validity of the interfacial friction coefficient obtained by Schijf and Schönfeld's simplified model [37].

CHAPTER II
BACKGROUND AND REVIEW OF EARLIER INVESTIGATIONS

2.1 Basic Parameters

The simple stratified flow system of Figure 2.1, where denser liquid flows over a spillway, is first analyzed in order to introduce some basic concepts of stratified flows [15]. The two layers are considered frictionless and nonmixing. Therefore, the velocity and the density distribution are discontinuous at the interface. The upper layer is stagnant and the velocity of the lower layer is considered uniform over any cross section.

Application of the energy equation between points A and B at the interface, first for the stagnant upper layer and second for the moving lower layer, gives

$$\frac{V_B^2 - V_A^2}{2} = \frac{\Delta\rho}{\rho_2} g\Delta h \tag{2.1.1}$$

where g is the gravity acceleration with the other parameters identified in Figure 2.1. If the velocity V_A is very small compared with the velocity V_B, Equation (2.1.1) becomes

$$V_B = \sqrt{2\frac{\Delta\rho}{\rho_2} g\Delta h} \tag{2.1.2}$$

In the case where $\Delta\rho \cong \rho_2$, as in air-water systems, Equation (2.1.2) becomes identical with the free surface flow equation over a spillway.

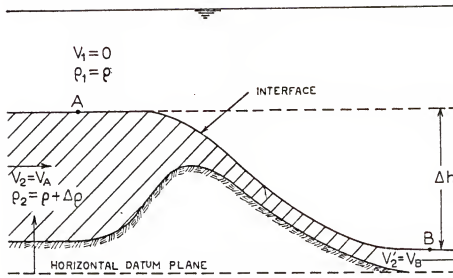

Figure 2.1 Gravity flow in a two-layered system

Source: [15, Figure 26.1]

In the case where $\Delta\rho \cong 0.0$, as in homogeneous fluids, the velocity is zero (no motion). Therefore, the driving force is the submerged weight of the denser fluid, which corresponds to a reduced gravitational acceleration denoted by

$$g' = \frac{\Delta\rho}{\rho_2} g = \frac{\Delta\rho}{\rho + \Delta\rho} g \tag{2.1.3}$$

and defined as "densimetric gravitational acceleration." For small values of $\Delta\rho$ compared with ρ, Equation (2.1.3) takes the form

$$g' = \frac{\Delta\rho}{\rho} g \tag{2.1.4}$$

Substituting g by g' in the definition of Froude number, a new nondimensional number is introduced as

$$Fr' = \frac{V}{\sqrt{g'h}} \tag{2.1.5}$$

where V and h represent characteristic velocity and length scales of the flow system, respectively. This number is called "densimetric Froude number" and it is a basic parameter in stratified flows for dynamic similarity.

In 1949, Keulegan [21], in order to study the interfacial stability of viscous fluids, introduced a nondimensional parameter Θ defined by the equation

$$\Theta = \frac{1}{V} \left[\nu g \frac{\Delta\rho}{\rho}\right]^{1/3} \tag{2.1.6}$$

where V is the local average velocity of the moving layer and ν is the kinematic viscosity of the heavier fluid. This equation comes from Jeffrey's criterion [20] for the generation of wind waves. Equation (2.1.6) can also be written in the form

$$K^3 = \frac{\nu g'}{V^3} = \frac{1}{Re(Fr')^2} \tag{2.1.7}$$

where Re is the Reynolds number. K is known as "Keulegan's number."

In the system of Figure 2.1, the velocity and density distributions are discontinuous at the interface. Viscosity and mixing, however, lead to a continuous distribution of both variables around the interface, albeit at sharp rates. The Richardson number, Ri, defined by the relation

$$Ri = - \frac{g}{\rho} \frac{(d\rho/dy)}{(du/dy)^2} \tag{2.1.8}$$

is introduced as a stability parameter of flow where $d\rho/dy$ and du/dy are the density and velocity gradients, respectively. When the flow is considered as one-dimensional, the Richardson number becomes identical with the densimetric Froude number [Equation (2.1.5)].

2.2 Mixing Mechanisms and Density Interface

The main mixing mechanisms are (a) the entrainment and (b) the turbulent diffusion. Entrainment is the vertical one-way volume flux through the interface from the lower to the upper layer. Turbulent diffusion is the mass transport of the dissolved or suspended matter by the turbulent velocity fluctuations. As a result of the mixing, a thin

layer, called the interfacial layer or interfacial zone, is formed with high gradients of continuously varying density. In the present study the term "interface" indicates the surface at which the density is the average of the two fluid densities.

2.3 Velocity Interface

Experimental observations suggest that in the vicinity of the interface there is a zone where the velocity gradients are large. Linden [25] calls this zone "velocity interface zone." Lofquist [26] observed that the point of inflection of the velocity distribution curve is about 1 mm to 3 mm over the interface. In Powell's experiments [34], the above point of inflection was found to be at a position where the velocity was the average of the velocities $U_{1\infty}$ and $U_{2\infty}$ of the two layers very far from the velocity interfacial zone. In this study the term "velocity interface" designates a theoretical surface, where the velocity has the mean value of $U_{1\infty}$ and $U_{2\infty}$. A characteristic of the velocity interface is that the viscous stresses in its vicinity are maximized.

From Figure 2.2 we can see the influence of interfacial zone and velocity interfacial zone widths on Richardson number, Ri. The two interfaces usually do not coincide. The stratified flow, which is studied herein, belongs to the second case of Figure 2.2.

2.4 Review and Discussion of Earlier Investigations

2.4.1 The Interfacial Friction Coefficient

The scientific interest and practical significance of the interfacial friction coefficient, f_i, motivated extensive laboratory

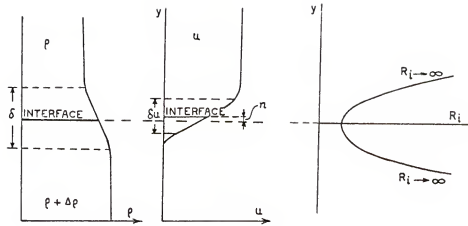

(a) Thick density interface

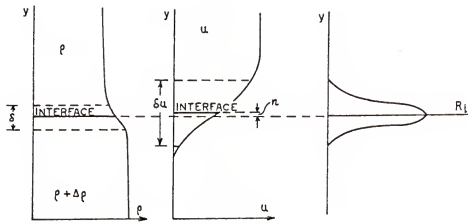

(b) Thin density interface

Figure 2.2 The effect of width of interfacial zone on the Richardson number

Source: [34]

research and field investigations in the last thirty years in order to obtain a reliable correlation of f_i to the gross flow parameters and fluid properties, which define the flow.

An extensive review and discussion of the best known investigations was presented in Chapter II of the author's previous dissertation [11]. For this reason only a short review of earlier investigations will be given in this section with some more details on Keulegan's experiments [20, 24] and on the author's previous research [11].

For the arrested saline wedge, only Keulegan's experimental studies [22, 24] give essentially bottom shear stresses. His mathematical model, modified and refined, is used in this study for the formulation of bottom shear stresses. The Schijf and Schönfeld mathematical model [37] is widely known for the evaluation of the interfacial friction coefficient f_i. Finally, in the author's earlier work [11] a satisfactory correlation of f_i to the mean flow parameters and the fluid properties has been obtained. This correlation can be used as a first approximation of f_i in practical applications. Moreover, in the present study, f_i is also correlated with the same parameters as in [11, 30], with satisfactory results.

Keulegan [22] applied the equations of motion in each layer to compute the interfacial and bed shear stresses of arrested saline wedges. His basic assumptions were (a) negligible vertical accelerations, (b) hydrostatic pressure distribution, and (c) small density difference between the two layers as compared to the average density.

Keulegan's analysis [22, 24] led to the following equations for the mean interfacial and bed shear stresses T_i and T_0, respectively:

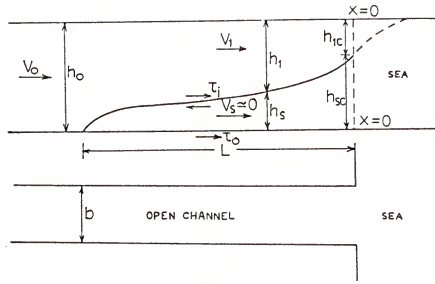

Figure 2.3 Arrested saline wedge

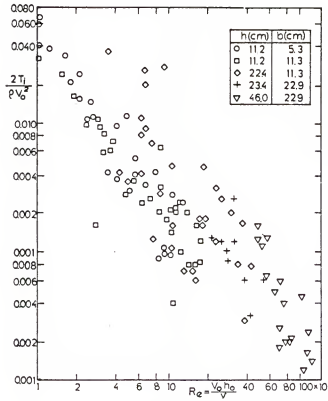

Figure 2.4 Mean interfacial shear stresses

Source: [22]

$$\frac{T_i}{\rho V_0^2} = -\frac{gh_0}{V_0^2} \cdot \overline{\frac{dH}{dx}}\, I_a - \alpha \cdot \frac{h_0}{L} I_b - \frac{f_{w0}}{4} \cdot \frac{h_0}{b} I_c \qquad (2.4.1.1)$$

and

$$\frac{T_i}{\rho V_0^2} + \frac{T_0}{\rho V_0^2} = \left[1 - (Fr_0')^{2/3}\right] \frac{gh_0}{V_0^2} \left[\overline{\frac{dH}{dx}}\, I_d + \frac{\Delta\rho}{\rho} \frac{h_{sc}}{2L}\right]$$

$$+ \frac{0.058\left[1 - (Fr_0')^{2/3}\right]}{(Fr_0')^{4/3}} \cdot \frac{h_0}{L} \qquad (2.4.1.2)$$

Here $\overline{\frac{dH}{dx}}$ is the mean slope of the piezometric line,

$$\alpha = (1/A_1)\int_{A_1} (u/V_i)^2 dA,$$

A_1 is the cross sectional area of the upper layer, u is the local time-averaged velocity, V_1 is the mean velocity of the upper layer, f_{w0} is the wall friction coefficient upstream of the wedge,

$$Fr_0' = V_0 \Big/ \sqrt{\frac{\Delta\rho}{\rho} gh_0}$$

is the densimetric Froude number upstream of the wedge, V_0, h_0 are the velocity and the depth upstream of the wedge, respectively, $\Delta\rho$ is the density difference between the two layers, ρ is the fresh water density, g is the gravitational acceleration, h_{1c} is the depth of the upper layer at the ocean end of the channel, $h_{sc} = h_0 - h_{1c}$, L is the length of the arrested saline wedge, b is the width of the channel. Now, introducing n as

$$n = h_{sc}/h_0 \tag{2.4.1.3}$$

I_a, I_b, I_c, and I_d are given by the following formulas:

$$I_a = 1 - 0.485n \tag{2.4.1.4}$$

$$I_b = 2 \cdot \frac{1.028n}{1 - n} \tag{2.4.1.5}$$

$$I_c = 1 + 0.369n + 0.195n^2 \tag{2.4.1.6}$$

$$I_d = 0.496 \tag{2.4.1.7}$$

Keulegan [22, 24] computed the stresses T_i and T_0 using Equations (2.4.1.1) and (2.4.1.2) and data from his experimental results. Figures 2.4 and 2.5 give the values of $T_i/\rho V_0^2$ in terms of the Reynolds number upstream of the wedge. The scattering of the points in Figures 2.4 and 2.5 is significant. This means that there are some other parameters besides the Reynolds number, Re, which influence the stresses. In particular, the extreme values of $T_i/\rho V_0^2$ or $T_0/\rho V_0^2$ differ by more than one order of magnitude for the same value of Re. Keulegan, on the basis of the mean values of the experimental points of Figures 2.4 and 2.5 suggested the graphical relationships of Figure 2.6. This figure indicates that the stresses T_i are inversely proportional to the Reynolds number, Re. This observation led him to consider the interfacial stresses as laminar. This is contrary to the experimental results of several investigators, where significant Reynolds stresses were detected [3, 4, 12, 13, 19, 26, 35, 39].

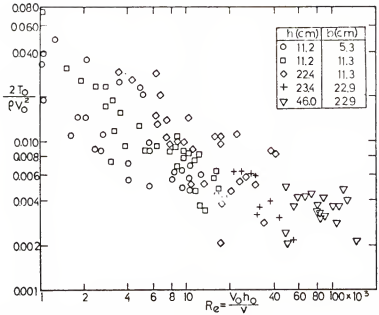

Figure 2.5 Mean shear stresses at the bottom

Source: [22]

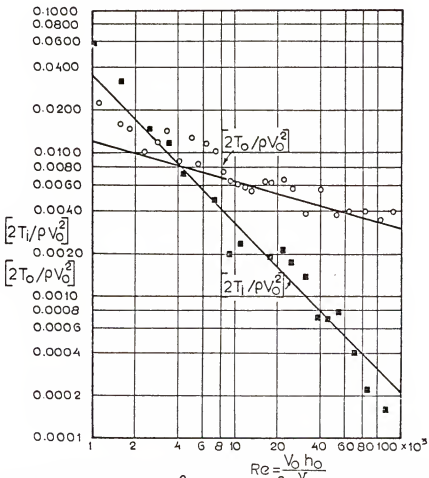

Figure 2.6 Variation of $2T_i/\rho V_0^2$ and $2T_0/\rho V_0^2$ with Reynolds number

Source: [22, 24]

It is, moreover, observed that for large Reynolds numbers, the shear stresses at the bottom are larger than the corresponding interfacial shear stresses.

In 1977, the author completed a study on the dynamics of a two-layered system which consisted of a fresh water layer flowing over a quasi-stagnant salt water layer. The analysis of the experimental data was based on a one-dimensional steady uniform flow model, similar to that developed by Schijf and Schönfeld [37] for open channels. Comparison of the data of the latter study with data obtained by other investigators for the same type of stratified flow is given in Figure 2.7 [11, Figure 6.13]. The scattering of the data points does not permit any reliable conclusion on the variation law for f_i. The same scattering appears in other types of stratified flows when f_i is plotted versus the Renyolds number only. Figure 2.8 [11, Figure 6.14] gives an example of such scattering for underflows. From the comparison of Figures 2.4, 2.7, and 2.8, it can be concluded that f_i is not only a function of Re, but it also depends on some other parameters. A satisfactory correlation was obtained when f_i was expressed as a function of $ReFr^2$, where Fr is the nondensimetric Froude number of the flow, with $\Delta\rho/\rho$ as an independent parameter (Figure 2.9). In Figure 2.10 the line of Figure 2.9 for $\Delta\rho/\rho = 0.020$ has been reproduced, while reanalyzed data by Abraham and Eysink [1] for counterflows have been plotted. The latter fall quite closely on the present curve and its extrapolation. Finally, one point corresponding to a single set of data from the South Pass of the Mississippi River has been added. In spite of the wide gap of the parameter $ReFr^2$, that point falls on a smooth extrapolation of

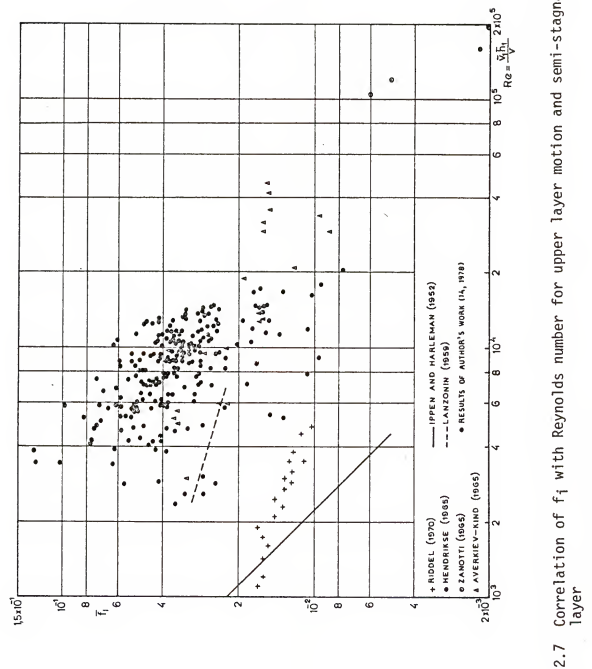

Figure 2.7 Correlation of f_i with Reynolds number for upper layer motion and semi-stagnant lower layer

Source: [11, Figure 2.7]

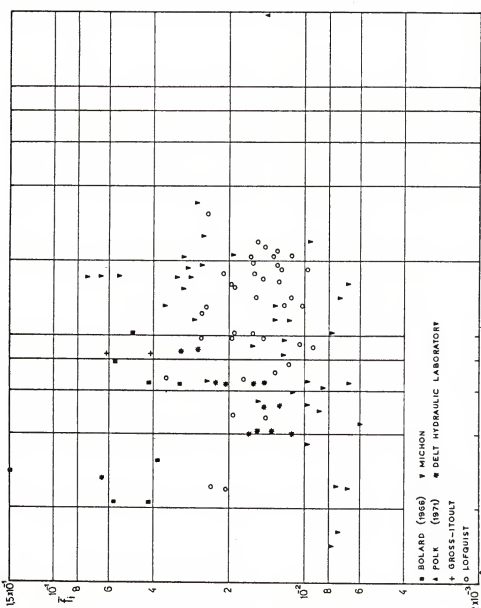

Figure 2.8 Correlation of f_i with Reynolds number for underflows [11, Figure 2.8]

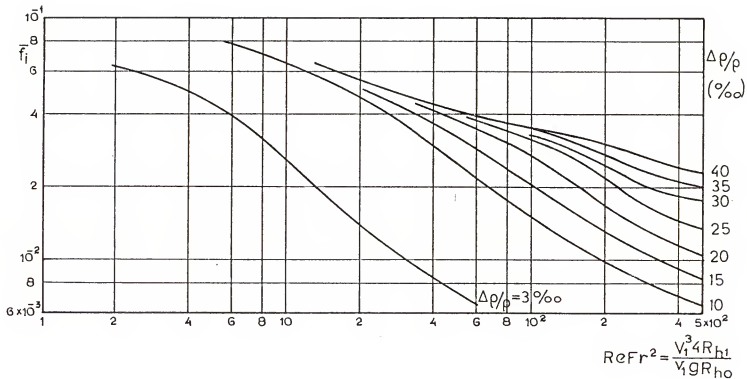

Figure 2.9 Variation of f_i with $ReFr^2$ and $\Delta\rho/\rho$

Source: [11, Figure 6.11.9]

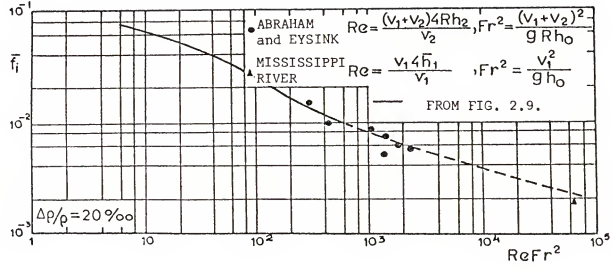

Figure 2.10 Extrapolation of the $\Delta\rho/\rho$ = 0.020 line of Figure 2.9 and comparison with earlier laboratory and field data

Source: [11, Figure 6.12]

the $\Delta\rho/\rho$ = 0.020 line of the author's study [11]. This is indicative that the correlation parameters have been properly selected.

In Figure 2.11, the curves of Figure 2.9 have been extrapolated in a qualitative manner following roughly the extrapolation of the $\Delta\rho/\rho$ = 0.20 curve. This extrapolation should be considered tentative, since only one field point was used. The graphs of Figures 2.9 and 2.11 can be used as a first approximation for the f_i value for any type of stratified flow.

In 1953 Schijf and Schönfeld [37] studied a system of two layers of infinite width and particularly the arrested saline wedge. For the latter they gave the following equation for the mean value of f_i:

$$\overline{f_i} = \frac{2h_0}{L}\left[\frac{1}{5(Fr_0')^2} - 2 + 3(Fr_0')^{2/3} - \frac{6}{5}(Fr_0')^{4/3}\right] \qquad (2.4.1.8)$$

In 1953 Bata and Knezevich [8] studied the turbidity currents in reservoirs as a density stratified underflow. They found $\overline{f}$ = 0.010 for smooth bed and $\overline{f}$ = 0.020 for rough bed, where $\overline{f}$ incorporates the resistance of both the solid boundaries and the interface.

In 1957 Bata [7] studied the warm wedge using Schijf and Schönfeld's [37] equation.

In 1960 Lofquist [26] studied the uniform flow of a heavier salt water under a quasi-stagnant fresh water layer using the equations of motion. Besides the detailed velocity and density profiles at the interfacial zone, he introduced the ratio of the total stresses to the laminar stresses and, neglecting the significant scattering of the data points, he derived the relation

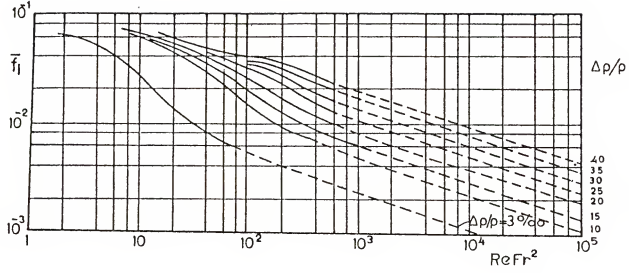

Figure 2.11 Tentative extrapoliation of the curves of Figure 2.9

Source: [11, Figure 6.12a]

$$\frac{u_{max}^2}{\nu\left(\frac{du}{dy}\right)_{max}} = \frac{Re}{4.34} \qquad (2.4.1.9)$$

where u_{max} is the maximum cross sectional velocity in the lower layer, ν is the mean kinematic viscosity of the layers, $(du/dy)_{max}$ is the maximum velocity gradient, and Re is the Reynolds number of the lower layer defined as $Re = (V_2 R_{h2})/(\nu_2)$. Here V_2, ν_2, R_{h2} are the mean velocity, hydraulic radius, and kinematic viscosity of the lower layer, respectively. Lofquist [26] subsequently introduced the ratio β_{max} as

$$\beta_{max} = \frac{Re\lambda_{max}}{4.34} = \left[\frac{u_{max}^2}{\nu\left(\frac{du}{dy}\right)_{max}}\right] \lambda_{max} \qquad (2.4.1.10)$$

where λ_{max} is the interfacial friction coefficient given as $\lambda_{max} = \tau_{max}/\overline{\rho u}_{max}^2$, τ_{max} is the maximum shear stress, and $\overline{\rho}$ is the mean density of the fluids. Finally, he found that β_{max} is a function of the Reynolds number, Re, and of the densimetric Froude number, Fr'. The scattering of the data points, however, was substantial. In the case of laminar flow at the interface β becomes equal to unity.

In 1962 Macagno and Rouse [27] studied the case of counterflow in a closed rectangular duct. They found that the ratio of the total stress to the viscous stress at the interface is a function of the Reynolds number and of the densimetric Froude number. These numbers were based on the maximum algebraic velocity difference and on the distance between the points of maximum velocities in the moving layers.

Their analysis was based on the assumption of laminar flow at the fixed boundaries.

In 1964 Iwasaki [18] studied stratified flows with a fresh water upper layer moving over a quasi-stagnant salt water lower layer. He suggested a close dependence of f_i on Keulegan's number $K = Re(Fr')^2$. A summary of data from several sources, including Iwasaki's results, is given by Sherenkov et al. [39, Figure 6] and by Plate and Friedrich [32, Figure 4]. It is observed that Iwasaki's data points [18] fall on a straight line with little scattering; however, all other points fall on a distinctly different line whose mean slope is considerably smaller than that given by Plate and Friedrich [32].

Averkiev and Kind [4] investigated the dynamics of stratified flows in cooling ponds. They defined f_i as a function of the Reynolds stresses only by the relation $f_i = -8\overline{u'v'}/V^2$, where V is the mean cross sectional velocity and where $\overline{u'v'}$ was measured directly. They found that f_i is a function of Re for small values of the Re while for large $Re(Re = Vh/\nu > 10{,}000)$ f_i was found to be constant and equal to about 0.016.

Shi-Igai [40] analyzed the flow of an upper fresh water layer over a quasi-stagnant salt water layer. He defined the interfacial shear stresses by the relation $\tau_i = \varepsilon/V_1$, where ε is the viscous energy dissipation per unit surface of fluid caused by interfacial harmonic waves and V_1 is the uniform velocity of the moving layer. He derived the following equation:

$$f_i = \frac{8\tau_i}{\rho V_1^2} = 32\pi^2 \left(\frac{\alpha}{\lambda}\right)^2 \frac{1}{Re(Fr')^2} \qquad (2.4.1.11)$$

where $Re = V_1 h_1/\nu$, $Fr' = V_1/\sqrt{g \frac{\Delta\rho}{\rho} h_1}$, h_1 is the thickness of the upper layer and α and λ are the amplitude and the length of the interfacial waves, respectively. The factor $A_1 = 32\pi^2(\alpha/\lambda)^2$ was found to be about 48. This value was based on his limited experimental data.

In 1966 Shi-Igai and Kono [41] studied the arrested saline wedge and they expressed f_i by the relation

$$f_i = \frac{A}{Re(Fr')^2} \qquad (2.4.1.12)$$

where Re and Fr' are the Reynolds and densimetric Froude number upstream of the wedge, respectively, and A is an experimental constant equal to about 80.

In 1971 Abraham and Eysink [1] investigated the case of exchange flows with constant densimetric Froude number, $Fr' \cong 0.8$, on the basis of Schijf and Schönfeld's equation [37]. Moreover, they reanalyzed Keulegan's [23] and Barr's [5, 6] experimental data. They came to the conclusion that f_i is only a function of Re for small values of Re and that f_i is constant for large values of Re.

In 1971, Polk et al. [33] studied the dynamics of warm wedges in the field and computed f_i by equations similar to those derived by Schijf and Schönfeld [37]. The coefficient f_i ranged from 0.08 to 0.013 for $8\times10^5 \leq Re \leq 2.3\times10^7$ and for various densimetric Froude numbers.

In 1971 Riddell [36] conducted an extensive investigation on the arrested saline wedges. His experimental results were reanalyzed at the Delft Hydraulic Laboratory using Schijf and Schönfeld's mathematical model [37] to obtain values of f_i.

In 1972 Georgiev [13] studied uniform underflows using photo-measurements to determine instantaneous velocities. A number of 70 to 90 instantaneous velocities were used to calculate the time-average velocity and Reynolds stresses in each point of the cross section. The total interfacial shear stress was given by the relation

$$\tau_i = - \overline{\rho}\ \overline{u'w'} + \overline{\mu}\ \frac{du}{dz} \qquad (2.4.1.13)$$

where u' and w' are the turbulent velocity fluctuations in the direction of flow, x, and the direction of gravity, z, respectively, while bars indicate average values. The coefficient f_i was defined as $f_i = 8\tau_i/\overline{\rho}V^2$ where V is the mean velocity of the moving layer. Georgiev's [13] plot of experimental data points, based on the hydraulic radius of the lower layer, indicate that f_i is a function of the Reynolds number, Re, only. However, in his experiments that number ranged from 10^3 to 10^4 only.

In 1972 Harleman and Stolzenbach [16] in their study of the re-circulation in cooling pools, where heated water is discharged from power plants, reviewed data of previous investigators. For the turbulent zone of their graph and with significant scattering of data points they suggested the following functional relation:

$$\frac{1}{\sqrt{f_i}} = 2.0 \log \mathrm{Re}\sqrt{f_i} - 0.8 \qquad (2.4.1.14)$$

In 1974 the Delft Hydraulics Laboratory [10] selected and reanalyzed the best known, at that time, data on stratified flows. This summary was extensively discussed in the author's earlier work [11] and some conclusions are herein presented.

a. There is no indication of any consistent relationship which correlates f_i either to the Reynolds number, Re, or to the densimetric Froude number, Fr'.

b. In turbulent flows, f_i decreases as Re is increased for low values of the latter.

c. For large values of Re, there is no clear relationship between f_i and Re.

Figures 2.12 and 2.13 provide additional bases for the previous conclusions as seen from the scatter of data.

In 1979 Abraham, Karelse, and van Os [2] assumed that the interfacial friction coefficient, f_i, is a function of the Reynolds number, Re, the Richardson number, Ri, and that it depends also on the type of flow. Moreover, they stated that the interfacial shear stresses, τ_i, are affected by turbulence which is generated at the interface and at the bed. Particularly, for arrested saline wedges, they considered that τ_i depends only on the interfacial turbulence. This is not the real case, however, since substantial shear flow takes place near the bed, which affects the velocity profile within the interfacial zone and through it the interfacial shear stresses. They claimed that, for Reynolds number higher than 10^6, f_i is constant and equal to 0.0032.

Among the latest advances in stratified flow is Powell's [34] study of flow of an upper fresh water layer over a quasi-stagnant salt

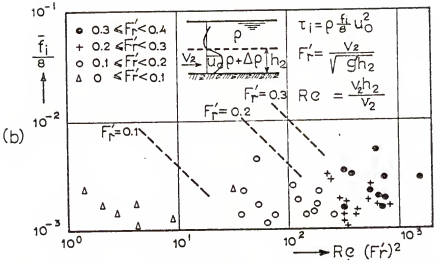

Figure 2.12 Variation of the average f_i for underflows according to Lofquist's experimental data

Source: [10, Figure 2.6]

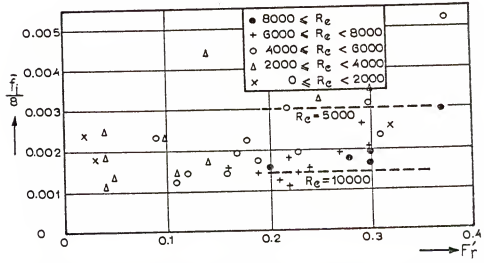

Figure 2.13 Variation of the Average f_i for underflows according to Lofquist's experimental data

Source: [10, Figure 2.7]

water layer of appreciable depth. Powell [34] calculated the interfacial shear stresses, τ_i, by direct measurements of viscous and Reynolds stresses. On the basis of his experimental results the interfacial friction coefficient, f_i, appeared to be a function of the Reynolds number, Re, only. However, his data were based on a limited range of variation of the relative density difference and of some other flow parameters.

In their study of saline wedges in 1980, Hino et al. [17] considered a linear-logarithmic velocity distribution for the upper layer according to Monin-Obukov similarity theory. They defined the interfacial friction coefficient by the equation

$$f_i = 2\left(\frac{u_{*i}}{V_1}\right)^2 = 2\left[\frac{\kappa S_2}{(1+\beta)V_1}\right]^2 \qquad (2.4.1.15)$$

where u_{*i} is the interfacial friction velocity, κ is the von Karman constant, β is the Monin-Obukov constant, V_1 is the average velocity of the upper layer, and S_2 is the slope of the logarithmic plot, i.e.,

$$S_2 = \frac{u_{*i}}{\kappa}(1+\beta)$$

They also gave f_i as a function of $Re(Fr')^2$ with Fr' as an independent parameter.

The discrepancy among various formulas and methods in estimating values of f_i can be demonstrated with an application to the South Pass of the Mississippi River for the following data [31]: discharge,

Q = 2,837 m^3/sec.; width, b = 500 m; depth, h = 15 m; fresh water velocity, V_0 = 0.38 m/sec.; relative density difference, $\Delta\rho/\rho$ = 0.02; kinematic viscosity, $\nu = 10^{-6}$ m^2/sec.; densimetric Froude number upstream of the wedge, Fr_0' = 0.22; and measured salinity intrusion, L = 22.5 km. It is noted that the critical velocity for initiation of entrainment is of the order of 10 percent of the actual velocity; therefore, entrainment does take place through the theoretical interface and the flow within the interfacial zone is expected to be turbulent. The following results are obtained:

a. From Schijf and Schönfeld's [37] model, f_i = 0.00185
b. From Keulegan's [22, 24] equation for laminar flow around the interface, $f_i = 2.5 \times 10^{-5}$
c. From Bata and Knezevich's [8] equation for Re = 244.4×10^5, $f_i = 0.74 \times 10^{-5}$
d. From Shi-Igai's [40, 41] equation, after properly converting Re and Fr' to mean flow conditions over the wedge, $f_i = 0.96 \times 10^{-5}$, and
e. From Harleman and Stolzenbach's [16] equation, f_i = 0.0071

This limited review led to the following conclusions: (1) The actual value of f_i, based on field measurements, may exceed the values given by equations based on laminar flow conditions around the interface by two to three orders of magnitude, (2) f_i cannot be expressed as a function of the Reynolds number, Re, only, and (3) the functional dependence of f_i on the Keulegan number seems to be rather weak.

These conclusions motivated the author to investigate the interfacial friction coefficient, for the first time, in his earlier work [11]. His analysis was based on a one-dimensional model similar to that by Schijf and Schönfeld [37] for open channels. The main results are given in Figures 2.9, 2.10, and 2.11. The graphs in the figures are the result of many trials for the correlation of f_i to the gross flow parameters and fluid properties and can be used as a first estimate of f_i.

2.4.2 Bed Shear Stresses in Arrested Saline Wedges

The only experimental work on the bed shear stresses, T_0, was conducted by Keulegan [22, 24] (Figures 2.5, 2.6). In Figure 2.6, the bed shear stresses, T_0, are larger than the interfacial shear stresses, T_i, at least by one order of magnitude for large Reynolds numbers.

2.4.3 Velocity Profiles at the Interfacial Zone

Lofquist [26] was one of the first investigators who studied systematically the interfacial velocity distribution. He gave the non-dimensional velocity distribution by the functional relationship

$$\frac{u - V_i}{u_*} = F\left[\frac{(y - y_i)(\partial u/\partial y)_{max}}{u_*}, \beta_{max}\right] \qquad (2.4.3.1)$$

where V_i, y_i are the velocity and the depth, respectively, at the interface, u_* is the friction velocity at the interface, given by the equation $u_* = \sqrt{\tau_{imax}/\rho}$, τ_{imax} is the maximum interfacial shear stress. Equation (2.4.3.1) is given graphically by Lofquist [26] in Figure 2.14.

In 1978 Csanady [9] reanalyzed Lofquist's experimental data [26] to study the turbulence structure around the interface. His nondimensional

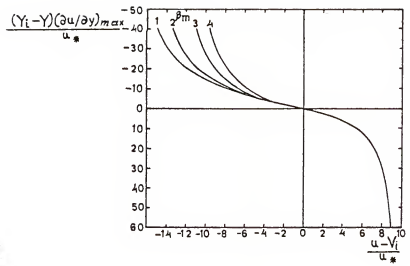

Figure 2.14 Velocity profile

Source: [26, Figure 14]

velocity distribution law, defined as "law of the interface," corresponds to the "wall law" for fixed boundaries and is given by the equation

$$\frac{u}{u_*} = \frac{1}{\kappa} \ln \left[\frac{u_*(y - y_i)}{\nu_e} \right] + F(K_i) \qquad (2.4.3.2)$$

where κ is the von Karman constant, ν_e is the effective viscosity, defined as

$$\nu_e = \frac{u_*^2}{(du/dy)_i} \qquad (2.4.3.3)$$

$(du/dy)_i$ is the velocity gradient at the interface and K_i is the Keulegan number at the interface defined as

$$K_i = \frac{(\Delta\rho/\rho)g\nu}{u_*^3} \qquad (2.4.3.4)$$

The law of the interface raises some questions. Specifically, the inverse of the coefficient of the logarithmic law is equal to von Karman's constant for fixed boundaries, where no transport of mass and momentum takes place through the boundary. However, such transport does take place through the interface of the two-layered stratified system.

Powel [34], in his recent and aforementioned doctoral dissertation, studied the velocity and density distribution near the interface. The nondimensional velocity distribution is given in Figure 2.15 [34, Figure 27]. For a region over the interface the graph has a logarithmic

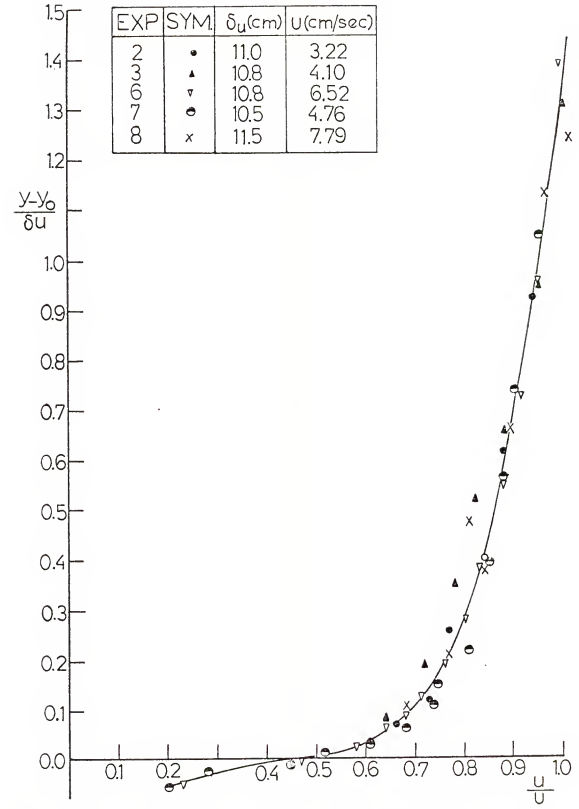

Figure 2.15 Normalized mean velocity profile from Powell's data

Source: [34, Figure 27]

form. Powell [34] postulated that the transport of mass and momentum through the interface may modify the turbulence structure in the vicinity of the latter and he gave the following general form of the velocity distribution law:

$$\frac{u}{u_*} = F_1(K_i)\ \ell n \left[\frac{u_*(y - y_i)}{\nu}\right] + F_2(K_i) \qquad (2.4.3.5)$$

where $F_1(K_i)$ and $F_2(K_i)$ are functions of the Keulegan number defined at the interface. Powell's data [34] were not sufficient to permit the derivation of a law for either $F_1(K_i)$ or $F_2(K_i)$.

Hino et al. [17] also made use in their aforementioned recent work of the Monin-Obukov similarity theory and claimed that velocity profiles obey the "log-linear" law or the "bi-log" law.

In the case of arrested saline wedges Keulegan [22, 24] gave a nondimensional velocity distribution, shown in Figure 2.16, without any information on the flow parameters and salinity.

The dimensional or non-dimensional velocity distribution laws given by various investigators differ not only for different types of stratified flows, but also for the same type of flow. The graphs given by Georgiev [13], Polk et al. [33], and Sherenkov et al. [39] have a logarithmic form at the interfacial region. The graphs presented by Averkiev and Kind [4] appear to be parabolic while those by Bata and Knezevich [8] have a distribution ranging from parabolic to logarithmic.

This limited review leads to the following conclusions:

(1) The shape of the profile varies from parabolic to logarithmic.

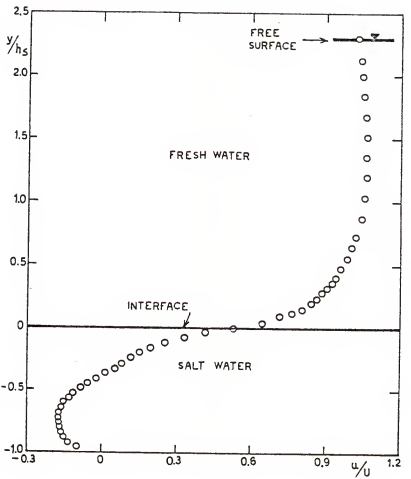

Figure 2.16 Velocity distribution in a cross section of arrested saline wedge, after Keulegan

Source: [24, Figure 11.7]

(2) Csanady's law [9] gives the inverse of the coefficient of the logarithmic term equal to von Karman's constant, although Powell's [34] recent research seems to suggest that this coefficient must be a function of the Keulegan number. (3) There is no law of variation for the equivalent von Karman coefficient nor for the constant factor in the logarithmic law. The objective of the work herein presented has been to provide some answers to the specific problems and questions isolated in this review and to fill a number of gaps in our knowledge on stratified flows.

CHAPTER III
THEORETICAL BACKGROUND

3.1 Fundamental Equations

For Newtonian and incompressible fluids with constant viscosity the equations of conservation of momentum, known as Navier-Stokes equations, are

$$\tilde{\rho} \frac{d\vec{V}}{dt} = - \vec{\nabla} P + \tilde{\rho} \vec{b} + \mu \vec{\nabla}^2 \vec{V} \tag{3.1.1}$$

where $\vec{V} = u_1 \vec{i} + u_2 \vec{j} + u_3 \vec{k}$ is the velocity vector with $\vec{i}$, $\vec{j}$, and $\vec{k}$ the unit vectors in the directions of the positive Cartesian coordinate axes x_1, x_2, x_3, respectively,

$$\vec{\nabla} = \frac{\partial}{\partial x_1} \vec{i} + \frac{\partial}{\partial x_2} \vec{j} + \frac{\partial}{\partial x_3} \vec{k}$$

is the vector operator del, $\vec{b} = b_1 \vec{i} + b_2 \vec{j} + b_3 \vec{k}$ is the body force per unit volume, $\tilde{\rho}$ is the local fluid density, P is the pressure, and μ is the molecular viscosity. Moreover, if the fluid is nondiffusive and nonconductive, the equations of incompressibility and continuity have the forms

$$\frac{D\rho}{Dt} = \frac{\partial \rho}{\partial t} + u_j \frac{\partial \rho}{\partial x_j} = 0 \tag{3.1.2}$$

$$\vec{\nabla} \cdot \vec{V} = 0 \tag{3.1.3}$$

In a gravitational field Equations (3.1.1) and (3.1.3) can be written in the form

$$\tilde{\rho} \frac{\partial U_i}{\partial t} + \tilde{\rho} U_j \frac{\partial U_i}{\partial x_j} = - \frac{\partial P}{\partial x_i} - \tilde{\rho} g_i + \mu \frac{\partial^2 U_i}{\partial x_j \partial x_j} \tag{3.1.4}$$

and

$$\frac{\partial U_j}{\partial x_j} = 0 \tag{3.1.5}$$

where i, j = 1,2,3, U_i and g_i are the instantaneous velocity and gravitational component in the x_i direction.

Introducing next for turbulent flows in Equations (3.1.4) and (3.1.5) the notations

$$U_i = u_i + u_i'$$

$$P = p + p'$$

$$\tilde{\rho} = \rho_\ell + \rho'$$

where u_i, p, ρ_ℓ are the local time-averaged values and u_i', p', and ρ' are the fluctuating components of U_i, P, and $\tilde{\rho}$, respectively, and taking into consideration that

$$\overline{u_i'} = \overline{p'} = \overline{\rho'} = 0 \tag{3.1.6}$$

the following equations, for steady state conditions, are obtained:

$$\rho_\ell u_j \frac{\partial u_i}{\partial x_j} + \rho_\ell \overline{u_j' \frac{\partial u_i'}{\partial x_j}} + u_j \overline{\rho' \frac{\partial u_i'}{\partial x_j}} + \overline{\rho' u_j' \frac{\partial u_i}{\partial x_j}}$$

$$+ \overline{\rho' u_j' \frac{\partial u_i}{\partial x_j}} = - \frac{\partial p}{\partial x_i} - \rho_\ell g_i + \frac{\mu \partial^2 u_i}{\partial x_j \partial x_j} \qquad (3.1.7)$$

$$\frac{\partial u_j}{\partial x_j} = 0 \qquad (3.1.8)$$

$$\frac{\partial u_j'}{\partial x_j} = 0 \qquad (3.1.9)$$

Equation (3.1.7) combined with Equations (3.1.8) and (3.1.9) after simplification takes the form

$$\left(u_j + \frac{\overline{\rho' u_j'}}{\rho_\ell} \right) \frac{\partial u_i}{\partial x_j} + \frac{1}{\rho_\ell} \frac{\partial}{\partial x_j} \left[u_j \left(\overline{\rho' u_i'} \right) + \overline{\rho' u_i' u_j'} \right] = - g_i$$

$$+ \frac{1}{\rho_\ell} \frac{\partial}{\partial x_j} \left[- p \delta_{ij} + 2\mu \frac{1}{2} \left(\frac{\partial u_i}{\partial x_j} + \frac{\partial u_j}{\partial x_i} \right) - \rho_\ell \left(\overline{u_i' u_j'} \right) \right]$$

$$+ \frac{\overline{u_i' u_j'}}{\rho_\ell} \frac{\partial \rho_\ell}{\partial x_j} + \frac{1}{\rho_\ell} \overline{u_i' \frac{\partial (\rho' u_j')}{\partial x_j}} + \frac{1}{\rho_\ell} \overline{\left(u_i' u_j' \right) \frac{\partial \rho'}{\partial x_j}}$$

The sum of the three last terms of the previous equation is zero. This follows from Equations (3.1.2), (3.1.8), and (3.1.9). The final equation then becomes

$$\left(u_j + \frac{\overline{\rho' u_j'}}{\rho_\ell}\right) \frac{\partial u_i}{\partial x_j} + \frac{1}{\rho_\ell} \frac{\partial}{\partial x_j} \left[u_j(\overline{\rho' u_i'}) + \overline{\rho' u_i' u_j'}\right] = - g_i$$

$$+ \frac{1}{\rho_\ell} \frac{\partial \tau_{ij}}{\partial x_j} \qquad (3.1.10)$$

where

$$\tau_{ij} = - p\delta_{ij} + 2\mu \frac{1}{2}\left(\frac{\partial u_i}{\partial x_j} + \frac{\partial u_j}{\partial x_i}\right) - \rho_\ell \overline{u_i' u_j'} \qquad (3.1.11)$$

Here τ_{ij} is the stress tensor. The first term of the right hand member represents normal stresses due to the thermodynamic pressure. The terms in the parentheses represent the viscous stresses, the last term represents the Reynolds stresses and δ_{ij} is the Kronecker delta.

Equations (3.1.8), (3.1.9), and (3.1.10) are the governing equations for flow of any incompressible fluid with variable density. There are, however, more unknowns than equations. For this reason we have to resort to assumptions in order to obtain appropriate mathematical models.

In stratified flows with small rates of entrainment and distinct interface, the two layers are normally considered as homogenous with the exception of a zone of small width around the interface. Moreover, if the measurements take place at the centerline of the channel and if the flow is considered symmetrical without secondary currents, the assumption of two-dimensional flow will not deviate from reality. Therefore, in the outer region of the interfacial zone, the equation of motion (3.1.10) can be written in the form

$$U_j \frac{\partial u_i}{\partial x_j} = g_i + \frac{1}{\rho} \frac{\partial \tau_{ij}}{\partial x_j} \tag{3.1.12}$$

and

$$\tau_{ij} = - p\delta_{ij} + 2\mu \frac{1}{2} \left(\frac{\partial u_i}{\partial x_j} + \frac{\partial u_j}{\partial x_i} \right) - \overline{\rho u_i' u_j'} \tag{3.1.13}$$

In the vertical direction, the equation of motion coincides with the equation of hydrostatic pressure distribution. The equations of motion and continuity in the direction of flow have the form

$$u \frac{\partial u}{\partial x} + v \frac{\partial u}{\partial y} = - g \frac{dz_0}{dx} - \frac{1}{\rho} \frac{\partial p}{\partial x} + \frac{1}{\rho} \frac{\partial \tau_{zx}}{\partial z} + \frac{\partial \tau_{yx}}{\partial y} \tag{3.1.14}$$

$$\frac{\partial u}{\partial x} + \frac{\partial v}{\partial y} = 0 \tag{3.1.15}$$

where u and v are the velocity components in the flow direction x and in the vertical direction y, respectively, z is the elevation of the bottom of the channel, and τ_{zx}, τ_{yx} are the shear stresses in the direction x, acting on planes normal to z and y directions, respectively.

3.2 The One-Dimensional Model

On the basis of the Schijf and Schönfeld's assumption [37] and referring to Figure 3.1, Equations (3.1.14) and (3.1.15) for the one-dimensional flow obtain the forms

$$V \frac{dV}{dx} = - g \frac{dz_0}{dx} - \frac{1}{\rho} \frac{dp}{dx} - \frac{1}{\rho} \frac{\partial \tau}{\partial y} \tag{3.2.1}$$

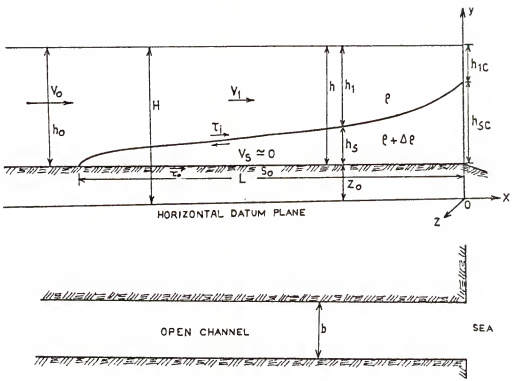

Figure 3.1 Definition sketch of an arrested saline wedge

and

$$V_1 h_1 = \text{const.} \tag{3.2.2}$$

where V is the local mean cross sectional velocity, in general, V_1 is its value in the upper layer and h_1 is the thickness of the upper layer. Equations (3.2.1) and (3.2.2) are next applied to each layer separately (Figure 3.1).

a. Fresh water layer

The integration of Equation (3.2.1) over any cross section of the upper layer gives

$$V_1 \frac{dV_1}{dx} = - g \frac{dz_0}{dx} - \frac{1}{\rho} \frac{dp}{dx} - \frac{\tau_i}{\rho h_1} \tag{3.2.3}$$

where τ_i is the interfacial shear stress. In Equation (3.2.3) the following relations are next introduced together with Equation (3.2.2)

$$\frac{dz_0}{dx} = -S_0 \tag{3.2.4}$$

$$p = p_0 + \rho g(h - y) \tag{3.2.5}$$

$$\tau_i = f_i \frac{\rho V_1^2}{8}$$

where S_0 is the bottom slope of the channel, y is the vertical distance from the bed for $y \geq h_s$, p_0 is a reference pressure, h is the depth of

the system, $h = h_1 + h_s$, h_s is the depth of the lower layer, and ρ is the density of the fresh water layer. After some simplifications, Equation (3.2.3) obtains the form

$$\frac{dh_1}{dx} + \frac{dh_s}{dx} - \frac{V_1^2}{gh_1}\frac{dh_1}{dx} + \frac{f_i V_1^2}{8gh_1} - S_0 = 0 \qquad (3.2.7)$$

b. Salt water layer

Applying the same procedure as in the upper layer and considering that the density difference between the two layers is small, the following equation is obtained

$$\left(1 - \frac{\Delta\rho}{\rho}\right)\frac{dh_1}{dx} + \frac{dh_s}{dx} - \frac{f_i V_1^2}{8gh_s} - S_0 = 0 \qquad (3.2.8)$$

Here the term of the kinetic energy and the term of bottom shear stress were neglected, because, according to the one-dimensional model, V_s—the mean cross section velocity of the lower layer—has to be taken equal to zero. Indeed, the shear stresses at the bottom are defined by the relation

$$\tau_0 = f_0 \frac{\rho V_s^2}{8} \qquad (3.2.9)$$

therefore, if V_s is near zero, then, by definition, τ_0 has to be taken as zero. Assuming next constant total depth, i.e.,

$$h_0 = h = h_1 + h_s = \text{const.} \qquad (3.2.10)$$

Equations (3.2.7) and (3.2.8) can be combined in the form

$$\left[-1 + \frac{V_1^2}{\frac{\Delta\rho}{\rho} g h_1}\right] \frac{dh_1}{dx} = \frac{f_i V_1^2}{8 \frac{\Delta\rho}{\rho} g} \left[\frac{1}{h_1} + \frac{1}{h_s}\right] \tag{3.2.11}$$

The second term in the parentheses of the left hand member is the square of the densimetric Froude number for the upper layer. That is,

$$(Fr_1')^2 = \frac{V_1^2}{(\Delta\rho/\rho) g h_1} \tag{3.2.12}$$

Fr_1' can be written in the form

$$(Fr_1')^2 = (Fr_0')^2 \left[\frac{h_0}{h_1}\right]^3 \tag{3.2.13}$$

Equation (3.2.11), after introducing Equations (3.2.10), (3.2.12), and (3.2.13), takes the form

$$\frac{f_i}{8h_0} dx = \left[1 - \frac{1}{(Fr_0')^2} \left[\frac{h_1}{h_0}\right]^3\right] \left[1 - \frac{h_1}{h_0}\right] \cdot d\left[\frac{h_1}{h_0}\right] \tag{3.2.14}$$

Schijf and Schönfeld [37] considered the saline wedge as a long internal wave. Therefore, its length depends on the condition at the ocean end, that is at $x = 0$. The wedge becomes stationary when the conditions there become critical. The critical depth, $h_1 = h_{1c}$ is given by Equation (3.2.13) for $Fr_1' = 1$, that is

$$\frac{h_{1c}}{h_0} = (Fr_0')^{2/3} \tag{3.2.15}$$

Integration of Equation (3.2.14) from -x to 0 with the introduction of Equation (3.2.15) at x = gives

$$\frac{\bar{f}_i}{8}\frac{x}{h_0} = 3(Fr_0')^{2/3}\left[\frac{1}{4} - \frac{1}{10}(Fr_0')^{2/3}\right] - \frac{h_1}{h_0}\left[\frac{1}{5(Fr_0')^2}\left(\frac{h_1}{h_0}\right)^5 - \frac{1}{4(Fr_0')^2}\left(\frac{h_1}{h_0}\right)^4 - \frac{1}{2}\left(\frac{h_1}{h_0}\right)^2 + \frac{h_1}{h_0}\right] \tag{3.2.16}$$

where $\bar{f}_i$ is the average value of f_i over the length of the wedge, L. That length is the value of x in Equation (3.2.16) for $h_1/h_0 = L$. That is

$$\bar{f}_i L = 2h_0\left[\frac{1}{5(Fr_0')^2} - 2 + 3(Fr_0')^{2/3} - \frac{6}{5}(Fr_0')^{4/3}\right] \tag{3.2.17}$$

The same model and methodology applies to warm wedges [3, 7, 16, 33].

It should be noted that, although the described analysis leads to a handy practical model for the intrusion length and the wedge shape, it does not give the detailed velocity distribution nor the actual significant shear stresses. Moreover, there is no way of estimating analytically f_i. Use, therefore, of Equations (3.2.16) and (3.2.17)

would require previous calibration of f_i on the basis of field and/or laboratory measurements. Even so, it can readily be shown that f_i is very sensitive to changes of the flow parameters. As a result, the use of these equations for cases beyond the calibration conditions becomes unreliable.

3.3 Integration of the Equations of Motion: Complete Intrusion

Equation (3.1.15) is first multiplied by u and then added to Equation (3.1.14) to yield

$$\frac{\partial u^2}{\partial x} + \frac{\partial (uv)}{\partial y} = - g \frac{dz_0}{dx} - \frac{1}{\rho} \frac{\partial p}{\partial x} + \frac{1}{\rho} \left(\frac{\partial \tau_{zx}}{\partial z} + \frac{\partial \tau_{yx}}{\partial y} \right) \qquad (3.3.1)$$

a. Fresh water layer

Equation (3.3.1) integrated over the cross-section $A_1 = bh_1$ gives

$$\int_{A_1} \frac{du^2}{dx} dA + \int_{A_1} \frac{\partial (uv)}{\partial y} dA = - g \frac{dz_0}{dx} \int_{A_1} dA$$

$$- \frac{1}{\rho} \int_{A_1} \frac{\partial p}{\partial x} dA + \frac{1}{\rho} \int_{A_1} \frac{\partial \tau_{zx}}{\partial z} dA$$

$$+ \frac{1}{\rho} \int_{A_1} \frac{\partial \tau_{yx}}{\partial y} dA \qquad (3.3.2)$$

The integrals are given by the following relations:

$$\int_{A_1} \frac{\partial u^2}{\partial x}\, dA = \frac{\alpha}{2}\, bh_1 \frac{dV_1^2}{dx} - bU^2 \frac{dh}{dx} + bV_i^2 \frac{dh_s}{dx} \tag{3.3.3}$$

where

$$\alpha V_1^2 A_1 = \int_{A_1} u^2 dA \tag{3.3.4}$$

and α is the momentum correction coefficient.

$$\int_{A_1} \frac{\partial (uv)}{\partial y}\, dA = bU^2 \frac{dh}{dx} - bV_i^2 \frac{dh_s}{dx} - bV_i v_s \tag{3.3.5}$$

For a pressure given by

$$p = p_0 + \rho g(h - y) \text{ for } y \geq h_s \tag{3.3.6}$$

the pressure integral becomes

$$\frac{1}{\rho} \int_{A_1} \frac{\partial p}{\partial x}\, dA = gbh_1 \frac{dh}{dx} \tag{3.3.7}$$

The shear stress terms finally take the forms

$$\frac{1}{\rho} \int_{A_1} \frac{\partial \tau_{zx}}{\partial z}\, dA = - \frac{2h_1 \tau_w}{\rho} \tag{3.3.8}$$

$$\frac{1}{\rho} \int_{A_1} \frac{\partial \tau_{yx}}{\partial y}\, dA = - \frac{1}{\rho}\, b\tau_i \tag{3.3.9}$$

Here b is the width of the channel, U is the velocity at the free surface, V_i is the velocity at the interface, v_s is the net rate of salt water entrainment per unit area, and τ_w is the sidewall shear stress.

Replacing the integrals by the given functions in Equation (3.3.2), the following equation is obtained:

$$\frac{dH}{dx} + \frac{\alpha}{2g}\frac{dV_1^2}{dx} + \frac{1}{\rho g h_1}\left(\tau_i + \frac{2\tau_w h_1}{b}\right) + \frac{V_i v_s}{g h_1} = 0 \qquad (3.3.10)$$

where dH/dx is the slope of the piezometric line.

The entrainment velocity v_s is equal to q_s/bL_0, where q_s is the rate of salt water entrainment over the saline wedge. The latter has been given by Keulegan [22, 24]. In the analysis of data, the term $V_i v_s/gh_1$ was found to be of minor importance with a maximum effect of 5 percent. Because of this and because entrainment does not take place continuously over the interface, but at isolated spots in the form of breaking of interfacial waves, it was neglected in the subsequent analysis.

Next, expressing τ_w by

$$\tau_w = f_w \frac{\rho V_1^2}{8} \qquad (3.3.11)$$

and solving Equation (3.3.10) with respect to τ_i/ρ the following equation is obtained:

$$\frac{\tau_i}{\rho} = - g(h - h_s) \frac{dH}{dx} - \frac{\alpha}{2} (h - h_s) \frac{dV_1^2}{dx} - \frac{f_w(h - h_s)V_1^2}{4b} \quad (3.3.12)$$

which integrated from -L to 0, gives

$$\frac{T_i}{\rho V_0^2} = - g \frac{h_0}{V_0^2} \overline{\frac{dH}{dx}} I_1 - \frac{\alpha h_0}{2L} I_2 - \frac{f_{w0} h_0}{4b} I_3 \quad (3.3.13)$$

Here T_i and $\overline{dH/dx}$ are the average values of τ_i and dH/dx, respectively, over the wedge, f_{w0} is the wall friction coefficient upstream of the wedge and I_1, I_2, I_3 are dimensionless functions given by Keulegan [24], after a numerical integration of his experimental data [Equations (2.4.1.4), (2.4.1.5), and (2.4.1.6) for I_a, I_b, I_c].

Partheniades et al. [31] developed the following equation for the interface:

$$\frac{x}{L} = \frac{\left[\left(\frac{h_s}{h_{sc}}\right)^3 \left\{\left[4 - 2\left(\frac{h_s}{h_{sc}}\right)\left[(1 - Fr_0')^{2/3}\right]\right]^2 + \left[4 + \left(\frac{h_s}{h_{sc}}\right)\left[1 - (Fr_0')^{2/3}\right]\right]\right\}\right]}{6(Fr_0')^{4/3} + 3(Fr_0')^{2/3} + 1}$$

$$+ \frac{-10\left(\frac{h_s}{h_{sc}}\right)^2 \left[(Fr_0')^{4/3} + (Fr_0')^{2/3} + 1\right]}{6(Fr_0')^{4/3} + 3(Fr_0')^{2/3} + 1} + 1 \quad (3.3.14)$$

where h_{sc} is the critical depth of the lower layer at the ocean end of the channel, that is at x = 0.

Using the last equation, the same investigators derived the following functional relationships for the integrals I_1, I_2, I_3.

$$I_1 = \frac{2\left[5(Fr_0')^2 + 6(Fr_0')^{4/3} + 3(Fr_0')^{2/3} + 1\right]}{3\left[6(Fr_0')^{4/3} + 3(Fr_0')^{2/3} + 1\right]} \tag{3.3.15}$$

$$I_2 = 2\left[(Fr_0')^{-2/3} - 1\right] \tag{3.3.16}$$

$$I_3 = \frac{0.3\left[5 + 255\ (Fr_0')^{13/6} - 221\ (Fr_0')^2 - 39\ (Fr_0')^{17/6}\right]}{\left[1 - (Fr_0')^{2/3}\right]^3 \cdot \left[6(Fr_0')^{4/3} + 3(Fr_0')^{2/3} + 1\right]} \tag{3.3.17}$$

These relationships differ from those given by Keulegan [22, 24] and the difference increases as the value of Fr_0' decreases, particiularly below 0.4 (Figure 3.2). In Figure 3.2 Keulegan's [22, 24] nondimensional curve for the arrested saline wedge is compared with the theoretical set of curves given by Equation (3.3.14). Keulegan [22, 24] used a limited range of variation for Fr_0', something that misled him to the conclusion that the wedge shape is independent of Fr_0' and function of only the relative distance, x/L, i.e.,

$$\frac{h_s}{h_{sc}} = f\left(\frac{x}{L}\right) \tag{3.3.18}$$

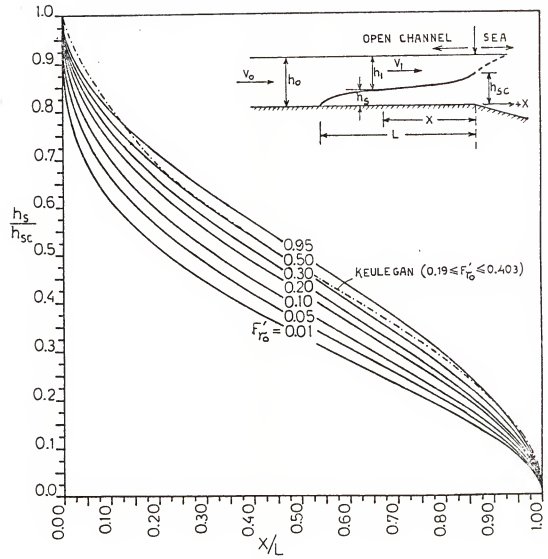

Figure 3.2 Dimensionless shape of arrested saline wedges

Source: [31]

For values of x/L between 0.2 and 0.6, there is satisfactory agreement between the theoretical and experimental data, when Fr_0' takes the values used in Keulegan's experiments [22].

b. Salt water layer

The integral form of Equation (3.3.1) over a cross section of the lower layer, $A_s = bh_s$, is

$$\int_{A_s} \frac{\partial u^2}{\partial x}\, dA + \int_{A_s} \frac{\partial (uv)}{\partial y}\, dA = -g \frac{dz_0}{dx} \int_{A_s} dA$$

$$- \frac{1}{\rho + \Delta\rho} \int_{A_s} \frac{\partial p}{\partial x}\, dA + \frac{1}{\rho + \Delta\rho} \int_{A_s} \frac{\partial \tau_{zx}}{\partial z}\, dA$$

$$+ \frac{1}{\rho + \Delta\rho} \int_{A_s} \frac{\partial \tau_{yx}}{\partial y}\, dA \qquad (3.3.19)$$

where the integrals are given by the following relations:

$$\int_{A_s} \frac{\partial u^2}{\partial x}\, dA = \beta b \frac{d(V_i^2 h_s)}{dx} - bV_i^2 \frac{dh_s}{dx} \qquad (3.3.20)$$

where

$$\beta V_i^2 A_s = \int_{A_s} u^2 dA \qquad (3.3.21)$$

and β is again the momentum correction coefficient.

$$\int_{A_s} \frac{\partial(uv)}{\partial y}\, dA = bV_i^2 \frac{dh_s}{dx} + bV_i v_s \tag{3.3.22}$$

For a pressure distribution given by

$$p = p_0 + (h - h_s)\rho g + g(\rho + \Delta\rho)\ (h_s - y) \text{ for } y < h_s \tag{3.3.23}$$

the pressure distribution integral becomes

$$\frac{1}{\rho + \Delta\rho} \int_{A_s} \frac{\partial p}{\partial x}\, dA = \frac{\rho g b h_s}{\rho + \Delta\rho} \frac{dh_1}{dx} + g b h_s \frac{dh_s}{dx} \tag{3.3.24}$$

Finally, the shear stress integral has the form

$$\frac{1}{\rho + \Delta\rho} \left[\int_{A_s} \frac{\partial \tau_{zx}}{\partial z}\, dA + \int_{A_s} \frac{\partial \tau_{yx}}{\partial y}\, dA \right] = \frac{b(\tau_i + \tau_0)}{\rho + \Delta\rho} \tag{3.3.25}$$

Equation (3.3.19) thus takes the form

$$\frac{\rho}{\rho + \Delta\rho} \frac{dH}{dx} + \frac{\Delta\rho}{\rho + \Delta\rho} \frac{d(h_s + z_0)}{dx} + \frac{\beta}{gh_s} \frac{d(V_i^2 h_s)}{dx} + \frac{V_i v_s}{gh_s}$$

$$- \frac{\tau_i + \tau_0}{g(\rho + \Delta\rho)h_s} = 0 \tag{3.3.26}$$

which, upon integration from -L to 0 neglecting $V_i v_s / gh_s$, reduces to

$$\frac{T_i}{\rho V_0^2} + \frac{T_0}{\rho V_0^2} = \frac{gh_0}{V_0^2} \overline{\frac{dH}{dx}}\, I_4 + \frac{g \frac{\Delta\rho}{\rho}}{2V_0^2 L} h_{sc}^2 +$$

$$+ \frac{g \frac{\Delta\rho}{\rho} h_0}{V_0^2} \frac{\overline{dz_0}}{dx} I_4 + \beta\left(1 + \frac{\Delta\rho}{\rho}\right)\left(\varepsilon \frac{V_{1c}}{V_0}\right)^2 \frac{h_{sc}}{L} \tag{3.3.27}$$

Here T_0 is the average bed shear stress over the length of the wedge, $(\overline{dz_0})/(\overline{dx}) = -S_0$ is the average bottom slope, $\varepsilon = (V_i)/(V_0)$, V_{1c} is the fresh water critical velocity at $x = 0$ and I_4 is an integral given by

$$I_4 = \frac{\left[1 - (Fr_0')^{2/3}\right]\left[10(Fr_0')^{4/3} + 4(Fr_0')^{2/3} + 1\right]}{3\left[6(Fr_0')^{4/3} + 3(Fr_0')^{2/3} + 1\right]} \tag{3.3.28}$$

The analysis to this point is valid for complete intrusion, that is for cases where the salt water depth at the ocean end of the channel is critical and equal to h_{sc}. It is similar in principle to the analysis used by Keulegan [22, 24] with the following differences: (1) a more detailed analytical equation for the wedge profile has been used instead of one single experimental curve and (2) the actual measured values of α and β for each experiment were used, instead of the constant values of $\alpha = 1.028$ and $\beta = 0.146$ used by Keulegan [22, 24]. Figure 3.3 gives graphically the integrals I_1, I_2, I_3, I_4. Moreover, it gives the integrals I_R [Equation (6.4.1)] and I_5, I_6 [Equations (A.3) and (A.4) of the Appendix].

3.4 Integration of the Equations of Motion: Partial Intrusion

This is the case where only part L_0 of the arrested saline wedge L is in the channel (Figure 3.4). This case will be discussed in Chapter V.

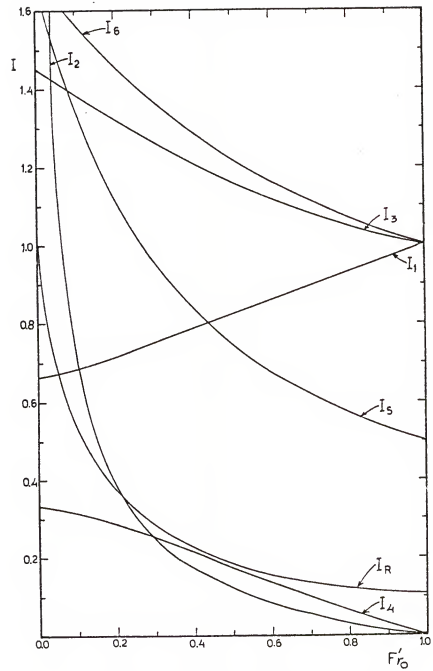

Figure 3.3 Variation of the integrals I with respect to Fr'_0

a. Fresh water layer

Replacing in Equation (3.3.12) h_1 by $h-h_s$ and dividing both members by V_0^2 the following equation is obtained:

$$\frac{\tau_i}{\rho V_0^2} = -\frac{gh_1}{V_0^2}\frac{dH}{dx} - \frac{\alpha h_1}{2V_0^2}\frac{dV_1^2}{dx} - \frac{f_w h_1 V_1^2}{4bV_0^2} \tag{3.4.1}$$

which can also be written in the form

$$\frac{\tau_i}{\rho V_0^2} = -\frac{gh_1}{V_0^2}\frac{dH}{dx} - \frac{\alpha h_0}{V_0}\frac{dV_1}{dx} - \frac{f_w h_1 V_1^2}{4bV_0} \tag{3.4.2}$$

In Equation (3.4.2), the Blasius equation

$$f_w = \frac{0.316}{Re^{0.25}} \tag{3.4.3}$$

is next introduced, where the Reynolds number, Re, is given by

$$Re = \frac{4V_1 R_{h1}}{\nu} \tag{3.4.4}$$

and where the hydraulic radius R_{h1} is

$$R_{h1} = \frac{bh_1}{(b + 2h_1)} \tag{3.4.5}$$

Thus, Equation (3.4.2) takes the form

$$\frac{\tau_i}{\rho V_0^2} = -\frac{gh_1}{V_0^2}\frac{dH}{dx} - \frac{\alpha h_0}{V_0}\frac{dV_1}{dx} - \frac{0.0559}{b^{1.25}} h_0^2 \left(\frac{\nu}{V_0 h_0}\right)^{0.25}$$

$$\cdot \frac{(b + 2h_1)^{0.25}}{h_1} \qquad (3.4.6)$$

The last equation, integrated from $-L_0$ to 0 (Figure 3.4), takes the form

$$\frac{T_i}{\rho V_0^2} = -\frac{g\overline{h_1}}{V_0^2} \cdot \overline{\frac{dH}{dx}} - \frac{\alpha h_0}{h_{10}} \cdot \frac{h_{s0}}{L_0}$$

$$- \frac{0.0559}{b^{1.25}} h_0 \left(\frac{\nu}{V_0 h_0}\right)^{0.25} \overline{\left[\frac{(b + 2h_1)^{0.25}}{h_1}\right]} \qquad (3.4.7)$$

where

$$\overline{h_1} = \frac{1}{L_0}\int_{-L_0}^{0} h_1 dx \qquad (3.4.8)$$

and

$$\overline{\left[\frac{(b + 2h_1)^{0.25}}{h_1}\right]} = \frac{1}{L_0}\int_{-L_0}^{0} \frac{(b + 2h_1)^{0.25}}{h_1}\, dx \qquad (3.4.9)$$

Here T_i is the average value of the interfacial shear stresses over the actual length of intrusion, L_0. The integrals of Equations

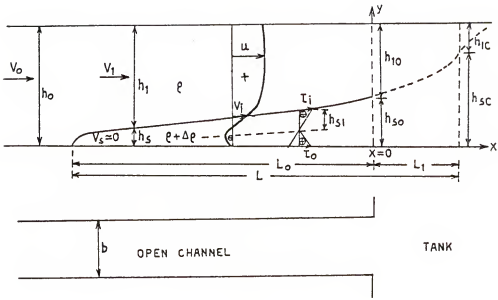

Figure 3.4 Definition sketch for partial intrusion of an arrested saline wedge

(3.4.8) and (3.4.9) have been computed by numerical integration on the basis of the trapezoidal rule.

b. Salt water layer

Equation (3.3.26), after neglecting the bottom slope, is first written in the form

$$\frac{\tau_i}{\rho V_0^2} + \frac{\tau_0}{\rho V_0^2} = \frac{g h_s}{V_0^2} \cdot \frac{dH}{dx} + \frac{(\Delta\rho/\rho) g h_s}{V_0^2} \cdot \frac{dh_s}{dx}$$

$$+ \frac{\beta(1 + \Delta\rho/\rho)\, \varepsilon^2}{V_0^2} \cdot \frac{d(V_1^2 h_s)}{dx} \qquad (3.4.10)$$

Integration of the last equation from $-L_0$ to 0 gives

$$\frac{T_i}{\rho V_0^2} + \frac{T_0}{\rho V_0^2} = \frac{\overline{g h_s}}{V_0^2} \cdot \frac{\overline{dH}}{dx} + \frac{(\Delta\rho/\rho) g}{2 V_0^2} \cdot \frac{h_{s0}^2}{L_0}$$

$$+ \frac{\beta(1 + \Delta\rho/\rho)\, \varepsilon^2 V_{10}^2}{V_0^2} \cdot \frac{h_{s0}}{L_0} \qquad (3.4.11)$$

where the integral

$$\overline{h_s} = \frac{1}{L_0} \int_{-L_0}^{0} h_s dx$$

has been computed by numerical integration.

c. Equations for T_i and T_0

For a direct evaluation of T_i and T_0 by Equations (3.4.7) and (3.4.11), a reliable measurement of the average slope of the piezometric line, $\overline{dH/dx}$, is required. This was, in fact, the procedure followed by Keulegan in his early studies [22, 24]. The experimental measurement of $\overline{dH/dx}$, however, has been found to be very difficult, since the head loss over the effective length of the flume is normally of the order of a few tenths of a millimeter. Attempts to measure that head loss optically through a laser beam required an excessively long time due primarily to the slowness of achieveing equilibrium in the two static tanks, as well as to a number of factors affecting the measurements. Moreover, the above equations are quite sensitive to $\overline{dH/dx}$ so that a measurement error of the order of 10 percent may cause an error in T_i of the order of 50 percent.

This difficulty was bypassed by assuming a linear shear stress distribution in the lower layer. Indeed, the shear stress distribution within the wedge is given by the equation

$$\frac{\partial \tau}{\partial y} = \frac{\partial}{\partial x}\left[p + g(\rho + \Delta\rho)z_0 + (\rho + \Delta\rho)\frac{u^2}{2}\right] \qquad (3.4.13a)$$

The velocity head is very small and can be neglected; then, introducing p from Equation (3.3.23), we get

$$\frac{\partial \tau}{\partial y} = \rho g \frac{dH}{dx} + \Delta\rho g \frac{\partial(h_s + z_0)}{\partial x} \qquad (3.4.13b)$$

The free surface slope dH/dx is very small, as has been discussed, and can be considered as constant. Also, apart from two relatively small segments around the wedge toe and the critical section, the interface is very nearly a plane surface and $[d(h_s + z_0)]/(dx)$ is also very nearly constant. Therefore, it is reasonable to assume linear variation of τ with y within the wedge. From Figure 3.4 it follows that

$$\frac{\tau_i + \tau_0}{\tau_i} = \frac{h_s}{h_{s1}} = \lambda \tag{3.4.14}$$

where h_{s1} is the distance from the interface to the point of maximum velocity in the wedge. Assuming next that λ is independent of x, the following simple relation for the average shear stresses T_i and T_0 is obtained

$$T_i + T_0 = \lambda T_i \tag{3.4.15}$$

Elimination of the mean slope of the free surface, $\overline{dH/dx}$ from Equations (3.4.7) and (3.4.11) and replacement of T_0 by $T_i(\lambda - 1)$ in Equation (3.4.15) leads to the equation

$$\frac{T_i}{V_0^2} = \left[\frac{\left[(\Delta\rho/\rho) g h_{s0} + 2\beta(1 + \Delta\rho/\rho)\, \varepsilon^2 V_{10}^2\right] h_{10} \overline{h_1}}{2V_0^2 h_{10}(\lambda \overline{h_1} + \overline{h_s})} - \frac{2\alpha V_0^2 h_0 \overline{h_s}}{2V_0^2 h_{10}(\lambda \overline{h_1} + \overline{h_s})} \right] \cdot \frac{h_{s0}}{L_0} - \frac{0.0559}{b^{1.25}} h_0^2 \left[\frac{\nu}{V_0 h_0}\right]^{0.25} .$$

$$\cdot \left[\frac{\overline{(b + 2h_1)^{0.25}}}{\overline{h_1}}\right] \cdot \frac{\overline{h_s}}{(\lambda\overline{h_1} + \overline{h_s})} \qquad (3.4.16)$$

All the terms of the second member of Equation (3.4.16) are either known or can be directly measured. With T_i known the average bed shear stress can be evaluated by means of Equation (3.4.15).

For infinite channel width and for $T_0 = 0$, Equation (3.4.16) becomes

$$\frac{T_i}{\rho V_0^2} = \left[\frac{(\Delta\rho/\rho)\ g\overline{h_1}h_{s0}}{2V_0^2 h_0} - \frac{\alpha h_s}{h_{10}}\right] \frac{h_{s0}}{L_0} \qquad (3.4.17)$$

The corresponding friction coefficient, f_i, in this case should be similar to the one given by Schijf and Schönfeld's model [37].

The analysis presented in section 3.3 constitutes an improvement as compared to Keulegan's original approacn [22, 24], particularly since it eliminates the need of measurement of $\overline{dH/dx}$ and since it takes into consideration partial intrusion.

The expected relative error in the estimate of λ is considerably lower than the error for $\overline{dH/dx}$, while the error in the estimate of shear stresses is smaller than that for λ [Equation (3.4.16)].

CHAPTER IV
EXPERIMENTAL APPARATUS AND INSTRUMENTATION

4.1 Introduction

The experimental salinity intrusion flume was designed at the University of Thessaloniki, in Greece, and at the University of Florida, in Gainesville, by Dr. Partheniades and the author. This apparatus was constructed at the Coastal and Oceanographic Laboratory of the latter university.

The construction of the flume started in the summer of 1977 and was completed in the fall of 1978, with the exception of some minor details which were completed in the beginning of 1979.

The apparatus basically consists of a variable slope plexiglass flume, the associated fresh water and salt water tanks, and the fresh water circulation system.

The main measuring instruments were the hot film anemometers, a specially designed electronic conductivity meter and the orifice meters.

4.2 The Main Experimental Apparatus

In laboratory studies on salt water intrusion a constant salinity water basin has to be maintained at the downstream end of the channel. This is rather difficult, requiring excessively large dimensions. For example, Keulegan [24] recommends a basin width equal to ten times the channel width and a basin length equal to twenty times the

channel length. Space limitations, however, impose severe restrictions.

Therefore, the following apparatus has been designed and constructed as a best compromise between the ideal requirements and the physical and technical limitations. That apparatus is outlined in Figure 4.1 and consists of a variable slope open channel with the necessary tanks and other accessories. The channel has a width of 45.7 cm and a length of about 20.0 m, so that an adequate length of salt water intrusion could form inside the channel. Moreover, the toe of the wedge should not exceed a certain distance from the upstream end of the channel, otherwise significant mixing could take place. The results of such a mixing, which has been observed in some experiments, is the development of three or more layers and the destruction of the sharp interface.

For large Reynolds numbers, large mean fresh water velocities and large cross sectional dimensions are required; however, physical limitations impose restrictions on both variables. Considering the mean fresh water velocity, there is the additional restriction on the interfacial shear stresses. These stresses must be lower than an upper limit, to avoid high rates of entrainment. In the case of small entrainments with still distinct interface, Keulegan [22, 24] defined a critical velocity, V_c, for the moving layer. For a mean velocity larger than the critical one, mixing is expected to take place at significant rates. In many experiments in the present study the mean fresh water velocity was larger than V_c; however, the interface remained distinct.

Finally, a rectangular cross section 45.7 cm x 45.7 cm (18 in x 18 in) and a length of 20.24 m (66.5 ft) have been selected. The bottom and the walls of the channel have been constructed of transparent plexiglass 1.27 cm (0.5 in) thick.

The channel is supported on a steel frame (Figures 4.1, 4.2, 4.3, and 4.4) through a plywood board. To allow free expansion and contraction due to temperature changes, the upstream end of the channel was free while the downstream end was connected with the fixed tank, T_1, through a 5 cm long thick rubber forming a flexible and waterproof hinge. In addition to the free slippage of the channel, this connection also permitted a rotation of the channel around the joint, B (Figure 4.1), when the slope was varied.

The channel has been constructed in parts of 2.5 m length, placing a rubber tape 2 mm thick between them. For cross sectional rigidity vertical sidewall supports and cross bars over the channel have been provided.

The steel frame is supported on the joint B and on two hydraulic jacks, one at the center and the other at the upstream end of the channel. Through a gear-chain, the central jack could be moved up and down over a height equal to one-half that of the upstream jack. In this way, a variation of the slope of the channel up to 4 $^{o}/_{oo}$ is possible while a special gauge installed near the upstream jack measures the change of the elevation of the bottom of the channel with an accuracy of one hundredth of an inch.

Tank T_1 (Figures 4.1, 4.2, 4.3, and 4.4) was used as a salt water tank. Its bottom and its three sidewalls are made of steel and

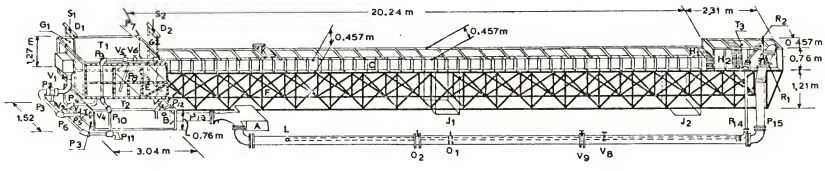

A = Axial Pump
B = Joint
C = Open channel
D = Disk
E = Steel plate
F = Steel frame
G = Gate
H = Honeycombed section
J = Jack
K = Carriage
L = Connection of Return pipes
O = Orifices
P = Pipe
R = Air cock
S = Endless screws
T = Tank
V = Valve

Figure 4.1 Main experimental apparatus

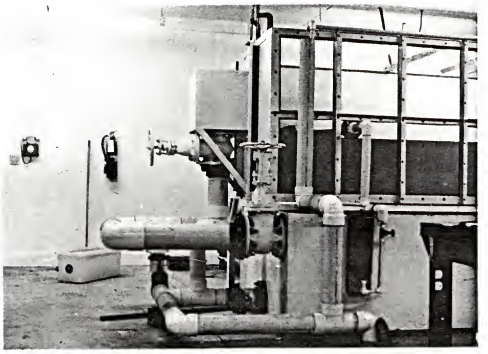

Figure 4.2 Downstream side of the apparatus

Figure 4.3 Front view of the apparatus

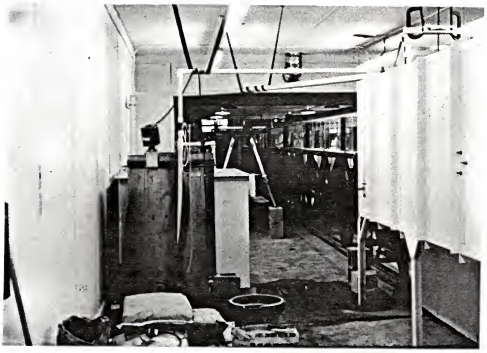

Figure 4.4 Rear view of the apparatus

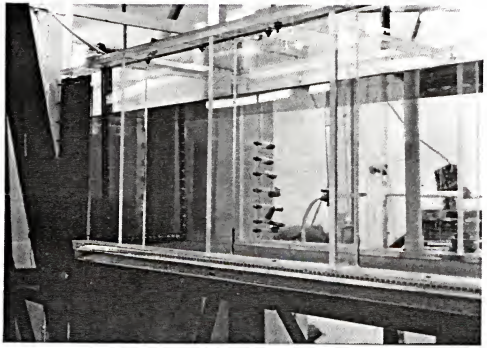

Figure 4.5 Rear view of the apparatus with gate

the fourth sidewall is made of transparent plexiglass 1.27 cm (0.5 in) thick. This permits a macroscopic control of mixing of the two layers in the tank as well as a control of the salt water elevation. The continuous observation of the interface level is necessary for good operation. This level should not be lower than the channel bottom. The tank was operated like a two-layered wide channel with the upper layer moving over a quasi-stagnant lower layer.

The tank length is 3 m and its depth is 1.3 m. The steel parts of the tank were covered with insulating coating and were subsequently painted by plastic dye.

To eliminate the disturbance of stratified flow at the entrance of the tank due to the abrupt change of the depth, a steel plate E was used (Figures 4.1 and 4.3). The slope of the plate to the horizontal direction is 32.5 degrees. The tank has two plexiglass gates G_1 and G_2 (Figures 4.1, 4.2, and 4.3) at its downstream and the upstream ends. Gate G_1 regulates the two-layer system in the channel. Pipe P_1 transports fresh water to the recirculation tank T_2. The upper end of P_1 is at the level of the bottom of the channel; therefore, the elevation of the interface must be higher than the upper end of P_1.

To avoid overflow of salt water, gate G_1 has a waterproof fit with the tank wall. A similar construction was used for gate G_2 at the upstream wall of the tank. Gate G_2 is waterproof and it separates the fresh water in the channel from the salt water tank before the beginning of the experiments. During the experiments gate G_2 is raised to permit the downstream flow of fresh water and the upstream motion of the salt

water. The raising and lowering of the gates is carried out by the rotation of disks D_1 and D_2. The endless screws S_1 and S_2 pass through the disks D_1 and D_2, respectively, and the screws have a fixed connection with the gates. Tank T_1 is connected to the emptying pipe P_{16}.

Tank T_2 (Figures 4.1, 4.2, and 4.3), with a length of 3.0 m and a width of 1.52 m, is used as a recirculation tank for the fresh water. The tank is connected to the axial flow pump A through the suction pipe P_{13}. An appropriate depth of water must be maintained over the crest of P_{13} for good operation without air suction. This depth and the diameter of the suction pipe determined the depth of water in T_2 to 0.75 m. The steadiness of this depth is controlled by an overflow pipe P_4. Tank T_1 has been placed on T_2 in a way that leaves a part of T_2 free. This is necessary for macroscopic control of the steadiness of the fresh water flow. The control of the fluctuation of the free water surface in T_2 in every experiment was particularly important, since this variation was significant for short time intervals. In particular, when the fresh water flow rate was increasing, the free surface of the system in the channel also increased; however, the free surface in T_2 was lowered. Therefore, there was a danger of a drop of the free surface in T_2 below the crest of pipe P_{13}. To avoid this danger, the volume of fresh water in T_2 was replenished by tap water from pipe P_{12} connected to the tap water faucet. It is recalled that, after establishing a steady flow, valve V_7 of pipe P_{12} was closed. Tank T_2 is also connected to the emptying pipe P_5 and to pipe P_3 through which fresh water is being recirculated. This tank is made of steel and it is coated and painted in the same way as tank T_1.

The fresh water is pumped into the upstream tank T_3 (Figure 4.1) from tank T_2. There the turbulence is dampened by flow through a honeycombed section. The recirculation of water takes place through pipes P_{14} of 7.6 cm diameter and P_{15} of 30.4 cm diameter, whose downstream ends are not connected to the channel. Therefore, the upstream end of the channel can be moved in the vertical direction freely. The pipes are connected at the location L and the operation of one or the other depends on the required discharge. The latter is regulated by the axial flow pump A. Each one of the pipes has an orifice meter. Orifice O_1 with a diameter D = 2.5 cm is in pipe P_{14} and orifice O_2 with a diameter D = 7.6 cm is in the pipe P_{15}.

Pipes P_1, P_2, P_3, and P_6 and valves V_1, V_2, V_3, and V_4 have an appropriate connection to drive the recirculated fresh water either to tank T_2 or to the sewer, through pipe P_{11}, when the mixing of the two layers is significant.

Pipe P_7 is branched into pipes P_8 and P_9 by an appropriate operation of valves V_5 and V_6. Pipe P_7 either drives salt water from the tank of preparation of salt water to tank T_1 through pipe P_8, or it empties the tank of preparation of saltwater through pipe P_9. In the last case the salt water is driven through the pipes P_7, P_9, P_{10}, and P_{11}. The length of pipe P_8 was so chosen that the system of pipes P_8 and P_9 operates as a reversed siphon. Therefore, to avoid the danger of salt water intrusion reaching the upstream end of the channel, the level of salt water in Tank T_1 was lowered using the reversed siphon. In this way, salt water, instead of being transferred to the sewer, was

stored in the mixing tank for a new usage during the experiment. The salt water from the mixing tank was transferred to tank T_1 by a pump.

The measuring instruments, that is the hot film anemometer probe, the conductivity meter probe and the point gauges, were supported on a carriage moving on rails (Figure 4.1).

4.3 Instrumentation

The electronic system of instruments used in this study is about the same as the one used by Powell [34]. For this reason much of this analysis on the instrumentation is basically a repetition of that given by Powell [34]. For more information see reference [34]. This system contained transducers, signal conditioners, and an analog-to-digital (A/D) tape recorder. The output signal from each transducer was passed through one or more signal conditioners and was sampled and recorded into magnetic tape by the kinemetrics Model DDS-1103 A/D tape recorder. Figure 4.7 shows the general arrangement of the instrument package.

The input voltage, being in A/D recorder between -5.0 V and +5.0 V, is resolved into 4,096 discrete values. Therefore, the input resolution for this unit was limited to $\pm$ 0.0012 V. The probes measuring temperature, conductivity, and velocity were mounted at the end of the transverse rod of the point gauges. All this system of probes and gauges were supported on the carriage. Figure 4.8 gives a general view of electronic instrumentation used in this study.

The measurement of temperature in the vicinity of the conductivity and hot film probes was obtained with the thermistor probe. That

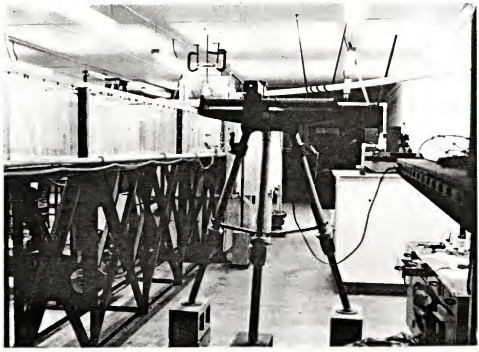

Figure 4.6 Rear view of the apparatus showing the laser instrument

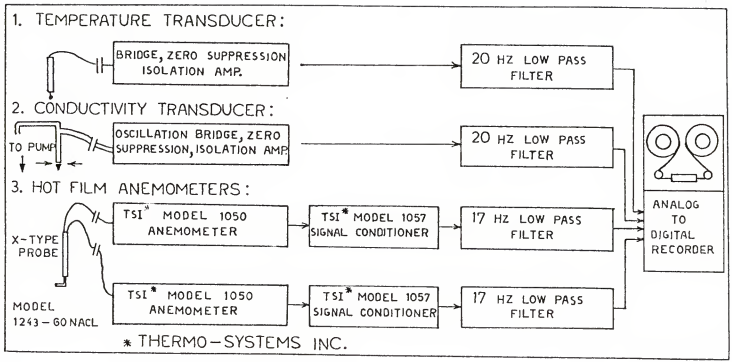
1. TEMPERATURE TRANSDUCER:
BRIDGE, ZERO SUPPRESSION ISOLATION AMP.
20 HZ LOW PASS FILTER
2. CONDUCTIVITY TRANSDUCER:
TO PUMP
OSCILLATION BRIDGE, ZERO SUPPRESSION, ISOLATION AMP.
20 HZ LOW PASS FILTER
3. HOT FILM ANEMOMETERS:
X-TYPE PROBE
TSI* MODEL 1050 ANEMOMETER
TSI* MODEL 1057 SIGNAL CONDITIONER
17 HZ LOW PASS FILTER
MODEL 1243-60 NACL
TSI* MODEL 1050 ANEMOMETER
TSI* MODEL 1057 SIGNAL CONDITIONER
17 HZ LOW PASS FILTER
ANALOG TO DIGITAL RECORDER
* THERMO-SYSTEMS INC.

Figure 4.7 Black box schematic outline of instrumentation

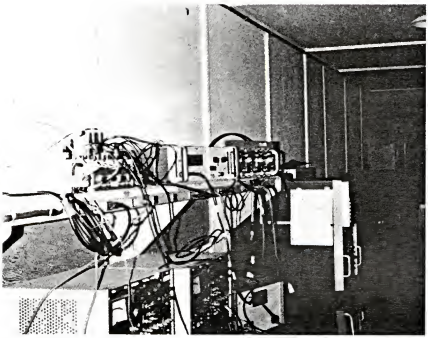

Figure 4.8 Outline of electronic instrumentation

probe, Model SF2-42A68, manufactured by Victory Engineering Company, has a sensor of 1.5 mm in diameter. The output from the thermistor was passed through a low-pass filter with a cutoff frequency of 20 Hz. The output from the filter was recorded by the A/D recorder.

The density at any point of the cross section of the stratified system was determined by the conductivity and temperature. The conductivity meter used in this study was designed by Doddington [38] and constructed in the Engineering Sciences Laboratory of the University of Florida in Gainesville (Figure 4.9). It is made of acrylic plastic and has one stainless steel and one platinum electrode. During its operation, the surrounding fluid is continuously drawn into the interior chamber through a 0.5 mm slit and a 0.3 mm diameter vertical hole at the bottom of the probe. The fluid exits through the plastic tube connecting the probe and the vacuum pump. The electrical current density between the electrodes is small except in the vertical hole, where it becomes large. Thus, the resistance between the electrodes at any instant is governed by the conductivity of the fluid in the vertical hole, not by the resistance at the fluid-electrode interface. This reduces the effects caused by electrode contamination and plating. For more details about the conductivity meter see Sheppard and Doddington [38]. The vacuum pump should work on low suction pressures to have small flow rates through the probe. An indicative maximum flow rate is about 30 cm^3/min, which does not affect the conductivity.

The output voltage from this transducer becomes again the input to a low-pass filter with a 20-Hz cutoff frequency and the output from the filter is also recorded digitally on a magnetic tape.

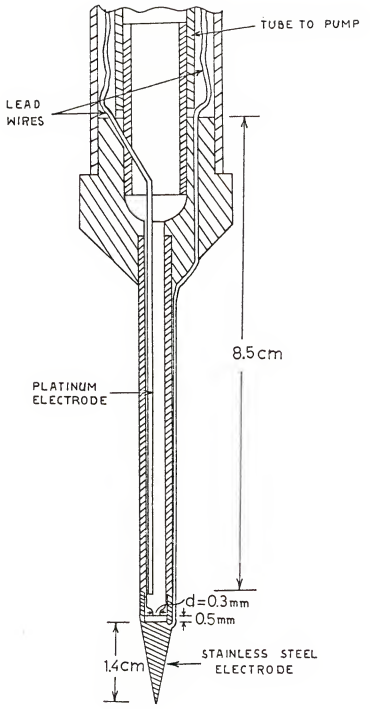

Figure 4.9 Cross section of conductivity probe

Source: [38]

A hot film anemometer with constant temperature, Thermo-system Model 1050 general purpose anemometer, was used to measure both the mean velocity and the fluctuating components of velocity in the plane of the sensors. The two sensors are part of an x-type hot film probe, Thermo-system Model 1243-60w NaCl.

The output from each anemometer is first passed to a thermosystems Model 1057 signal conditioner. This conditioner suppresses the excessive DC voltage to make the signal compatible with the input requirements of the A/D recorder. From the conditioner the signal is sent to a low-pass filter with a cutoff frequency of 17 Hz and from there the signal goes to the A/D recorder where it is ditigized and recorded onto a magnetic tape.

The overheating ratio is given as

$$\frac{R_H}{R_e} = 1 + \alpha_c(t_s - t_e) \tag{4.3.1}$$

where R_H is the operational resistance of the sensor, R_e is the sensor resistance in environmental temperature, α_c is the temperature coefficient, t_e is the environmental temperature, and t_s is the operational temperature of the sensor. For the hot film used in this study the value of α_c is 0.0026/°C. To avoid creation of bubbles on the sensors by the high temperature, an overheat ratio of $R_H/R_e = 1.05$ was chosen.

To transform the output voltage into flow velocity, King's law has been used. That law reads

$$E^2 = \left[A + B(\rho u)^{1/n}\right](t_s - t_e) \tag{4.3.2}$$

where A and B are constants depending on the temperature, u is the fluid velocity, 1/n was taken equal to 0.45, and E is the output voltage.

The low-pass filters were used to prevent contamination of the signal by high frequency noise, particularly 60-cycles noise, which is picked up from the large pumps, electric motors, and other support equipment in the laboratory. Spectral analysis of the velocity data, done by Powell [34], has indicated that for these experiments negligible energy exists above 7 Hz; therefore, these low pass filters have little or no effect on the true signal from their respective transducers.

In addition to the aforementioned electronic instrumentation, some other instruments were used, such as orifices, thermometers, and pycnometers.

CHAPTER V
EXPERIMENTAL PROCEDURE AND CALIBRATION OF THE INSTRUMENTS

5.1 Introduction

The hydrodynamic behavior of arrested saline wedges has been studied by using fresh and salt water, with the latter dyed by a red food color dye. The relative density difference, $\Delta\rho/(\rho + \Delta\rho)$, ranged from 8 $^{o}/_{oo}$ to 93 $^{o}/_{oo}$.

The following primary parameters were independently varied: (1) the fresh water flow rate, Q, (2) the ratio $\Delta\rho/(\rho + \Delta\rho)$, and (3) the fresh water depth, h_0, upstream of the wedge.

Each group of experiments was conducted during a day and was preceeded by the following stages of preparatory work:

1. Preparation of the salt water in the mixing tank. The salt water was subsequently transferred to tank T_1 up to the desirable depth (Figure 4.1). Gate G_2 was closed during this phase
2. Calibration of the electronic instruments. When the measurement duration was more than 10 to 12 hours, a checking of the instruments calibration was necessary, particularly for the hot film sensors and the thermistor
3. Placing and fixing of the probes on the carriage K (Figure 4.1)

4. Gate G_2 was raised and the operation of axial pump A was started at the same time (Figure 4.1). The measurements started a few hours after the onset of flow to allow the establishment of the maximum degree of steadiness.

The preliminary work usually started at seven o'clock in the morning and ended early in the afternoon. The main experiments followed right afterwards. The fresh water flow rate was measured through orifices O_1 and O_2; next, the total depth of the two layers, the length of salt water intrusion, and the depth of the saline wedge at every meter of length were determined. Finally, the instantaneous velocities, conductivities, and temperatures at several points in a selected cross-section were measured.

5.2 Preparation of the Salt Water in Tank T_1

The fresh water, the salt, and the dye were mixed in the mixing tank until a uniform salt water mixture of the desirable density was obtained. The mixing tank volume was about one cubic meter. For this reason and before starting the experiments, some time was necessary to fill tank T_1 up to the required depth. A volume equal to seven times the volume of the mixing tank was required.

According to Equations (3.4.16) and (3.4.17), the length of salt water intrusion in the channel, L_0, is an increasing function of the depth at the mouth of the channel, h_{10}, and a decreasing function of the average interfacial shear stress T_i. Therefore, an approximate estimate

of h_{s0} was necessary so that L_0 would be less than the length of the channel. This was made possible by a rough calculation of an arrested saline wedge with a length of intrusion equal to L_0 (Figure 3.4).

For values of h_0 equal to or less than 10 cm, the levels of free surfaces of the fresh and salt water on the respective side of gate G_2 were approximately the same. For values of h_0 higher than 15 cm the fresh water level was higher than the salt water level by a depth h_g. This was done in order to avoid any disturbance of the flow at the position of gate G_2 at the start of the experiment due to an unbalanced pressure force. The operation in this case was the following: The depth h_g was approximately estimated and tank T_1 was filled with salt water up to the bottom of the channel. Then the axial pump was started at very small discharge to fill the channel and the tank T_1 to a depth h_g above the bottom of the channel. During this operation valves V_1 and V_2 remained closed, gate G_2 remained open, and gate G_1 was lifted to a height determined on the basis of the desirable depth h_0 upstream of the wedge. Fresh water was replaced in tank T_2 during pumping through pipe P_{12}. When the fresh water depth in tank T_1 was equal to h_g, gate G_2 was closed while fresh water was supplied to the channel and salt water was supplied to the tank T_1 from the mixing tank through pipe P_8. The discharge of pipe P_8 was small in the beginning to avoid any interfacial mixing and it was increased later on. When the depth of fresh water was approximately equal to the desirable depth, any supply of fresh or salt water was ceased. To avoid any mixing of fresh water in the channel and the salt water in tank T_1 due to a possible small leakage through gate G_2,

another gate G_3 was installed, as shown in Figure 4.1. The thermistor and the hot film sensors were next calibrated.

5.3 Calibrations

The thermistor was calibrated through a mercury thermometer with a resolution of ± 0.05 degrees Celcius (°C), assumed to be the same as the resolution of the thermistor.

Each calibration curve corresponds to a daily series of experments. In the curve of Figure 5.1 a small degree of nonlinearity can be observed. However, the linearization of the curve on the basis of the method of least squares error gives an error less than ± 0.1°C.

The hot film anemometer sensors were calibrated through a Thermosystems, Inc. calibrator for water, Model 1127.

Figure 5.2 gives typical calibration curves for the two sensors of an experimental day.

The method of least squares error was applied again for the correlation curves and the square of correlation coefficient was of the order of 99.9 percent. Otherwise, the relative error between the real velocities and the corresponding values on the calibration curve would be, at least, of the order of 10 percent. It follows from Figure 5.2 that for small velocities, the correlation is nonlinear; however, we can accept the linearity for velocities as low as 3.0 mm/sec.

Figure 5.3 gives a partial view of the instruments used for the calibration of the thermistors and the sensors.

The conductivity probes were calibrated just prior to the experimental work and the calibration curves were frequently checked during

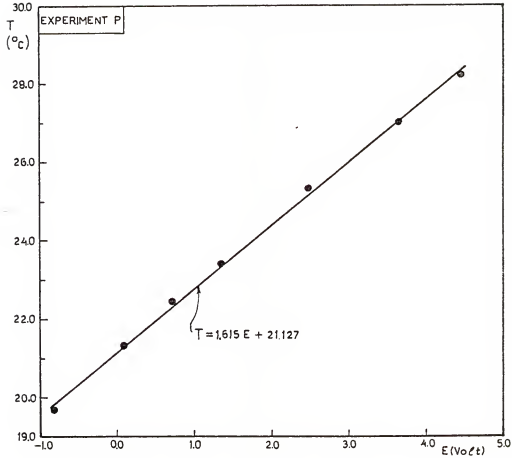

Figure 5.1 Calibration curve for the thermistor

the conduct of each experiment. The calibration was repeated after five months in order to detect the time effect on the probe. That effect was found to be negligible.

The calibration started with the correlation of the output of the probe with the relative density difference $\Delta\rho/(\rho + \Delta\rho)$ and with temperature (Figure 5.4). The ratio of $\Delta\rho/(\rho + \Delta\rho)$ in the first calibration ranged from 5 $^{o}/_{oo}$ to 40 $^{o}/_{oo}$ and in the second one from 5 $^{o}/_{oo}$ to 85 $^{o}/_{oo}$. The temperature ranged from 14.5°C to 29°C. The variation of $\Delta\rho/(\rho + \Delta\rho)$ with the temperature was approximately linear. Through the application of the method of least squares error, the following relation was derived first for a temperature of 20.4°C (Figure 5.5) and later on extended to any temperature.

$$\frac{\Delta\rho}{(\rho + \Delta\rho)} = - 0.0031 + 0.087E - 0.00067\ (T - 20.4) \qquad (5.3.1)$$

where E is the probe output in volts, T is the temperature in degrees centigrade, and $\Delta\rho/(\rho + \Delta\rho)$ is given per thousand ($^{o}/_{oo}$). Equation (5.3.1) is applicable only for $\Delta\rho/(\rho + \Delta\rho) \leqq 40$ $^{o}/_{oo}$. The calibration curve for $\Delta\rho/(\rho + \Delta\rho)$ larger than 40 $^{o}/_{oo}$ is given in Figure 5.6. In this figure, the calibration curve for $\Delta\rho/(\rho + \Delta\rho) > 40$ $^{o}/_{oo}$ has the form

$$\frac{\Delta\rho}{(\rho + \Delta\rho)} = - 0.0021 + 0.125E - 0.00067\ (T - 20.4) \qquad (5.3.2)$$

and the calibration curve for $\Delta\rho/(\rho + \Delta\rho) \leqq 40$ $^{o}/_{oo}$ has the form

$$\frac{\Delta\rho}{(\rho + \Delta\rho)} = - 0.0032 + 0.0875E - 0.00067\ (T - 20.4) \qquad (5.3.3)$$

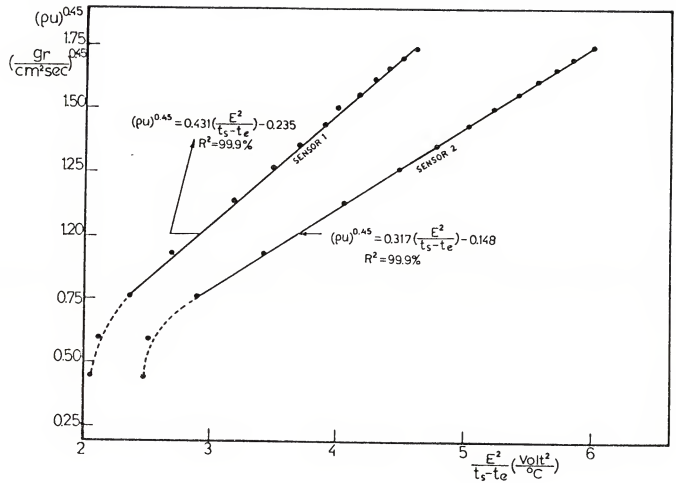

Figure 5.2 Calibration of hot film sensors

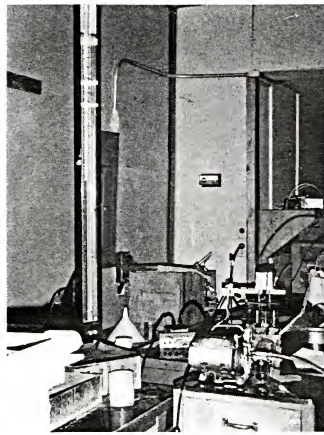

Figure 5.3 Instruments used for calibration of thermistor and sensor

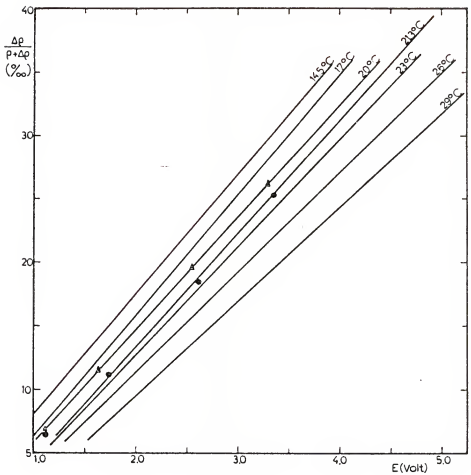

Figure 5.4 Calibration curves for the conductivity probe for various temperatures

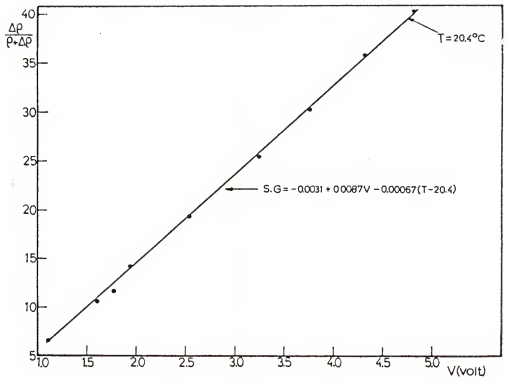

Figure 5.5 Calibration of the conductivity probe for T = 20.4° C

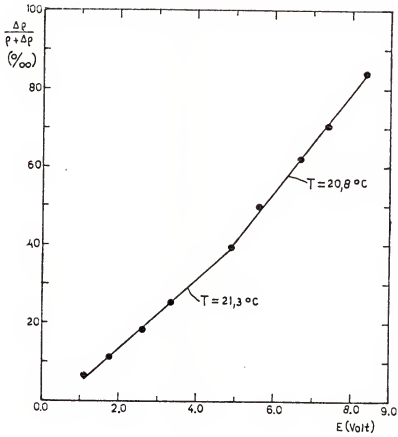

Figure 5.6 Calibration of the conductivity probe for $\Delta\rho/(\rho + \Delta\rho)$ up to 85 ‰

The difference between Equations (5.3.1) and (5.3.3) appears to be neglibible. Therefore, the time had no serious effect on the conductivity probe. The curves of Figure 5.6 have different slopes because the conductivity meter had been designed for $\Delta\rho/(\rho + \Delta\rho) \leqq 40\ ^{o}/_{oo}$.

The calibration curves for the orifice meters were given by the company; however, they were checked in place. The continuous curve in Figure 5.7 is the company's calibration, while the points correspond to the experimental check. After linearizing the given curves, application of the method of the least squares error led to the calibration formulas

$$Q = 0.0048(\Delta h)^{0.488} \tag{5.3.4}$$

for the orifice with a diameter D = 2.5 cm and

$$Q = 0.0711(\Delta h)^{0.499} \tag{5.3.5}$$

for the orifice with a diameter D = 7.6 cm. Here Δh is expressed in meters of mercury column and Q in m^3/sec.

A figure similar to Figure 5.7 was obtained for the orifice with diameter D = 7.6 cm.

5.4 The Placing of the Instruments on the Carriage

After their calibration, the thermistor and the hot film probe were attached to the shaft of one point gauge while the conductivity probe was attached to the shaft of a second point gauge. These gauges were permanently supported on the carriage K (Figure 4.1). The horizontal distance between the hot film probe and the thermistor was about 2 cm

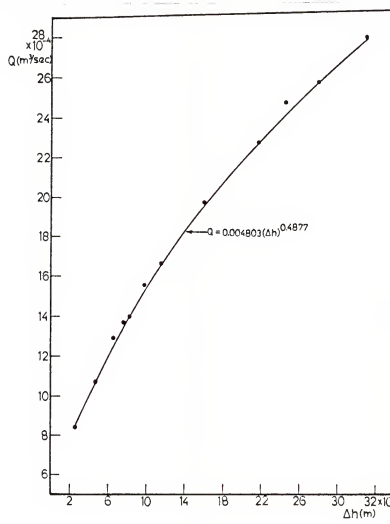

Figure 5.7 Orifice calibration curve for D = 2.5 cm

and that between the hot film and conductivity probe was about 8 cm. Thus, the high frequency fluctuations of temperature at the position of the thermistor and of conductivity at the position of the conductivity probe were not affected by the high frequency fluctuations of temperature and density in the neighborhood of the hot film sensors. The existence of such fluctuations introduces nonexisting fluctuations in the velocity measurements.

Because temperature, density, and velocity varied with the depth, the measurements were taken at the same horizontal level. First, these instruments were leveled with respect to the horizontal surface of stagnant water. Next, the level of the bottom of the channel was determined. After all these preparatory steps, the experiments were ready to start.

Figure 5.8 shows the establishment of the level of the bottom of the channel with only fresh water in it before starting the experiments.

5.5 Experiments

The outlined preparatory steps usually took about six hours, provided that no problems were encountered in the establishment of the calibration curves of the instruments. One of the usual problems was the formation of very small air bubbles invisible to the eye on the x-type hot film probe. The existence of the bubbles was detected after the definition of calibration curve, when the square of correlation coefficient of the curve was less than 99.8 percent. In such a case, the calibration of the hot film sensors was repeated. For this reason, the preliminary work sometimes continued for more than eight hours. When the air bubbles were visible, the required time was not so long.

Figure 5.8 Establishment of bottom elevation of the channel before starting the experiments

When everything was ready, the movable gate G_3 was raised and the axial pump A was turned on with a nearly simultaneous raising of gate G_2 and an opening of valves V_1 and V_2. Valve V_4 was closed. In this way, all the fresh water discharge was driven to the sewer through the pipes P_1, P_2, P_6, and P_{11}. This was necessary because by raising gate G_2 a salt water front was formed while moving upstream (Figure 5.9). The interfacial mixing of the front was significant because the fresh water conditions had not yet reached their final steady state. Thus, the fresh water contained large quantities of salt and that violated the requirement of small entrainment and sharp interface. The mixing was normally controlled through visual observation and in certain instances through sampling from the recirculation tank T_2. The volume of fresh water in T_2 was replaced through the discharge pipe P_{12}, which was connected to the tap water faucet.

In order to maintain the toe of the saline wedge downstream of the head water tank, the fresh water flow rate and the depth of salt water at the mouth of the channel had to be properly controlled. The flow rate was controlled through the axial variable speed pump and the salt water depth at the mouth of channel was controlled through siphon P_8-P_7.

As it was pointed out earlier, the length of salt water intrusion was very sensitive to flow and salinity fluctuations; for this reason, the pump and siphon operations had to be done very carefully. When the upper layer was clear, valves V_2 (emptying the water to the sewer), V_6 (operating the siphon), and V_7 (discharging tap water) were

Figure 5.9 Upstream motion of salt water front

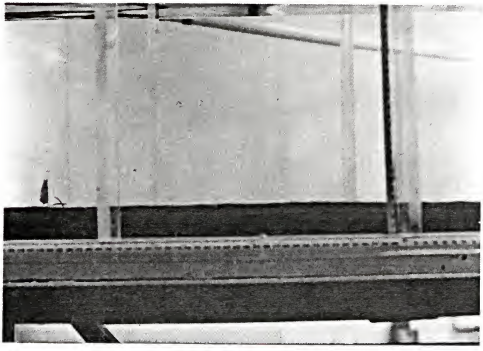

Figure 5.10 Example of smooth interface

closed while valve V_4 (through which the upper layer was transferred to tank T_2 for circulation) was opened. Next, the flow rate for each experiment was established through the axial pump (Figure 4.1). This work was difficult because the motion of salt water front had to be continuously observed and the discharge of pump A had to be properly controlled. The establishment of steady conditions required normally one hour and in certain special and extreme cases more than four hours.

The entrainment of salt water, although small, was eroding the depth of salt water and diminishing the length, L_0, of the saline wedge. For small interfacial shear stresses, the decrease of L_0 was negligible; however, for larger stresses, the erosion of the salt water layer was large and the assumption of stationary saline wedge was no longer valid. To avoid this, Tank T_1 was continuously supplied with salt water in appropriate discharges through pipe P_8. For smooth interfaces (Figure 5.10) and low mean velocity in the upper layer, the interfacial shear stresses were low and mixing was small; therefore, the depth of salt water in any cross section was approximately constant.

When the duration of the experiment was of the order of half an hour, the decrease of intrusion length, L_0, was negligible compared to the original length. Most of the experiments of series I, L, N, O, P, and many of the remaining series belong to this category.

When the mean velocity of the upper layer was large, interfacial waves appeared (Figure 5.11). For even larger velocities, these waves started breaking. The upper limit of the mean velocity of the upper layer was established from the form of wave breaking. Figure 5.12 gives

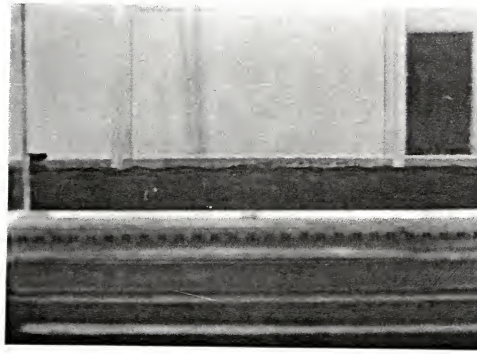

Figure 5.11 Example of wavy interface

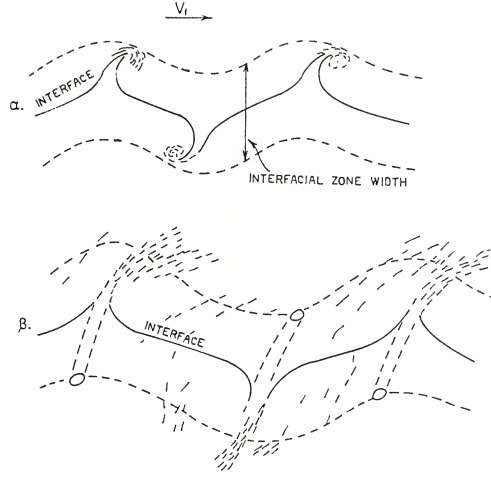

Figure 5.12 (a) Eddy formation due to the interfacial wave breaking;
(b) beginning of gradual mixing of the two layers

Source: [14]

two characteristic forms of breaking. In the first, for moderate interfacial shear stresses, a small volume of injected fluid is diffused in the upper layer, but the largest part of it is returned back to the saline layer. In this case mixing is a factor of stability. In the second case of high interfacial shear stresses, the total injected fluid in the upper or in the lower layer is almost totally diffused and mixed with the ambient water. This is the beginning of gradual mixing of the two layers. In the experiments of the present study the upper limit of mean velocity of the fresh water layer was determined by the instability of the first form (Figure 5.12).

The following flow and salinity parameters were measured: (1) the depths, h_s, of salt water intrusion in every meter of its length; (2) the salt water intrusion length, L_0; and (3) the manometer readings. These preliminary measurements were followed by the detailed measurements of velocities, temperatures, and salinities at several points of the cross section from the bottom to the free surface by the three instruments attached to the point gauges. One of the point gauges was used to establish the levels of the free surface and of the bottom, from which the depths of each layer of the system were calculated. Next, the position of the thermistor, the hot film sensors, and the conductivity probe were defined by the point gauges. The A/D recorder was turned on to record the data of velocities and conductivities on the tape. The measurements took place in a cross section within the middle third of the saline wedge. The recording was automatically stopped before continuing the measurements at another point of the cross section. Most of the

points were located around the interface and in the lower layer. In the lower part of the salt water layer the sensors were directed downstream, because in this part the salt water motion was in the upstream direction. Above this part of the lower layer the sensors were directed upstream.

For every point of the cross section, four series of data were recorded on the tape, that is, the data of the thermistor, of the conductivity meter, and of the two hot film sensors. Using the calibration curves, the I.B.M. electronic computer was transforming the data from volts to data in temperature, density, and velocities, respectively. In particular, to calculate the instantaneous velocities at a point, the temperature and the density at the point had to be known [Equation (4.3.2)].

As mentioned in the previous chapter, the high frequency fluctuations in the temperature and in the conductivity may introduce fluctuations in velocity measurements which do not actually exist. To reduce the effect of this source of errors, the time average values of temperature and density were introduced in Equation (4.3.2) instead of their instantaneous values.

In order to estimate the magnitude of errors from such a source, Powell [34] performed the following simple experiment. He determined the instantaneous velocity and all the correlations, first for constant temperature and density equal to their corresponding averaged values and next for instantaneous values of temperature and density. The comparison of the results showed that the relative difference between these two sets

of values was always less than 0.1 percent. Therefore, the temperature and density fluctuations are not considered to be a significant source of error.

CHAPTER VI
ANALYSIS OF EXPERIMENTAL DATA

6.1 Introduction

There were two objectives that directed the analysis of the experiments: firstly, the derivation of universal laws for the interfacial and bed friction coefficients, f_i and f_0, respectively, and, secondly, the derivation of similar laws for the velocity and density distribution, particularly in the neighborhood of the interfacial zone.

The main flow and salinity parameters ranged within the following limits: (a) as stated in the previous chapter, the relative density difference ratio $\Delta\rho/(\rho + \Delta\rho)$ ranged between 8 $^{o}/_{oo}$ and 93 $^{o}/_{oo}$, (b) the mean velocity, V_0, upstream of the toe of the wedge varied from 1.86 cm/sec to 10.01 cm/sec and the velocity of the upper fresh water layer, V_1, in the cross section of measurements ranged from 2.21 cm/sec to 10.91 cm/sec, (c) the depth of flow upstream of the toe of the wedge, h_0, ranged from 6.55 cm to 34.57 cm, and (d) the Reynolds number, upstream of the toe of the wedge, based on the equivalent pipe diameter, ranged from 6,700 to 62,000.

The cross section of velocity and density measurements was located at about 4.5 meters from the downstream end of the channel.

6.2 Density Distribution Law

In each position of the conductivity probe, more than two hundred instantaneous data of density were taken. These data were

averaged to obtain the mean value of density at this position. The variation of density with the depth was significant in the vicinity of the interface, becoming negligible at some distance away from it, of the order of a few millimeters. For this reason, most of the measurements were restricted to the immediate neighborhood of the interface. Knowing the position and the corresponding density, the density profiles have been drawn for each experiment. Figures A.1 to A.5 of the Appendix give examples of density profiles for some experiments belonging to the one particular group. Figure 6.1 gives the parameters of a density interfacial zone. The width δ of that zone is defined as the vertical distance between the intersection points of the vertical lines at $\Delta\rho_{\ell}/(\rho + \Delta\rho) = 0$ and $\Delta\rho_{\ell}/(\rho + \Delta\rho) = \Delta\rho/(\rho + \Delta\rho)$ and the tangent to the curve at $\Delta\rho/2(\rho + \Delta\rho)$, where the subscript ℓ indicates mean local conditions with respect to time. The assumption of small entrainment means that the mixing takes place within the interfacial zone whose width is very small compared to the depths of the two layers. Outside the interfacial zone the layers are considered homogeneous. The mean value of $\delta/2$ has been found to be 3 mm with a divergence of ± 1 mm. Therefore, after comparing the values of $\delta/2$ to the depths of the layers we can consider that the previous assumption is valid (Table 2).

The theoretical interface is defined as the locus of points at which the density is $\rho + \Delta\rho/2(\rho + \Delta\rho)$. The distance between the interface and the bottom, h_s, is defined as the depth of the lower layer and the distance between the interface and the free surface, h_1, is defined as the depth of the upper layer.

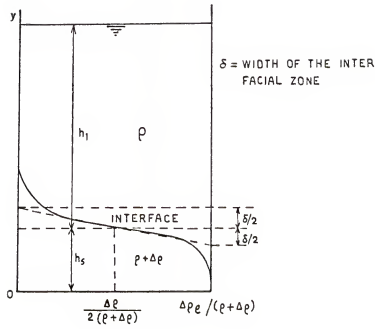

Figure 6.1 Definition sketch for the interfacial zone

The density distribution curve is approximately linear in its central portion and it curves at its two ends near the boundaries. Powell [34] gave the following density distribution law.

$$\frac{\rho_{\ell} - \rho}{\Delta\rho} = \frac{1}{2}\left[1 - \tanh\left[\frac{y - h_s}{\delta/2}\right]\right] \qquad (6.2.1)$$

The symbols of Equation (6.2.1) have been defined in Figure 6.1.

Figure 6.2 gives Powell's [34] experimental data and Figure 6.3 represents some experiments of the present study, belonging to group 5, with $\Delta\rho/(\rho + \Delta\rho) = 0.0225$ approximately equal to the value used by Powell [34] (Table 1 and Appendix). In both figures the curves given by Equation (6.2.1) have been drawn and they appear to agree satisfactorily with the experimental data for $0.1 \leqq \Delta\rho_{\ell}/(\rho + \Delta\rho) \leqq 0.9$.

When the velocity, V_1, of the upper layer was less than the critical entrainment velocity, V_c, given by Keulegan [22, 24], the interface was smooth (Figure 5.10). For V_1 larger than V_c, random interfacial wavelets were formed moving downstream with a slowly increasing wavelength and amplitude. In many cases the wavelength was of the order of some centimeters and the amplitude of some millimeters. For larger velocities V_1, the wave crests become sharper and, after breaking, the two fluids were mixed at the interface [Figure 5.12(a)]. The latter in all the experiments was distinct and easily identifiable.

6.3 Velocity Distribution

The time-averaged horizontal velocity component, u, was evaluated from the instantaneous velocities computed from the hot film

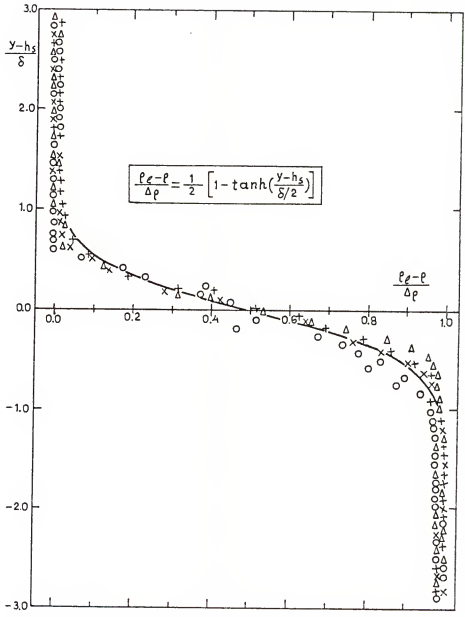

Figure 6.2 Nondimensional density distribution, Powell's data

Source: [34, Figure 18]

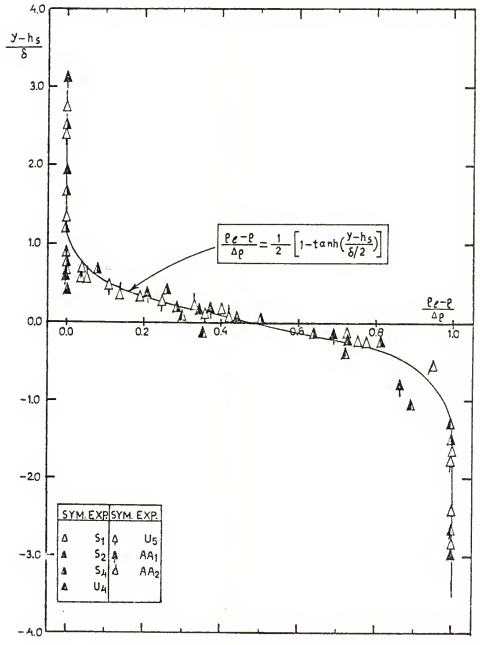

Figure 6.3 Nondimensional density distribution (data from present study)

Table 1. Grouping of experiments

Group	Experiments	$\left(\frac{\Delta\rho}{\rho + \Delta\rho}\right)$ °/oo
1	$P_{10}, P_9, P_7, P_6, P_5, O_6, P_4, N_4, P_2$	8.8
2	$I_2, I_3, I_4, N_1, N_3, O_3, O_5, P_1$	10.4
3	$I_1, O_1, O_2, Q_1, Q_3, Q_4, Q_5, Q_6, T_4, CA_3$	12.0
4	L_2, L_6, L_7, L_9, V_4	17.8
5	$R, S_5, T_1, V_1, V_5, V_6, S_1, S_2, S_4, U_4, U_5, AA_1, AA_2$	22.5
6	$U_1, U_2, U_3, V_2, W_4, W_5, W_6, Y_1, Y_2, Y_4, Y_5, Z_1,$ Z_2, Z_3, Y_3	35.5
7	W_1, W_2, W_3	48.5
8	$DA_1, DA_2, DA_3, DA_4, DA_5, EA_1, EA_2, EA_3, EA_4,$ GA_1, GA_2	82.0

anemometer recordings. Knowing the velocity and the corresponding position, the dimensional velocity distribution was determined for each experiment. Examples are given in Figures A.1 to A.5 of the Appendix. Figure 6.4 is a definition sketch with the following parameters:

a. The position of the density interface, as defined in section 6.2 from the density profiles

b. The position of the velocity interface—This interface is defined at the point where u = U/2 where U is the free surface velocity. This point approximately coincides with the inflection point at the interfacial zone of the velocity distribution curve (see section 2.3).

c. The distance, δu, between the velocity interface and the upper limit of the zone of shear flow—This limit is considered to be in a position where the velocity is 98 percent of U. Above this limit, the flow is considered frictionless (Figures A.1, A.2, A.4, and A.5 of the Appendix). This limit corresponds to the limit of the boundary layer for homogeneous fluids.

d. The distance, δu_1, between the velocity interface and the lower inflection point of the velocity distribution curve—A short distance below that point the velocity becomes negative (see Figure 2.16 and Figures A.1 to A.5 of the Appendix).

e. The distance, δu_2, given as $\delta u_2 = \delta u + \delta u_1$

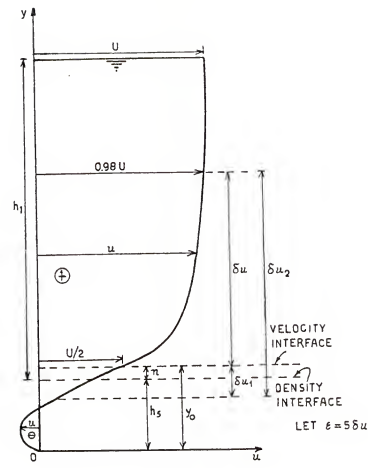

Figure 6.4 Definition sketch for velocity profiles

f. The distance, η, between the two interfaces

g. The parameter, $\varepsilon = 5\delta u_1$, defined for a better representation of the experimental data

h. The distance, y_0, between the bottom and the velocity interface, defined as

$$y_0 = h_s + \eta \tag{6.3.1}$$

For a dimensionless presentation, the velocity has been non-dimensionalized by U and the vertical distance by δu. The latter has been taken with reference to the velocity interface, i.e., data have plotted versus $(y - y_0)/\delta u$. After some trials, the dimensionless velocity distributions have been separated into two distinct groups. The first group contains the experiments of Figure 6.5 and the second the experiments of Figures 6.6 and 6.7. The separation of the second group into two subgroups was based on the ratio $\Delta\rho/(\rho + \Delta\rho)$. Figure 6.6 contains the experiments with $\Delta\rho/(\rho + \Delta\rho) \leqq 20\ ^{o}/oo$ and Figure 6.7 the experiments with $\Delta\rho/(\rho + \Delta\rho) > 20\ ^{o}/oo$. The curve in Figure 6.5 differs from the corresponding curves of Figures 6.6 and 6.7; Figure 6.5 contains mainly experiments with small velocities, V_0, upstream of the wedge. The dimensionless velocity distribution of Figures 6.6 and 6.7 is similar to the one given by Powell [34] (Figure 2.15). Powell [34] found out that δu has no significant correlation with the mean velocity of the upper layer and the downstream distance or with the Reynolds number based on these two quantities. Therefore, the flow is

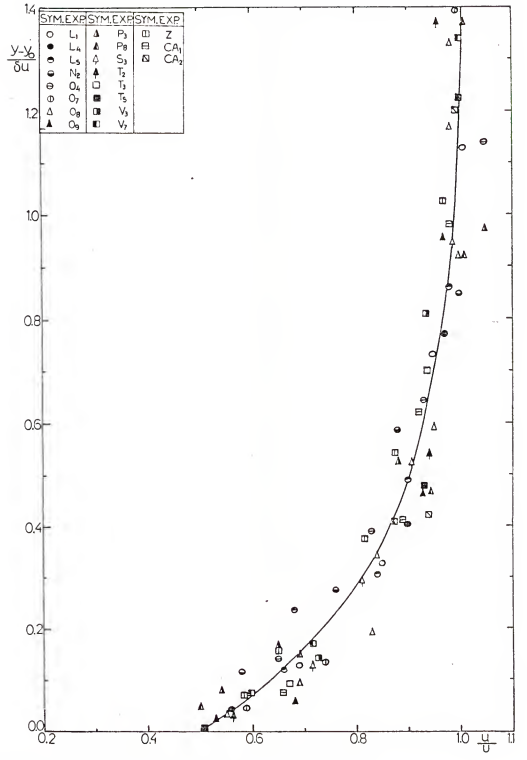

Figure 6.5 Dimensionless velocity distribution

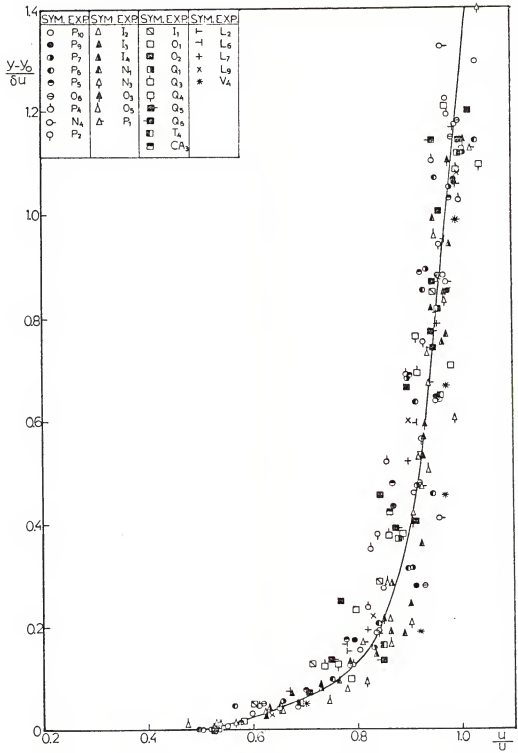

Figure 6.6 Dimensionless velocity distribution [$\Delta\rho/(\rho + \Delta\rho) \leqq 20\ ^{o}/_{oo}$]

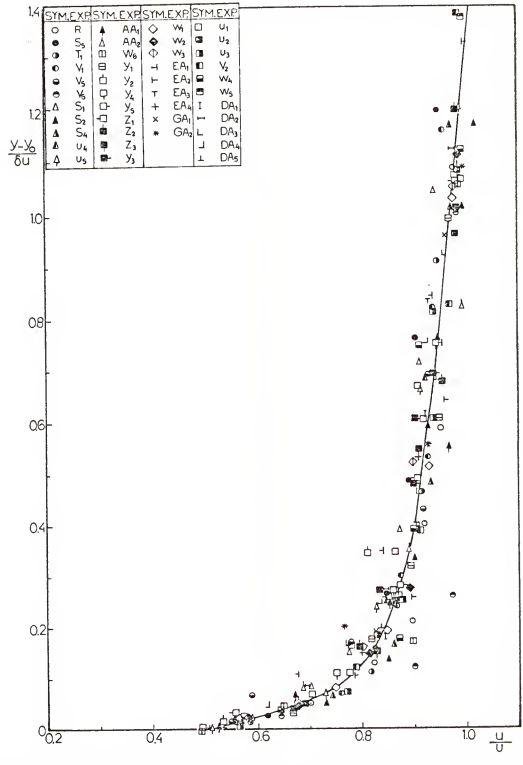

Figure 6.7 Dimensionless velocity distribution [$\Delta\rho/(\rho + \Delta\rho) > 20\ ^{o}/_{oo}$]

believed to be fully developed. This is not valid for the experiments of Figure 6.5. In the previous figures the mean curves were drawn and transferred onto a semilogarithmic paper. Figure 6.5 corresponds to Figure 6.8 and Figures 6.6 and 6.7 correspond to Figure 6.9. The mean curves of Figures 6.6 and 6.7 coincide. The comparison of Figures 6.8 and 6.9 suggests that in fully developed flow, the dimensionless velocity distribution is logarithmic and it consists of two branches intersecting each other at approximately the point where $(y - y_0)/\delta u = 0.15$. This value is very near the limit of validity of the wall law for a solid boundary for homogeneous fluids. This significant observation will be discussed later.

The subsequent analysis has been applied to the experiments of the second group, where the flow is considered fully developed (experiments of Figures 6.6 and 6.7).

Within the region of shear flow there are three distinct zones of the dimensional velocity distribution curves: (a) the zone δu, (b) the zone δu_1, and (c) the zone in the immediate neighborhood of the velocity interface (Figure 6.4). To study the flow structure, the vertical distances were represented in each zone by the nondimensional relations $(y - y_0)/\delta u_1$, $(y - y_0)/\varepsilon = (y - y_0)/5\delta u_1$, and $(y - y_0)/\delta u_2$, respectively. The velocities were nondimensionalized by the free surface velocity, U.

By correlating the dimensionless lengths to dimensionless velocities a mathematical expression for the velocity distribution was sought by which viscous stresses could be reliably computed at any point

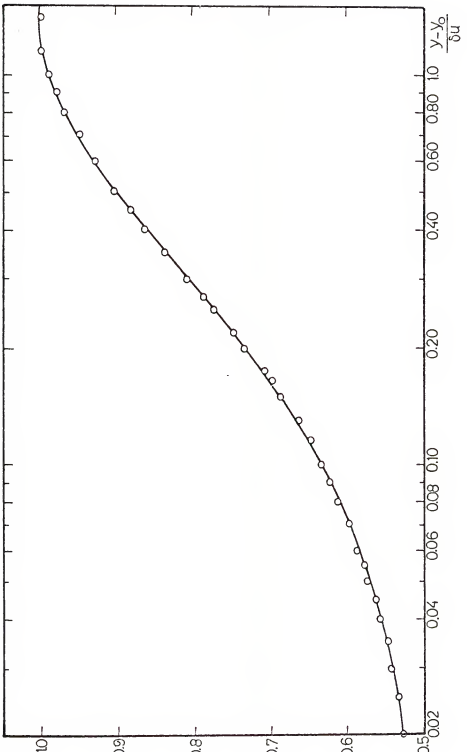

Figure 6.8 Dimensionless velocity distribution (data from Figure 6.5)

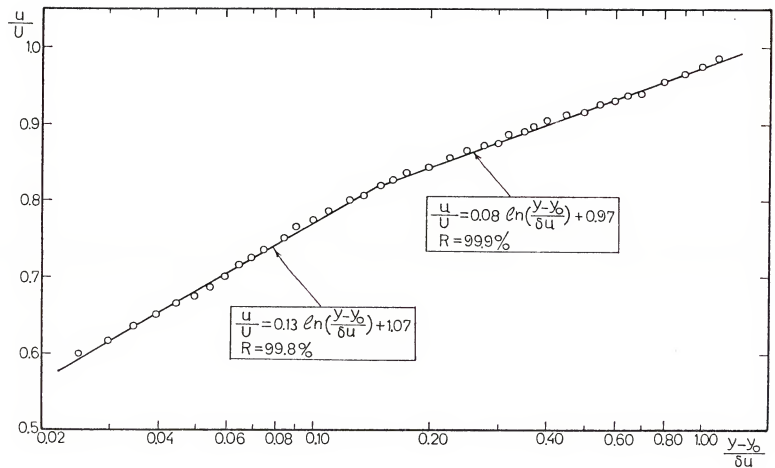

Figure 6.9 Dimensionless velocity distribution (data from Figures 6.6 and 6.7)

of the cross section. The general laws of velocity distribution were derived in paragraph 6.5 in terms of the friction velocity, u_*.

First, the velocity distribution in the immediate neighborhood of the velocity interface was studied. The plots in Figures 6.10 and 6.11 clearly suggest that this distribution is linear; the correlation coefficient, R, is equal to 98 percent for the data of Figure 6.10 and 98.6 percent for the data of Figure 6.11. The linear distribution zone has a width between 2 mm and 6 mm with an average of 4 mm. The linear velocity distribution can be satisfactorily approximated by the equation

$$\frac{u}{U} = 5\left[\frac{y - y_0}{\delta u_2}\right] + 0.5 \qquad (6.3.2)$$

where the symbols are given in Figure 6.4.

Next, the velocity distribution in the zones of width δu and δu_1 have been simultaneously studied. A wide scattering of data points was first observed in each one of the two original groups for $\Delta\rho/(\rho + \Delta\rho) \leqq 20\ ^{o}/oo$ and $\Delta\rho/(\rho + \Delta\rho) > 20\ ^{o}/oo$, respectively.

This scattering is indicative of some dependence of dimensionless velocities on $\Delta\rho/(\rho + \Delta\rho)$ in the aforementioned zones, in spite of the fact that in the zone of linear velocity distribution the dimensionless velocity profile appears to be practically independent of $\Delta\rho/(\rho + \Delta\rho)$. To further elucidate that dependence, it has been decided to separate the experiments into eight groups according to $\Delta\rho/(\rho + \Delta\rho)$.

Table 1 shows the grouping of experiments with each group identified by its mean value of $\Delta\rho/(\rho + \Delta\rho)$.

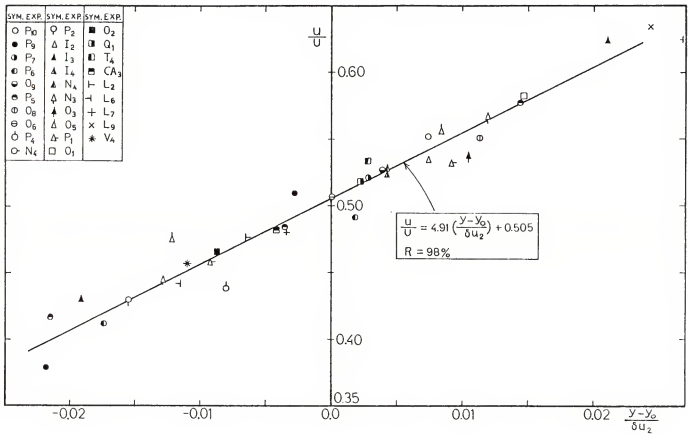

Figure 6.10 Dimensionless velocity distribution in the immediate neighborhood of velocity interface for $\Delta\rho/(\rho + \Delta\rho) \leq 20$ ‰

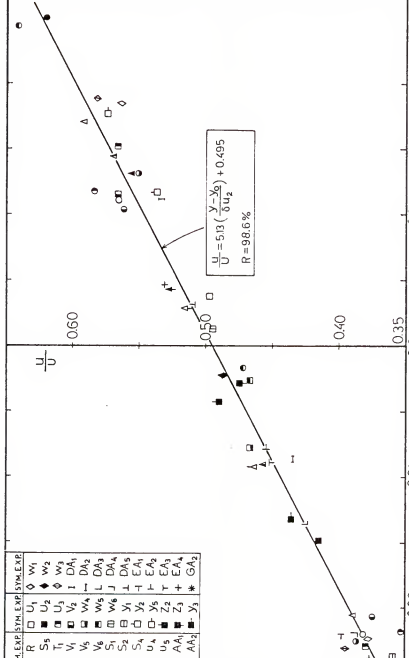

Figure 6.11 Dimensionless velocity distribution in the immediate neighborhood of velocity interface, for $\Delta\rho/(\rho + \Delta\rho) > 20$ o/oo

The graphs of Figures 6.12 to 6.19 give the dimensionless velocity distribution outside of the linear zone for the eight groups of experiments (Table 1). These graphs suggest a logarithmic velocity distribution in the zones δu and δu_1 with values of the correlation coefficient R ranging from 61 percent to 98.1 percent. In the zone δu the semilogarithmic plot consists of two linear segments which intersect approximately at the point $(y - y_0)/\delta u = 0.15$. It is noteworthy that in boundary layers with a width δ, and with fixed boundaries, the point for which $y/\delta = 0.15$ is the limit of validity of the wall law. We can define tentatively, therefore, the value of $(y - y_0)/\delta u = 0.15$ as the limit of validity of the "law of the interface" which corresponds to the wall law for solid boundaries. In the zone δu_1 preliminary analysis also leads to a similar logarithmic law. These previous laws were subsequently used for the calculation of viscous stresses.

6.4 Laws of Variation of Interfacial and Bed Friction Coefficients

The local friction coefficients f_i and f_0 at the interface and at the bed, respectively, are defined by the relations

$$f_i = \frac{8\tau_i}{\rho V_1^2} \quad \text{and} \quad f_0 = \frac{8\tau_0}{\rho V_1^2} \tag{6.4.1}$$

where τ_i and τ_0 are the local shear stresses at the interface and at the bottom, respectively. The shear stresses in a turbulent flow are given by the equation

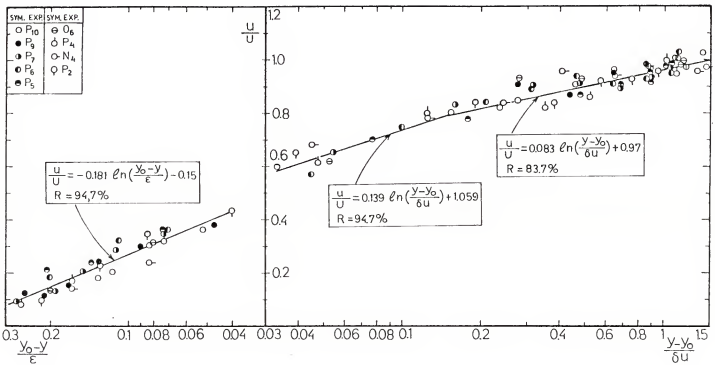

Figure 6.12 Dimensionless velocity distribution outside of the linear zone (group 1)

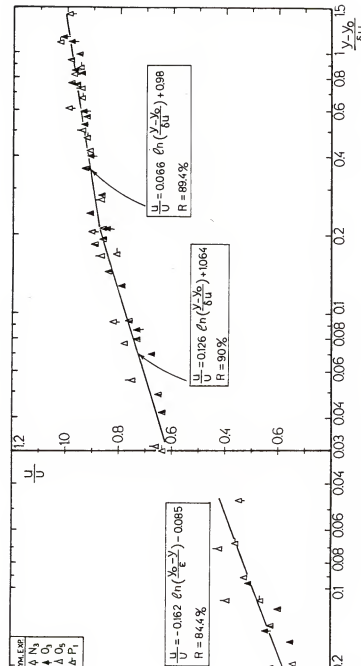

Figure 6.13 Dimensionless velocity distribution outside of the linear zone (group 2)

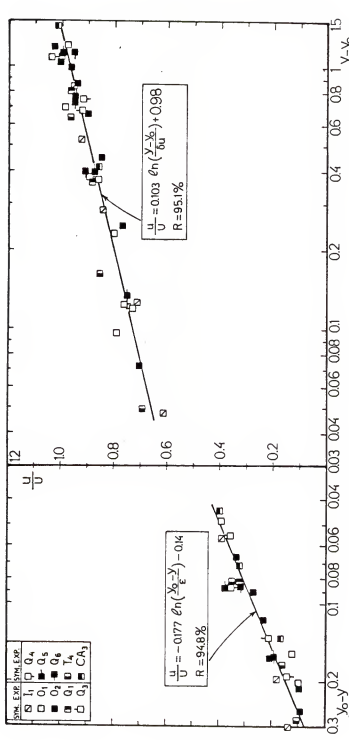

Figure 6.14 Dimensionless velocity distribution outside of the linear zone (group 3)

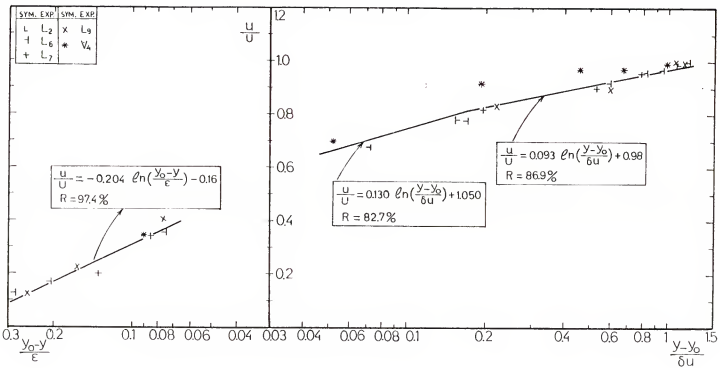

Figure 6.15 Dimensionless velocity distribution outside of the linear zone (group 4)

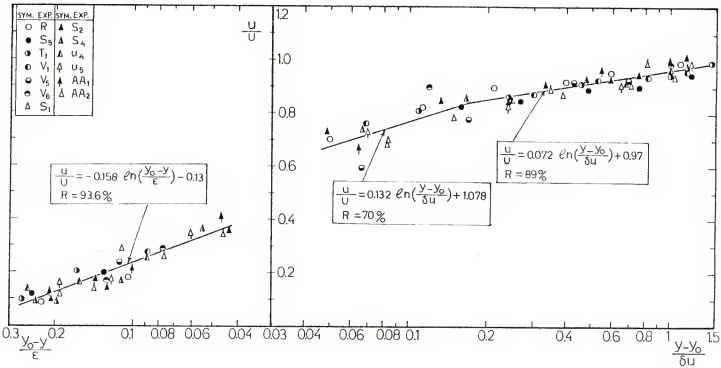

Figure 6.16 Dimensionless velocity distribution outside of the linear zone (group 5)

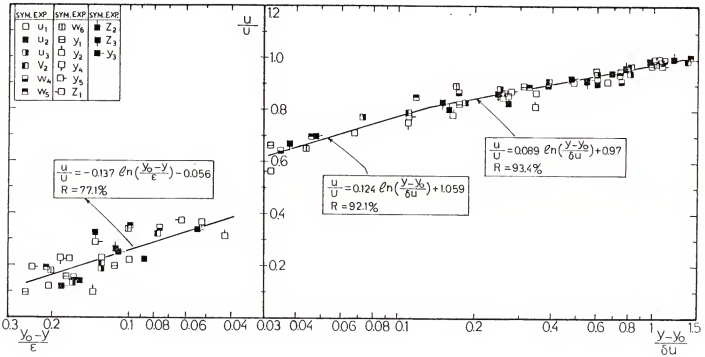

Figure 6.17 Dimensionless velocity distribution outside of the linear zone (group 6)

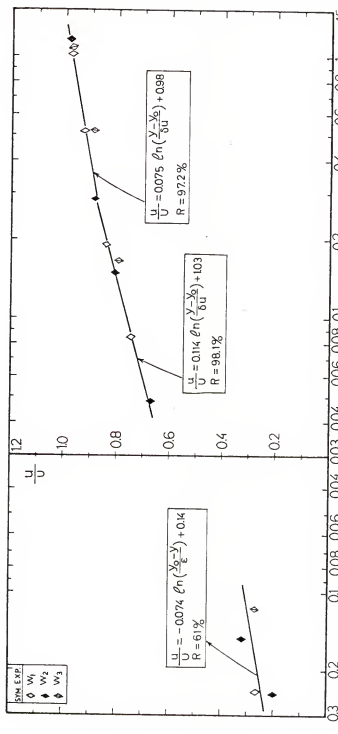

Figure 6.18 Dimensionless velocity distribution outside of the linear zone (group 7)

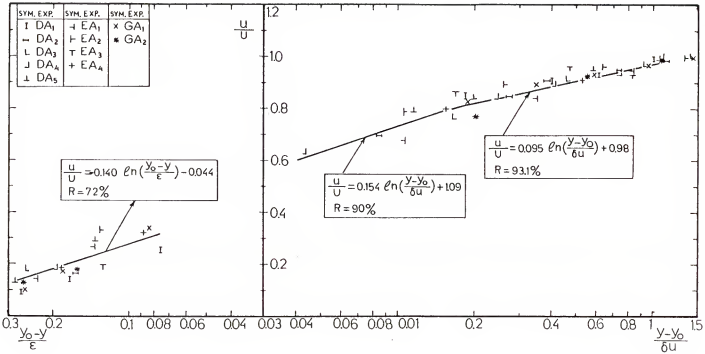

Figure 6.19 Dimensionless velocity distribution outside of the linear zone (group 8)

$$\tau = \tau_v + \tau_t = \mu \frac{\partial u}{\partial y} - \overline{\rho u' v'} \qquad (6.4.2)$$

where τ_v are the viscous stresses and τ_t are the Reynolds stresses. The viscous stresses were obtained from the velocity distribution curve while the Reynolds stresses are given by the correlation of the turbulent velocity fluctuations u' and v'.

For the evaluation of viscous stresses, the mean curves of each group of experiments in Figures 6.12 to 6.19 were used. However, a more careful study of the graphs, particularly in the region $0 < (y - y_0)/\delta u \leq 0.15$, led to the observation that the slope of the straight line differs from experiment to experiment as well as from the mean straight line of the experimental group. Therefore, the straight line of each particular experimental velocity distribution was used for the computation of the viscous stress instead of the average line. These curves are presented in Figures A.6 to A.12 of the Appendix, as an example for a part of the experiments of group 5 (Table 1). The velocity distribution law in zone δu_1, in general, is expressed by two straight lines intersected at point $(y - y_0)/\varepsilon = 0.1$. That point has been defined as the limit of the law of the interface for zone δu_1.

The general form of the laws of the interface are

$$\frac{u}{U} = a_3 \ln \left(\frac{y - y_0}{\delta u} \right) + b_3 \qquad (6.4.3)$$

for the δu zone and

$$\frac{u}{U} = a_2 \ln \left(\frac{y_0 - y}{\varepsilon} \right) + b_2 \qquad (6.4.4)$$

for the δu_1 zone, where a_2, a_3, b_2, b_3 are functions of the flow and salinity parameters and ε is taken equal to $5\delta u_1$. In the immediate neighborhood of the velocity interface the linear law [Equation (6.3.2)] has been used.

Figure 6.20 constitutes a definition sketch for the velocity distribution on a semilogarithmic paper.

In the zone δu_1, points 1 and 2 define the limits of the region of the law of the interface. In the same way, points 3 and 4 define similar limits in the zone δu. Between points 2 and 3 the linear law is valid. The viscous stresses at any position y of the cross section can be expressed by the following relationships:

$$\tau_v = \mu \frac{a_3 U}{(y - y_0)} \tag{6.4.5}$$

for the δu zone

$$\tau_v = \mu \frac{a_2 U}{(y_0 - y)} \tag{6.4.6}$$

for the δu_1 zone and

$$\tau_v = \mu \frac{a_1 U}{\delta u_2} \tag{6.4.7}$$

in the immediate neighborhood of the velocity interface, where a_1 is the slope of straight lines in Figures 6.10 and 6.11 [in Equation (6.3.2) $a_1 = 5$]. From Equations (6.4.5) to (6.4.7) and from Figure 6.20,

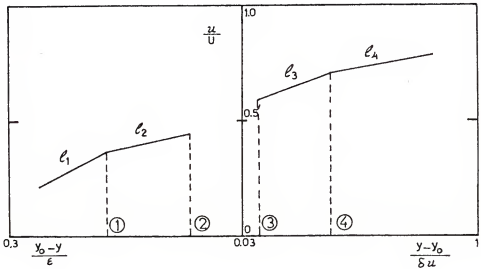

Figure 6.20 Definition sketch for the velocity distribution laws

it follows that the above stresses reach their maximum value at one of the positions 0, 1, 2, 3, or 4. In particular, at position 4 the viscous stresses are lower than at any other position of line l_3 [Equation (6.4.5)], because the slope of l_4 is less than the slope of l_3. Moreover, the value of $y - y_0$ in l_4 is larger than the corresponding value of $y - y_0$ at any point of l_3.

For the experiments of groups 1, 2, 3, and 4 with $\Delta\rho/(\rho + \Delta\rho) \leq 20\ ^{o}/oo$, the corresponding positions of points 0, 1, 2, and 3 (Figure 6.20) are $(y_0 - y)/\varepsilon = 0.0$, $(y_0 - y)/\varepsilon = 0.12$ [and in some experiments $(y_0 - y)/\varepsilon = 0.077$], $(y_0 - y)/\varepsilon = 0.047$ and $(y - y_0)\delta u = 0.037$, respectively. For the experiments of groups 5, 6, 7, and 8 with $\Delta\rho/(\rho + \Delta\rho) > 20\ ^{o}/oo$ the corresponding positions of points 0, 1, 2, and 3 are $(y_0 - y)/\varepsilon = 0.0$, $(y_0 - y)/\varepsilon = 0.12$ [and in some experiments $(y_0 - y)/\varepsilon = 0.08$], $(y_0 - y)/\varepsilon = 0.048$ [and in some experiments $(y_0 - y)/\varepsilon = 0.028$], and $(y - y_0)/\delta u = 0.023$ [and in some experiments $(y - y_0)/\delta u = 0.04$]. In some of the points 0, 1, 2, 3 correspond two positions. For example, at point 1 of the groups with $\Delta\rho/(\rho + \Delta\rho) \leq 20\ ^{o}/oo$, correspond the positions $(y_0 - y)/\varepsilon = 0.12$ and 0.077; that means that in some experiments point 1 corresponds to $(y_0 - y)/\varepsilon = 0.12$ and in the remaining experiments point 1 corresponds to $(y_0 - y)/\varepsilon = 0.077$. The maximum Reynolds stresses, τ_{it}, have been defined in the immediate vicinity of points 0, 1, 2, and 3. Next, the total stresses $\tau_{i0} = (\tau_{i\nu})_0 + (\tau_{it})_0$ at point 0 have been calculated. Here $(\tau_{i\nu})_0$ are the viscous and $(\tau_{it})_0$ are the Reynolds stresses at $(y_0 - y)/\varepsilon = 0.0$. Next, the Reynolds stresses τ_{it} and the viscous stresses $\tau_{i\nu}$ at points 0, 1, 2, and 3 have been nondimensionalised by τ_{i0}. The results are

given in Figures 6.21 and 6.22. In these figures the left vertical axis represents the relative distance of the position from the velocity interface with respect to δu or with respect to $\varepsilon = 5\delta u_1$. The right vertical axis represents the absolute value of the above distances in millimeters and the horizontal axis represents the relative Reynolds stresses τ_{it} or viscous stresses $\tau_{i\nu}$ with respect to the total stresses τ_i at $(y_0 - y)/\varepsilon = 0.0$ (that is, τ_{i0}). From Figures 6.21 and 6.22 and from the governing equations of the velocity distribution, the total stress $\tau_i = \tau_{i\nu} + \tau_{it}$ for each experiment has been calculated at points 0, 1, 2, and 3; the highest of these values was taken as the local interfacial stress τ_i. The local interfacial coefficient f_i was calculated from the relationship

$$f_i = \frac{8(\tau_{i\nu} + \tau_{it})_{max}}{\rho V_1^2} \tag{6.4.8}$$

where $(\tau_{i\nu} + \tau_{it})_{max}$ is the maximum value of the total shear stress in the cross section of measurements, except in the vicinity of the bottom.

Next, on the basis of the theoretical analysis developed in section 3.4, the mean interfacial friction coefficient over the length of salt water intrusion has been calculated by means of Equation (3.4.16). The mean value of the depth h_s has been numerically calculated and that of h_1 has been calculated from the relation $\bar{h}_1 = \bar{h}_0 - \bar{h}_s$. The depth of the lower layer at the mouth of the channel, h_{s0}, is the mean value of the depths in three successive cross sections in a distance between them of about 2 m.

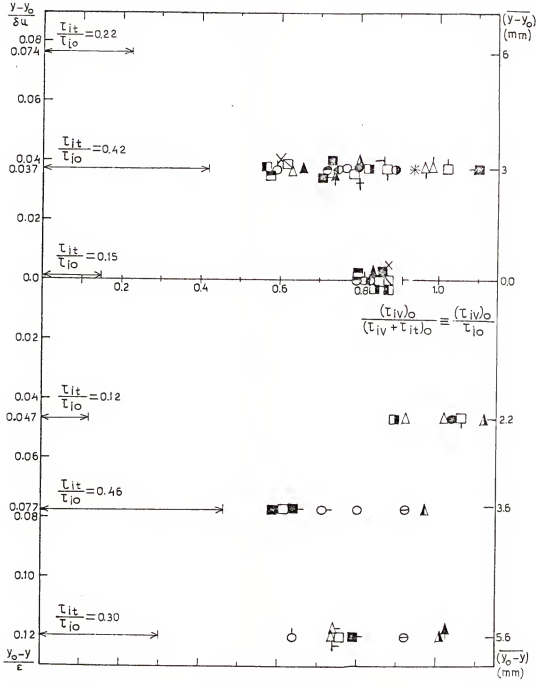

Figure 6.21 Dimensionless values of Reynolds and viscous stresses for $\Delta\rho/(\rho+\Delta\rho) \leq 20\ ^{o}/_{oo}$

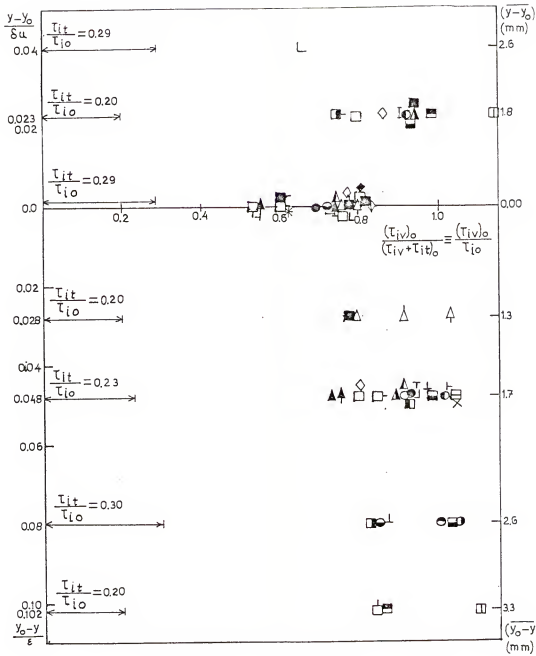

Figure 6.22 Dimensionless values of Reynolds and viscous stresses for $\Delta\rho/(\rho + \Delta\rho) > 20$ o/oo

Table 2 gives the values of the parameters entering in Equation (3.4.16) as well as the dimensionless values of δu and δu_1. In column 26, the values of f_i based on Equation (6.4.8) are listed, while those values estimated from Equation (3.4.16) are listed in column 27.

A comparison of f_i suggests that these two values of f_i based on direct measurements and on the integration of the equations of motion, respectively, are very close to each other; therefore, f_i can be reasonably approximated from Equation (3.4.16).

The values of f_i calculated on the basis of Schijf and Schönfeld's model [37] [Equation (3.2.17)] are listed in column 29. Since for the reasons explained in Chapter IV, the length of salt water intrusion, L_0, in the channel was smaller than the full length, L, of the arrested saline wedge (Figure 3.4), the calculation of L had to be first computed in the following way.

For each experiment of given densimetric Froude number, Fr_0', the critical depth of the fresh water layer, h_{1c}, was computed from Equation (3.2.15). The critical salt water depth $h_{sc} = h_0 - h_{1c}$ has next been used to nondimensionalize the wedge profile, as h_s/h_{sc}. From Equation (3.3.14) or from the graph of Figure 3.2, the total intrusion length, L, was estimated for several values of h_s/h_{sc} and distances x_i from the channel entrance. The mean value of L, thus determined, with the exception of certain data that appeared to be in gross error, was taken to represent the true total intrusion length, L, of the wedge.

The number of the rejected values was small in comparison to their total number. Finally, f_i has been estimated by Schif and

Table 2. Values of parameters introduced in Equation (3.4.16)

No.	Exp.	Sym.	$\frac{\Delta\rho}{\rho+\Delta\rho}$	h_0	h_1	η	V_1	h_{s1}	λ	h_1	h_{10}	V_1	L_0	L	a	β
			o/oo	cm	cm	cm	$\frac{cm}{sec}$	cm		cm	cm	$\frac{cm}{sec}$	m	m		
1	2	3	4	5	6	7	8	9	10	11	12	13	14	15	16	17
1	P_{10}	○	7,9	14,01	11,76	0,77	2,21	1,60	1,41	12,35	11,34	2,11	14,16	42,6	1,033	0,325
2	P_9	●	8,2	14,06	11,81	0,86	2,47	1,60	1,41	12,26	11,33	2,73	14,02	37,5	1,041	0,266
3	P_7	◑	8,7	14,17	11,74	0,81	3,01	1,73	1,41	12,08	11,07	2,92	14,66	32,4	1,052	0,218
4	P_6	◐	9,0	14,22	11,56	0,65	3,35	1,91	1,39	11,96	10,95	3,23	15,27	29,3	1,067	0,193
5	P_5	◒	9,3	14,28	11,51	0,75	3,61	1,97	1,41	11,94	10,75	3,48	15,46	27,6	1,065	0,242
6	O_6	⊖	9,4	11,84	9,62	0,45	2,76	1,57	1,41	10,00	9,09	2,65	12,21	23,0	1,030	0,240
7	P_4	◔	9,7	14,34	11,46	0,76	3,76	2,08	1,39	11,75	10,47	3,66	17,04	27,6	1,047	0,190
8	N_4	◔	9,5	16,85	14,35	0,26	2,97	1,80	1,39	14,93	13,82	2,88	15,63	52,3	1,014	0,260
9	P_2	◌	9,8	14,33	12,43	0,56	3,61	1,35	1,41	12,65	11,86	3,55	9,19	23,6	1,017	0,173
10	I_2	△	10,8	10,82	9,25	0,55	3,49	1,12	1,40	9,15	8,44	3,52	8,46	16,0	1,056	0,350
11	I_3	▲	10,6	14,13	11,48	0,87	3,82	1,90	1,40	11,93	10,61	3,67	15,82	27,7	1,050	0,333
12	I_4	△	10,5	14,39	12,34	0,02	3,88	1,40	1,46	12,62	11,27	8,80	11,19	22,5	1,015	0,176
13	N_1	◭	10,3	17,05	14,15	0,35	3,48	2,05	1,42	14,94	13,62	3,30	18,10	52,2	1,020	0,219
14	N_3	△	10,1	16,94	14,44	0,51	3,11	1,80	1,39	15,10	13,84	2,97	15,66	49,7	1,017	0,246
15	O_3	▲	10,7	11,97	9,70	0,44	3,19	1,62	1,40	10,09	9,30	3,06	10,83	20,7	1,036	0,181
16	O_5	△	10,0	11,91	9,53	0,46	2,97	1,68	1,42	9,92	8,83	2,86	13,95	24,2	1,023	0,198
17	P_1	△	10,0	14,36	12,11	0,40	4,29	1,60	1,41	12,36	11,34	4,24	11,10	21,5	1,026	0,165
18	I_1	⊠	12,0	10,60	8,20	0,44	3,68	1,70	1,41	8,84	7,75	3,42	12,90	19,1	1,013	0,261
19	O_1	□	11,1	12,12	10,36	0,33	3,67	1,26	1,40	10,06	9,44	3,76	8,50	14,9	1,021	0,139
20	O_2	■	11,1	12,01	9,52	0,46	3,58	1,79	1,39	9,79	8,98	3,48	12,62	19,1	1,041	0,184
21	Q_1	◨	12,5	11,93	9,16	0,16	4,31	1,97	1,41	9,77	8,73	4,04	18,92	15,8	1,018	0,192
22	Q_3	◫	12,6	11,81	9,21	0,35	3,70	1,85	1,41	9,58	8,79	3,14	12,80	22,6	1,032	0,213
23	Q_4	◪	11,6	11,76	9,66	0,80	3,41	1,50	1,40	10,18	9,19	3,23	11,47	23,3	1,055	0,323
24	Q_5	■	11,3	11,74	9,48	0,57	3,30	1,61	1,40	10,13	9,14	3,12	11,86	24,8	1,036	0,201
25	Q_6	■	11,3	11,65	9,05	0,18	2,99	1,85	1,41	9,58	8,72	2,83	12,97	24,5	1,006	0,222
26	T_4	◧	12,1	33,73	30,75	0,29	4,37	2,12	1,41	31,52	30,36	4,26	17,85	158,3	1,007	0,164
27	CA_3	▬	12,8	29,50	26,43	0,79	6,54	2,07	1,46	26,34	24,97	6,56	12,44	36,2	1,020	0,221
28	L_2	⊢	16,6	6,54	5,24	0,33	3,96	0,95	1,37	5,26	4,71	3,94	7,62	9,2	1,056	0,250
29	L_6	⊣	17,3	11,22	8,94	0,31	4,57	1,63	1,40	9,28	8,35	4,40	12,91	19,8	1,022	0,190
30	L_7	+	16,8	11,32	9,37	0,44	4,41	1,40	1,39	9,49	8,62	4,35	9,72	15,7	1,036	0,213
31	L_9	×	16,8	11,39	9,12	0,32	4,54	1,57	1,45	9,46	8,22	4,42	11,26	16,2	1,045	0,198
32	V_4	⊼	18,9	29,64	27,81	0,40	3,68	1,28	1,43	28,23	27,62	3,62	11,15	245,7	1,011	0,203
33	R	○	20,9	11,66	9,45	0,37	4,26	1,60	1,41	10,61	9,54	4,04	10,63	27,4	1,021	0,237
34	S_5	●	20,9	19,01	16,53	0,39	3,76	1,78	1,39	17,08	16,04	3,64	16,23	71,1	1,022	0,261
35	T_1	◑	20,7	29,76	27,14	0,31	4,86	1,82	1,44	27,91	26,81	4,69	16,78	167,6	1,011	0,119
36	V_1	◐	22,5	20,42	18,59	0,50	3,69	1,33	1,38	18,96	18,29	3,55	13,58	113,7	1,019	0,339
37	V_5	◒	19,8	34,57	32,45	0,12	4,17	1,52	1,40	32,49	31,70	4,16	15,34	203,8	1,007	0,123
38	V_6	◓	20,9	34,18	31,61	0,18	3,60	1,82	1,41	32,19	31,10	3,53	18,73	228,0	1,005	0,100

Table 2—Continued

ε	T	A	Fr_o	$\delta u/h_o$	$\frac{\delta u_1}{h_s}$	I_R	$ReFr^2$	f_i	f_i	f_i	f_i	λ_ε	$f_{\pm\varepsilon}$	f_o	No.
	°C														
18	19	20	21	22	23	24	25	26	27	28	29	30	31	32	33
0.249	27.90	0.218	0.179	0.587	0.765	3.909	12.2	0.0254	0.0239	0.0340	0.0334	1.40	0.0250	0.0100	1
0.221	27.95	0.221	0.195	0.682	0.539	3.721	16.0	0.0200	0.0201	0.0275	0.0310	1.40	0.0200	0.0080	2
0.233	27.80	0.229	0.226	0.675	0.488	3.402	25.4	0.0184	0.0155	0.0231	0.0251	1.40	0.0180	0.0072	3
0.343	27.80	0.238	0.243	0.653	0.473	3.248	31.6	0.0147	0.0135	0.0199	0.0231	1.40	0.0150	0.0060	4
0.318	27.70	0.236	0.255	0.692	0.513	3.148	37.4	0.0122	0.0129	0.0199	0.0216	1.40	0.0130	0.0052	5
0.333	27.05	0.281	0.214	0.634	0.543	3.519	18.8	0.0245	0.0213	0.0298	0.0312	1.40	0.0240	0.0096	6
0.239	27.60	0.238	0.257	0.621	0.409	3.132	40.7	0.0130	0.0134	0.0196	0.0212	1.40	0.0125	0.0050	7
0.301	27.90	0.189	0.203	0.519	0.516	3.634	28.6	0.0167	0.0172	0.0248	0.0241	1.40	0.0165	0.0060	8
0.277	27.50	0.225	0.267	0.742	0.542	3.053	45.0	0.0125	0.0133	0.0198	0.0224	1.40	0.0117	0.0047	9
0.317	26.70	0.277	0.278	0.673	0.455	2.970	37.1	0.0179	0.0137	0.0209	0.0219	1.40	0.0155	0.0062	10
0.246	26.80	0.230	0.256	0.616	0.568	3.140	44.3	0.0132	0.0132	0.0203	0.0211	1.40	0.0136	0.0055	11
0.501	27.10	0.219	0.259	0.744	0.322	3.116	46.4	0.0138	0.0160	0.0238	0.0226	1.40	0.0135	0.0054	12
0.360	26.80	0.187	0.220	0.654	0.379	3.460	39.5	0.0154	0.0143	0.0217	0.0200	1.40	0.0148	0.0059	13
0.294	26.90	0.188	0.205	0.519	0.658	3.612	31.9	0.0171	0.0178	0.0262	0.0249	1.40	0.0170	0.0068	14
0.245	26.80	0.263	0.230	0.659	0.578	3.365	27.3	0.0208	0.0176	0.0269	0.0316	1.40	0.0185	0.0075	15
0.439	27.05	0.270	0.220	0.747	0.462	3.460	22.2	0.0197	0.0195	0.0285	0.0301	1.40	0.0220	0.0088	16
0.349	27.30	0.225	0.308	0.693	0.446	2.765	64.3	0.0115	0.0101	0.0148	0.0163	1.40	0.0117	0.0047	17
0.353	26.60	0.301	0.255	0.591	0.409	3.148	33.4	0.0170	0.0152	0.0215	0.0232	1.40	0.0172	0.0069	18
0.303	26.10	0.267	0.272	0.610	0.364	3.015	42.7	0.0181	0.0163	0.0232	0.0285	1.40	0.0158	0.0063	19
0.322	26.50	0.277	0.248	0.608	0.369	3.206	34.5	0.0169	0.0149	0.0214	0.0282	1.40	0.0172	0.0069	20
0.469	25.20	0.270	0.274	0.660	0.352	3.000	49.8	0.0141	0.0168	0.0234	0.0259	1.40	0.0150	0.0060	21
0.423	27.10	0.272	0.211	0.669	0.552	3.550	28.0	0.0178	0.0218	0.0305	0.0355	1.40	0.0195	0.0078	22
0.245	27.25	0.271	0.242	0.667	0.475	3.257	34.2	0.0172	0.0163	0.0233	0.0242	1.40	0.0172	0.0069	23
0.301	27.30	0.264	0.236	0.670	0.484	3.310	30.8	0.0178	0.0168	0.0241	0.0243	1.40	0.0187	0.0075	24
0.469	27.25	0.277	0.205	0.637	0.454	3.612	21.8	0.0233	0.0232	0.0322	0.0348	1.40	0.0235	0.0094	25
0.389	27.35	0.098	0.199	0.185	0.407	3.677	111.5	0.0124	0.0106	0.0165	0.0168	1.41	0.0117	0.0047	26
0.283	27.10	0.116	0.304	0.198	0.475	2.791	267.5	0.0091	0.0103	0.0169	0.0180	1.48	0.0088	0.0041	27
0.459	24.80	0.490	0.307	0.676	0.461	2.765	26.4	0.0233	0.0192	0.0287	0.0289	1.40	0.0230	0.0092	28
0.368	25.80	0.287	0.264	0.629	0.402	3.076	68.7	0.0151	0.0129	0.0185	0.0215	1.40	0.0156	0.0062	29
0.447	26.00	0.280	0.267	0.670	0.678	3.052	69.1	0.0150	0.0170	0.0233	0.0266	1.40	0.0153	0.0061	30
0.452	26.50	0.271	0.268	0.462	0.477	3.045	70.8	0.0158	0.0172	0.0234	0.0235	1.40	0.0152	0.0061	31
0.320	27.35	0.101	0.147	0.318	0.496	4.346	85.3	0.0150	0.0156	0.0233	0.0192	1.40	0.0140	0.0056	32
0.309	27.15	0.265	0.238	0.685	0.923	3.293	78.3	0.0184	0.0156	0.0220	0.0213	1.40	0.0174	0.0070	33
0.314	27.50	0.163	0.166	0.481	0.446	4.076	68.8	0.0173	0.0231	0.0328	0.0324	1.40	0.0163	0.0073	34
0.363	27.30	0.109	0.179	0.378	0.368	3.909	159.9	0.0143	0.0126	0.0194	0.0180	1.42	0.0136	0.0058	35
0.238	26.90	0.153	0.155	0.425	0.616	4.228	72.3	0.0182	0.0172	0.0244	0.0255	1.40	0.0180	0.0072	36
0.456	27.30	0.093	0.151	0.223	0.332	4.286	123.0	0.0164	0.0168	0.0250	0.0255	1.40	0.0146	0.0059	37
0.390	27.10	0.096	0.125	0.314	0.417	4.706	82.3	0.0188	0.0225	0.0343	0.0343	1.40	0.0170	0.0068	38

Table 2—Continued

1	2	3	4	5	6	7	8	9	10	11	12	13	14	15	16	17
39	S_1	Δ	24,0	9,82	7,25	0,09	5,20	1,82	1,41	7,96	7,25	4,74	11,76	18,5	1,033	0,167
40	S_2	▲	24,1	9,62	7,59	0,46	4,25	1,43	1,42	7,84	7,19	4,11	13,11	23,1	1,036	0,220
41	S_4	Δ	23,8	19,29	16,69	0,49	4,88	1,85	1,41	17,12	16,16	4,75	16,60	59,8	1,019	0,190
42	U_4	∠	25,1	10,13	7,78	0,14	3,78	1,70	1,38	8,42	7,41	3,49	16,70	29,3	1,017	0,228
43	U_5	Δ	23,5	9,95	7,93	0,42	3,08	1,42	1,42	8,43	7,60	2,89	15,30	33,7	1,027	0,246
44	AA_1	▲	23,9	30,49	27,32	0,28	7,96	2,02	1,57	27,20	26,26	7,99	13,37	53,5	1,005	0,170
45	AA_2	Δ	23,4	30,73	27,71	0,24	7,95	1,92	1,57	27,74	26,63	7,94	12,12	53,5	1,005	0,169
46	U_1	□	33,2	7,06	5,54	0,14	4,25	1,12	1,36	5,82	5,29	4,04	9,69	16,5	1,012	0,156
47	U_2	■	33,8	6,91	5,14	0,29	3,68	1,27	1,39	5,56	4,84	3,41	13,47	21,5	1,039	0,216
48	U_3	◨	30,7	10,19	8,47	0,32	4,10	1,27	1,35	8,83	8,21	3,94	11,27	30,4	1,024	0,210
49	V_2	◧	32,0	21,45	19,35	0,21	5,80	1,45	1,45	18,88	18,35	5,94	13,00	55,7	1,010	0,162
50	W_4	▭	40,2	10,43	8,47	0,30	4,08	1,41	1,39	8,83	8,21	3,91	16,26	39,1	1,020	0,201
51	W_5	▬	37,1	10,30	8,45	0,26	3,43	1,30	1,42	8,89	8,18	3,26	15,95	44,4	1,028	0,209
52	W_6	▥	30,7	10,11	8,26	0,33	2,86	1,30	1,42	8,81	8,79	2,69	16,82	48,6	1,021	0,330
53	Y_1	▤	32,5	20,31	17,76	0,52	7,25	1,70	1,50	18,16	17,18	7,09	13,71	47,1	1,020	0,224
54	Y_2	▯	34,0	21,12	18,57	0,02	8,50	1,65	1,55	18,57	16,74	8,35	15,13	37,2	1,017	0,179
55	Y_4	▢	45,7	30,90	27,90	0,48	7,17	1,95	1,54	28,08	26,90	7,12	19,08	107,6	1,016	0,196
56	Y_5	▢	31,9	30,24	27,49	0,14	6,25	1,82	1,51	27,68	26,87	6,21	17,19	118,3	1,008	0,147
57	Z_1	▭	32,8	6,83	5,29	0,28	5,18	1,09	1,41	5,43	4,65	5,04	9,26	10,6	1,030	0,204
58	Z_2	■	32,6	6,99	6,57	0,10	5,51	1,02	1,39	5,59	4,96	5,49	10,46	8,7	1,019	0,149
59	Z_3	■	35,5	9,84	7,62	0,11	5,17	1,57	1,41	7,90	7,04	4,98	14,98	22,5	1,022	0,166
60	Y_3	▬	34,4	31,85	28,30	0,65	8,97	1,90	1,58	28,89	27,32	8,79	16,93	80,6	1,012	0,229
61	W_1	◇	49,5	6,73	5,15	0,07	5,44	1,13	1,40	5,30	4,75	5,28	8,86	12,0	1,070	0,149
62	W_2	◆	49,0	6,68	5,83	0,00	5,00	1,30	1,42	5,22	4,65	4,63	10,96	15,6	1,014	0,196
63	W_3	◈	47,5	6,55	4,97	0,20	4,08	1,13	1,40	5,24	4,65	3,88	11,64	17,3	1,024	0,263
64	DA_1	⊥	93,0	7,24	5,44	0,25	6,11	1,25	1,44	6,06	5,17	5,48	16,29	29,7	1,029	0,184
65	DA_2	⊢	93,5	7,10	5,39	0,16	6,24	1,21	1,41	5,68	5,00	5,93	14,00	20,6	1,028	0,140
66	DA_3	L	90,0	7,26	5,43	0,06	6,49	1,28	1,45	5,98	5,26	5,89	13,71	23,6	1,016	0,114
67	DA_4	⊥	85,8	9,08	7,20	0,15	5,73	1,33	1,42	7,80	6,96	5,29	15,93	37,7	1,023	0,137
68	DA_5	⊥	82,4	9,01	6,94	0,20	6,24	1,42	1,46	7,64	6,78	5,67	15,86	33,2	1,021	0,169
69	EA_1	⊣	80,1	20,95	18,68	0,23	10,91	1,27	1,79	18,63	17,52	10,94	14,06	47,7	1,015	0,166
70	EA_2	⊢	78,3	20,42	18,62	0,35	9,30	1,05	1,71	18,79	18,09	9,22	10,84	64,9	1,015	0,211
71	EA_3	⊤	88,2	30,16	27,79	0,38	10,86	1,32	1,80	27,70	26,66	10,90	17,03	120,3	1,011	0,157
72	EA_4	+	82,3	29,14	27,02	0,26	7,73	1,32	1,61	27,33	26,61	7,65	16,90	220,8	1,013	0,133
73	GA_1	x	70,4	20,86	18,68	0,44	8,41	1,33	1,64	18,90	17,99	8,31	15,64	70,8	1,016	0,185
74	GA_2	*	72,6	21,55	18,93	0,24	8,47	1,62	1,62	19,69	18,49	8,14	15,40	80,4	1,015	0,164

$$A = \left\{ \frac{(b + 2h_1)^{0,25}}{h_1} \right\}$$

Table 2—Continued

.18	19	20	21	22	23	24	25	26	27	28	29	30	31	32	33
0.477	25.90	0.323	0.253	0.467	0.392	3.164	83.2	0.0189	0.0138	0.0193	0.0226	1.40	0.0169	0.0067	39
0.259	27.80	0.329	0.222	0.614	0.551	3.441	82.6	0.0178	0.0147	0.0213	0.0250	1.40	0.0190	0.0076	40
0.246	27.60	0.169	0.199	0.411	0.461	3.677	133.5	0.0148	0.0154	0.0228	0.0254	1.41	0.0143	0.0059	41
0.427	26.80	0.325	0.184	0.684	0.491	3.848	44.4	0.0212	0.0229	0.0314	0.0328	1.40	0.0220	0.0088	42
0.327	26.80	0.313	0.162	0.594	0.605	4.130	28.7	0.0301	0.0260	0.0368	0.0378	1.40	0.0275	0.0110	43
0.415	26.20	0.108	0.267	0.271	0.338	3.053	527.1	0.0089	0.0105	0.0177	0.0204	1.55	0.0092	0.0051	44
0.346	26.50	0.113	0.270	0.243	0.428	3.030	518.6	0.0101	0.0110	0.0188	0.0205	1.55	0.0093	0.0051	45
0.450	25.80	0.448	0.220	0.661	0.452	3.460	59.2	0.0236	0.0185	0.0238	0.0261	1.40	0.0230	0.0092	46
0.358	26.30	0.468	0.181	0.651	0.652	3.885	37.4	0.0265	0.0226	0.0285	0.0317	1.40	0.0285	0.0114	47
0.380	26.90	0.292	0.195	0.703	0.551	3.721	70.0	0.0209	0.0195	0.0264	0.0276	1.40	0.0218	0.0087	48
0.380	26.80	0.146	0.202	0.373	0.304	3.644	247.5	0.0131	0.0165	0.0247	0.0295	1.45	0.0130	0.0059	49
0.355	27.35	0.298	0.163	0.676	0.425	4.116	71.4	0.0228	0.0203	0.0285	0.0337	1.40	0.0212	0.0083	50
0.396	27.45	0.301	0.145	0.684	0.390	4.376	46.6	0.0241	0.0258	0.0365	0.0383	1.40	0.0268	0.0107	51
0.378	27.25	0.307	0.134	0.694	0.446	4.552	27.8	0.0315	0.0307	0.0430	0.0410	1.40	0.0330	0.0132	52
0.246	26.30	0.158	0.249	0.514	0.465	3.198	382.8	0.0108	0.0105	0.0167	0.0192	1.51	0.0113	0.0057	53
0.480	26.30	0.153	0.276	0.399	0.337	2.985	552.3	0.0100	0.0128	0.0193	0.0195	1.55	0.0102	0.0055	54
0.335	26.30	0.105	0.197	0.303	0.372	3.699	470.6	0.0094	0.0133	0.0219	0.0232	1.53	0.0108	0.0057	55
0.432	26.50	0.106	0.185	0.291	0.305	3.837	331.8	0.0108	0.0124	0.0209	0.0240	1.49	0.0117	0.0057	56
0.368	27.10	0.463	0.270	0.641	0.414	3.030	93.1	0.0208	0.0159	0.0216	0.0230	1.40	0.0190	0.0076	57
0.481	27.50	0.467	0.294	0.607	0.279	2.858	116.1	0.0197	0.0151	0.0201	0.0226	1.40	0.0175	0.0071	58
0.492	27.30	0.336	0.216	0.723	0.242	3.499	107.1	0.0168	0.0172	0.0241	0.0281	1.40	0.0181	0.0072	59
0.335	26.50		0.243	0.146	0.472	3.248	775.1	0.0102	0.0105	0.0182	0.0187	1.62	0.0094	0.0058	60
0.603	25.60	0.500	0.230	0.689	0.175	3.365	111.7	0.0205	0.0208	0.0271	0.0298	1.40	0.0205	0.0082	61
0.535	26.30	0.492	0.202	0.599	0.281	3.644	80.9	0.0207	0.0212	0.0286	0.0312	1.40	0.0232	0.0093	62
0.397	26.50	0.501	0.177	0.644	0.412	3.934	55.1	0.0261	0.0254	0.0342	0.0394	1.40	0.0277	0.0111	63
0.281	27.40	0.429	0.179	0.642	0.542	3.909	181.1	0.0185	0.0201	0.0285	0.0279	1.43	0.0195	0.0084	64
0.401	28.15	0.455	0.186	0.596	0.286	3.825	198.7	0.0182	0.0203	0.0280	0.0317	1.44	0.0187	0.0082	65
0.421	28.15	0.422	0.192	0.456	0.281	3.755	208.9	0.0202	0.0190	0.0273	0.0265	1.44	0.0182	0.0080	66
0.421	28.15	0.364	0.174	0.652	0.359	3.972	181.3	0.0183	0.0220	0.0312	0.0261	1.43	0.0195	0.0084	67
0.387	28.00	0.371	0.178	0.686	0.409	3.921	212.1	0.0157	0.0199	0.0286	0.0279	1.44	0.0180	0.0080	68
0.385	27.50	0.168	0.240	0.292	0.284	3.275	1452.0	0.0092	0.0106	0.0184	0.0215	1.76	0.0093	0.0071	69
0.398	27.20	0.163	0.214	0.644	0.393	3.519	1033.0	0.0094	0.0109	0.0173	0.0207	1.68	0.0100	0.0068	70
0.290	27.00	0.116	0.196	0.274	0.309	3.710	1796.0	0.0090	0.0108	0.0186	0.0204	1.81	0.0088	0.0071	71
0.323	27.20	0.117	0.148	0.274	0.331	4.331	770.0	0.0116	0.0119	0.0206	0.0208	1.62	0.0110	0.0067	72
0.315	27.20	0.164	0.198	0.593	0.408	3.688	762.0	0.0102	0.0118	0.0187	0.0211	1.61	0.0110	0.0067	73
0.378	26.10	0.163	0.190	0.262	0.435	3.778	733.0	0.0110	0.0150	0.0241	0.0236	1.61	0.0112	0.0068	74

Schönfeld's equation [37] (Table 2, column 29) and also on the basis of Equation (3.4.17) which is derived from the aforementioned Equation (3.4.16) for $\tau_0 = 0$, that is, for conditions similar to those assumed by Schijf and Schönfeld [37] (Table 2, column 28). It is observed that there is close agreement between the values of these last columns.

The values of f_i in columns 28 and 29 exceed the corresponding values in columns 26 and 27, based on direct measurements and on the rigorous integration of the equation of motion, respectively, by a margin of the order of 50 percent. This gives an idea of the order of magnitude of error introduced by the Schijf-Schönfeld's [37] simplified model.

The correlation of f_i, as obtained by each one of the above methods, to the pertinent flow and salinity parameters followed the general line of the author's early work [11]. After several trials it was found that f_i can be best correlated to the number $ReFr^2$ with the relative density difference $\Delta\rho/(\rho + \Delta\rho)$ taken as a parameter. Here Fr is the nondensimetric Froude number.

The dimensionless variable $ReFr^2$ is given by the equation

$$ReFr^2 = \frac{4V_1^3}{\nu g} = \frac{4V_0^3 I_R}{\nu g} \tag{6.4.9}$$

where

$$I_R = \frac{10}{[6(Fr_0')^{4/3} + 3(Fr_0')^{2/3} + 1]} \tag{6.4.10}$$

I_R is graphically given in Figure 3.3.

The correlations for the f_i computed from Equations (6.4.8) and (3.2.17) are presented in Figures 6.23 to 6.30. In the same figures values of f_i computed on the basis of Equations (3.4.16) and (3.4.17) have been plotted. Figures 6.31 and 6.32 summarize the curves of Figures 6.23 to 6.30 corresponding to the cases $T_0 \neq 0$ and $T_0 = 0$, respectively.

In Figures 6.33 (a), (b), and (c), data from other investigations are compared with the corresponding data of the present study. In Figures 6.33 (a) and 6.33 (b), Powell's [34] experimental results for $\Delta\rho/(\rho + \Delta\rho) = 0.022$ have been replotted and compared with the results of this study. When f_i is plotted against the Reynolds number only, as done by Powell [34], the two sets of data deviate strongly [Figure 6.33 (a)]; however, a close agreement is reached when both sets are plotted in Figure 6.33 (b) against $ReFr^2$. In particular, the drop of the curve for low values of $ReFr^2$ agrees with the trend observed in the author's experiments. Powell [34] gave as a law of variation of f_i the straight line given in Figure 6.33 (a) and he claimed that the point for $Re \cong 22{,}000$ seemed to be in error. This point, however, as we see in Figure 6.33 (b), is in agreement with the general law derived from this study when plotted against the appropriate parameter (Figure 6.31).

The curve corresponding to $\Delta\rho/(\rho + \Delta\rho) = 0.020$ has been replotted in Figure 6.33 (c) together with the reanalyzed laboratory data by Abraham and Eysink [1] and one field data point from the Mississippi estuary [31]. The agreement is quite good. This suggests that until the curves of Figure 6.31 are implemented with field data, they can

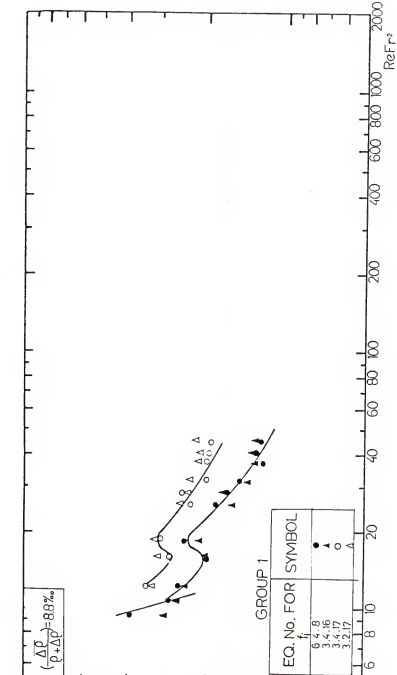

Figure 6.23 Correlation of f_i with $ReFr^2$ and $[(\Delta\rho)/(\rho + \Delta\rho)]$ (group 1)

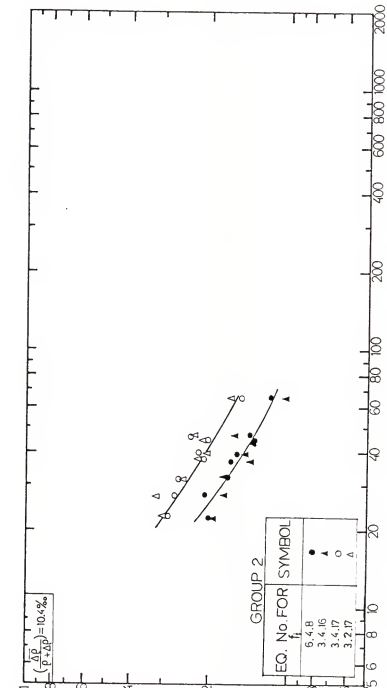

Figure 6.24 Correlation of f_1 with $ReFr^2$ and $[(\Delta\rho)/(\rho+\Delta\rho)]$ (group 2)

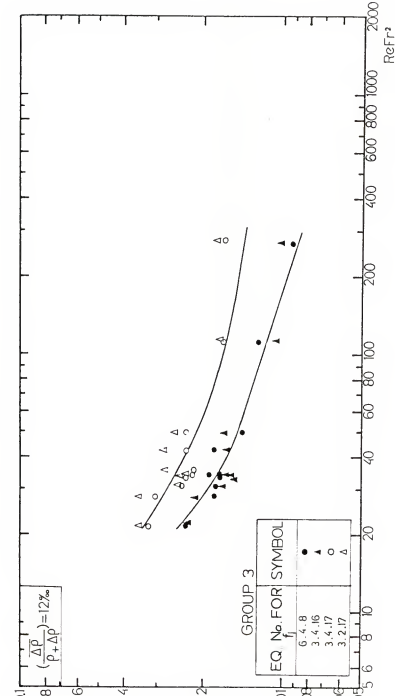

Figure 6.25 Correlation of f_i with $ReFr^2$ and $[(\Delta\rho)/(\rho+\Delta\rho)]$ (group 3)

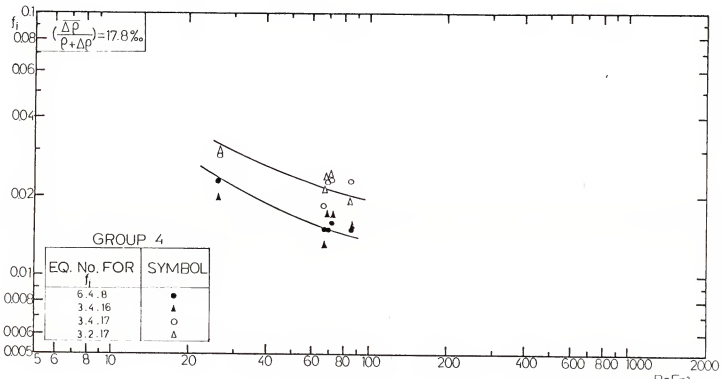

Figure 6.26 Correlation of f_f with $ReFr^2$ and $[\overline{(\Delta\rho)}/\overline{(\rho + \Delta\rho)}]$ (group 4)

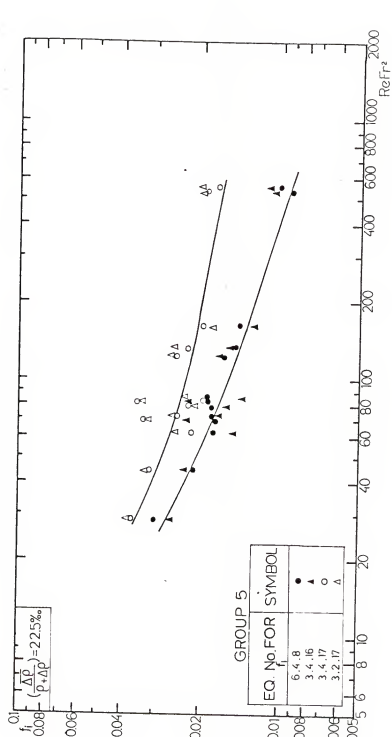

Figure 6.27 Correlation of f_i with $ReFr^2$ and $[(\Delta p)/(\rho + \Delta p)]$ (group 5)

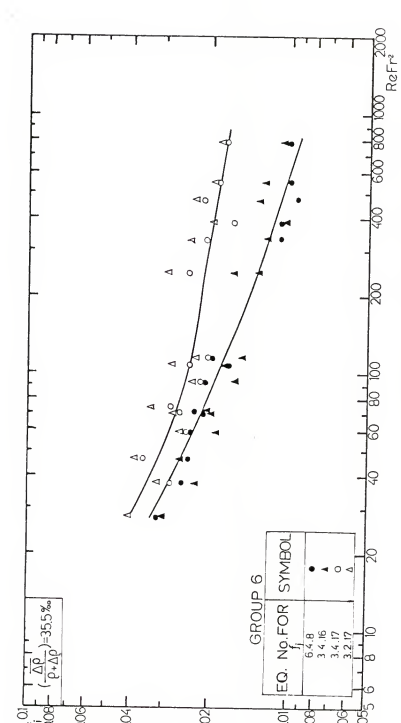

Figure 6.28 Correlation of f_i with Re_{Fr}^2 and $[(\Delta\rho)/(\rho + \Delta\rho)]$ (group 6)

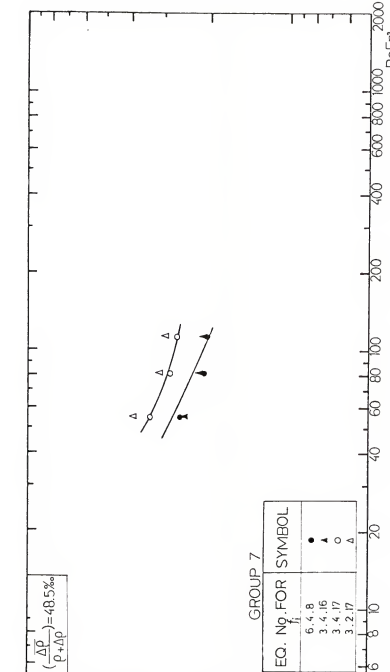

Figure 6.29 Correlation of f_i with $ReFr^2$ and $[(\Delta\rho)Y/(\rho + \Delta\rho)]$ (group 7)

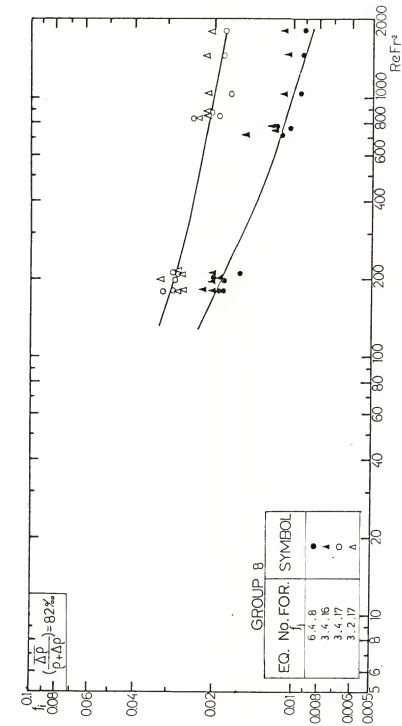

Figure 6.30 Correlation of f_i with $ReFr^2$ and $[(\overline{\Delta\rho})/(\rho + \overline{\Delta\rho})]$ (group 8)

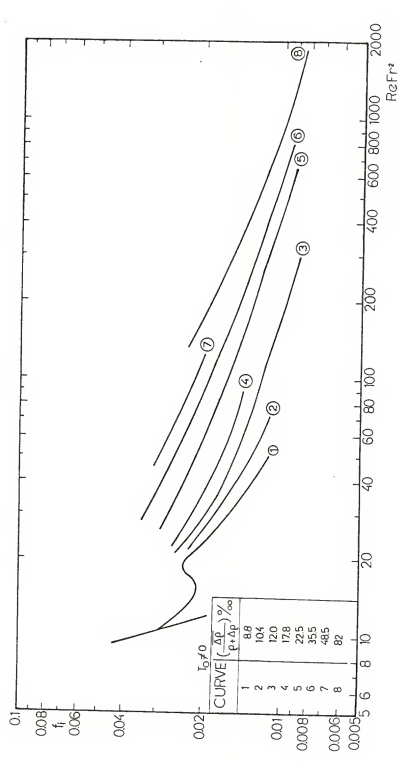

Figure 6.31. Variation of f_i with $ReFr^2$ and $[(\Delta\rho)/(\rho + \Delta\rho)]$ for $T_0 \neq 0$

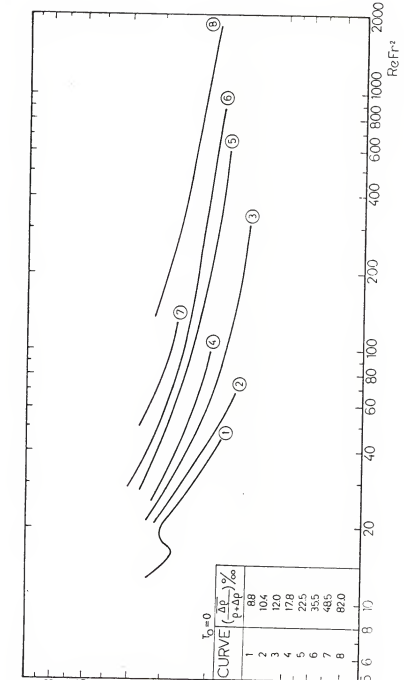

Figure 6.32 Variation of f_i with $ReFr^2$ and $[(\Delta\rho)/(\rho + \Delta\rho)]$ for $T_0 = 0$

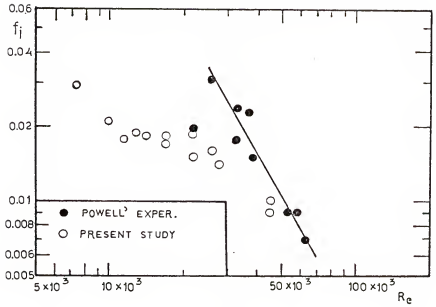

(a)

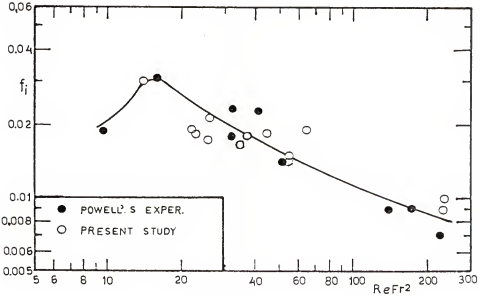

(b)

Figure 6.33 Comparison of data from other investigations with the corresponding data of the present study

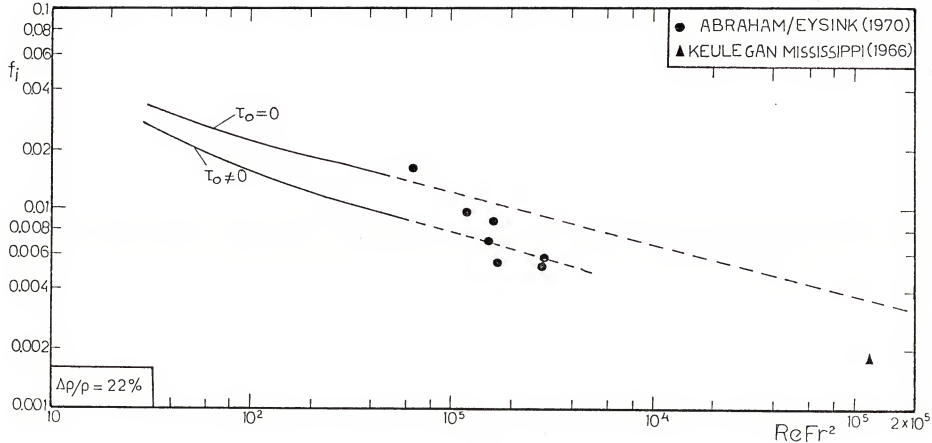

(c)

Figure 6.33—Continued

be tentatively extrapolated following the extrapolation of the $\Delta\rho/(\rho + \Delta\rho) = 0.020$ curve of Figure 6.33 (c).

The bed friction coefficient f_0 [Equation (3.4.15)] was evaluated in the following way. For each experiment the ratio $\lambda = h_s/h_{s1}$ [Figure 3.4 and Equation (3.4.14)] has been computed. In Figure 6.34, the quantity $\lambda - 1 = T_0/T_i$ is plotted against $ReFr^2$. It is observed that this ratio is independent of the salinity parameter $\Delta\rho/(\rho + \Delta\rho)$ and that it reaches a constant value equal to 0.4 for $ReFr^2 \leq 100$. For $ReFr^2 > 100$ the ratio T_0/T_i increases with $ReFr^2$. In particular, for $ReFr^2 = 2{,}000$ the bottom shear stresses, T_0, are equal to about 85 percent the value of the corresponding interfacial shear stresses, T_i. Knowing λ and f_i, the bed friction factor, f_0, can readily be computed. In the computation of f_0, the values of f_i have been taken from the graph of Figure 6.31 ($f_i = f_{ig}$) and are tabulated in column 31 of Table 2. Likewise, the values of λ have been taken equal to λ_g, that is equal to the value corresponding to the curve of Figure 6.31. These values are tabulated in column 30 of Table 2.

The correlation of f_0 with $ReFr^2$ for different values of $\Delta\rho/(\rho + \Delta\rho)$ is given in Figure 6.35.

The graphs of Figures 6.31 and 6.34 or 6.35 can be applied to practical problems, for the calculation of f_i or f_0, because the introduced parameters can be readily defined. A comparison of Figure 6.35 with Figure 2.5 leads to the justification of the earlier conclusion, based on the review of earlier work, that both the interfacial and bed friction factors cannot be universally expressed as a function of one

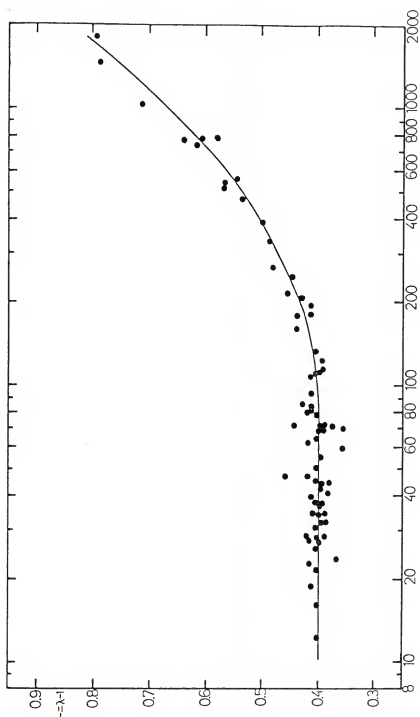

Figure 6.34 Variation of T_0/T_i with $ReFr^2$

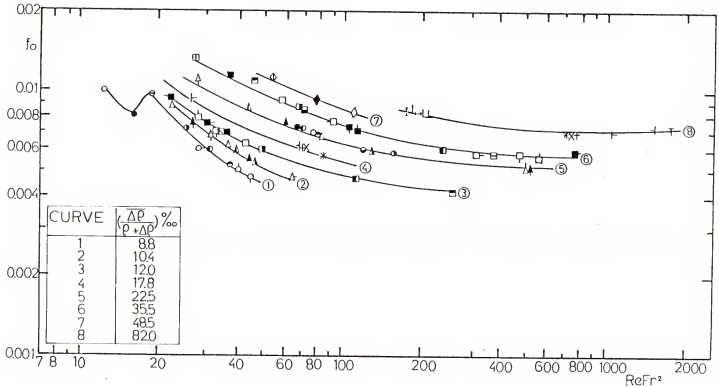

Figure 6.35 Variation of f_0 with $ReFr^2$ and $[\overline{(\Delta\rho)}/(\rho + \Delta\rho)]$

of the commonly used dimensionless parameters only (Re, Fr'_0, or Keulegan's number).

6.5 Velocity Distribution Laws

According to section 6.3, the experiments of this study indicated that the velocity distribution follows a linear law within a relatively thin zone around the velocity interface, while above and below that zone the velocity distribution becomes logarithmic.

The objective of this section is the detailed analytical formulation of these laws. This was accomplished in the following way. First, from the values of f_{ig} (Table 2, column 31) and from the mean velocity V_1, of the upper layer at the cross section of measurements, the friction velocity, u_*, was computed for each experiment on the basis of the equation

$$u_* = V_1\sqrt{\frac{f_i}{8}} \tag{6.5.1}$$

The velocity U/2, corresponding approximately to the velocity at the interface, has been taken as a reference velocity. The velocity difference u - U/2 was next nondimensionalized by u_*; the corresponding vertical distance y - y_0 or y_0 - y was also nondimensionalized by ν/u_*. The dimensionless velocities have been plotted in Figures 6.36 to 6.43 against the dimensionless vertical distance with $\overline{\Delta\rho/(\rho + \Delta\rho)}$ as a parameter. Here bars indicate average values. These plots lead to the following law for the interface:

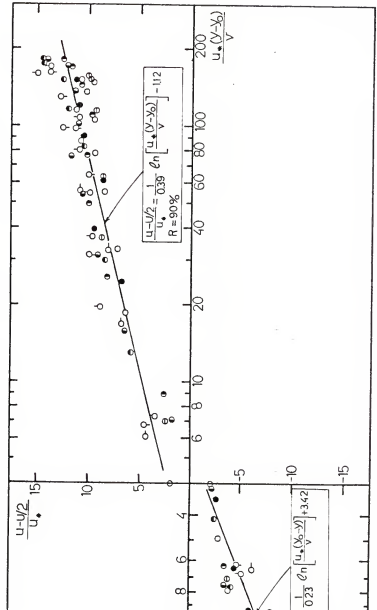

Figure 6.36 Dimensionless velocity distribution outside of the linear zone (group 1)

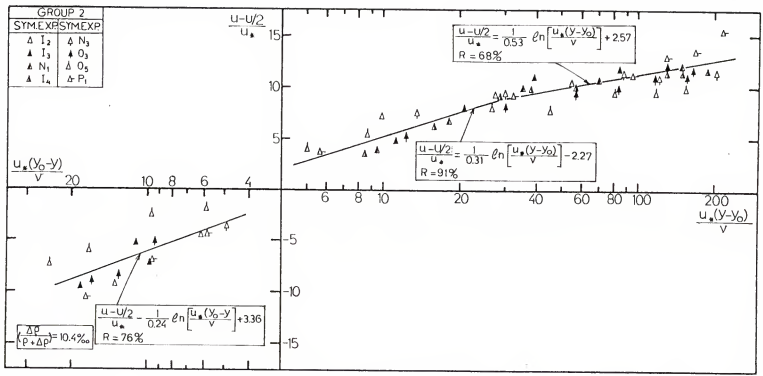

Figure 6.37 Dimensionless velocity distribution outside of the linear zone (group 2)

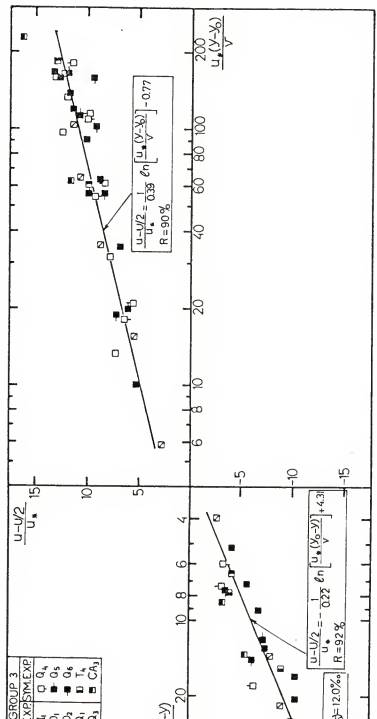

Figure 6.38 Dimensionless velocity distribution outside of the linear zone (group 3)

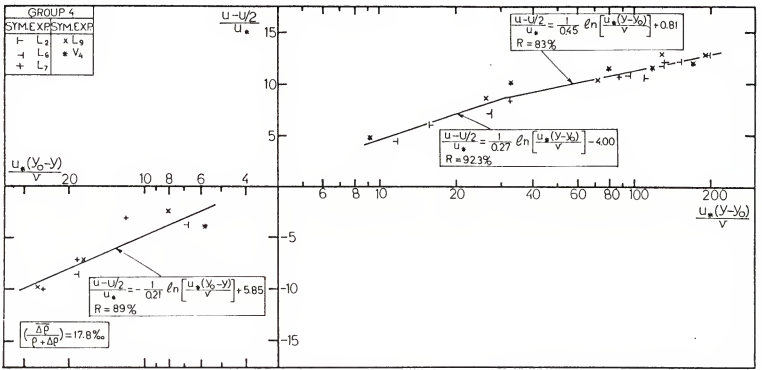

Figure 6.39 Dimensionless velocity distribution outside of the linear zone (group 4)

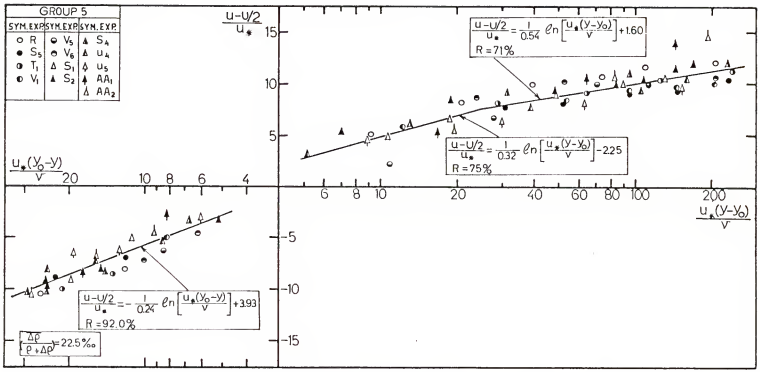

Figure 6.40 Dimensionless velocity distribution outside of the linear zone (group 5)

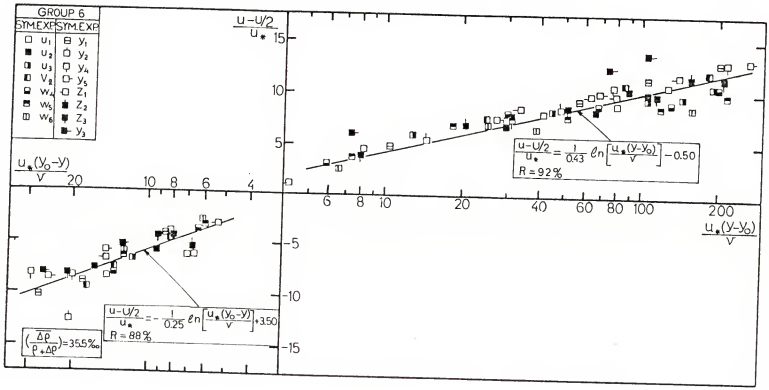

Figure 6.41 Dimensionless velocity distribution outside of the linear zone (group 6)

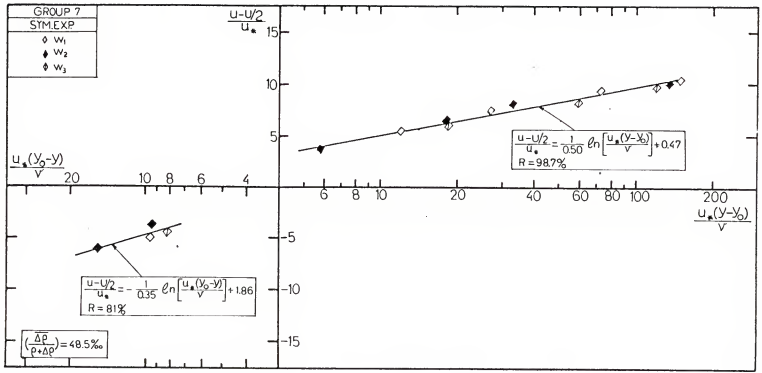

Figure 6.42 Dimensionless velocity distribution outside of the linear zone (group 7)

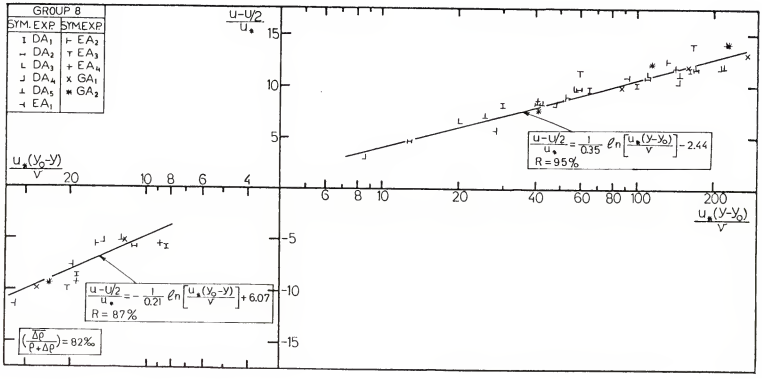

Figure 6.43 Dimensionless velocity distribution outside of the linear zone (group 8)

$$\frac{u - U/2}{u_*} = \frac{1}{k_3} \ln \left[\frac{u_*(y - y_0)}{\nu}\right] + c_3 \qquad (6.5.2)$$

for the upper zone, δu, and

$$\frac{u - U/2}{u_*} = \frac{1}{k_2} \ln \left[\frac{u_*(y_0 - y)}{\nu}\right] + c_2 \qquad (6.5.3)$$

for the lower zone δu_1, where k_2, k_3, c_2, and c_3 are coefficients to be defined later. As a first approximation, the mean values of these coefficients from the graphs of Figures 6.36 to 6.43 are taken and introduced into Equations (6.5.2) and (6.5.3) which then take the form

$$\frac{u - U/2}{u_*} = \frac{1}{0.37} \ln \left[\frac{u_*(y - y_0)}{\nu}\right] - 1.61 \qquad (6.5.4)$$

for the upper zone and

$$\frac{u - U/2}{u_*} = -\frac{1}{0.24} \ln \left[\frac{u_*(y_0 - y)}{\nu}\right] + 3.70 \qquad (6.5.5)$$

for the lower zone.

A more careful study of the graphs, however, leads to the observation that the dimensionless velocity distribution curve differs for each experiment (examples in Figures A.13 to A.19 of the Appendix). More specifically, the slope of the straight line portion of each experiment, sometimes, deviates from the slope of the mean straight line of the corresponding group of experiments. The analysis of the

experimental data, on the basis of straight lines of each experiment instead of the mean line of the group is presented in Table 3, where a_2, a_3, b_2, and b_3 are coefficients of Equations (6.4.3) and (6.4.4). Then k_2, k_3, c_2, and c_3 of Equations (6.5.2) and (6.5.3) are correlated with the flow and salinity parameters. The correlations for k_2 and k_3 are given in Figures 6.44 and 6.45, respectively, and the correlations for c_2 and c_3 are presented in Figure 6.46. The straight lines of Figure 6.44 can be expressed by the relations

$$k_3 = \left[\frac{0.77}{(\delta u/h_0)(ReFr^2)^{0.4}}\right]^{1/3} \tag{6.5.6}$$

and

$$k_2 = -\left[\frac{0.77}{\sqrt{\delta u_1/h_s}\,\sqrt[3]{ReFr^2}}\right]^{1/2} \tag{6.5.7}$$

The equations for the curves of Figure 6.46 are

$$c_3 = 9.50\ \ell n\ |k_3| + 7.97 \tag{6.5.8}$$

and

$$c_2 = -\ 6.37\ \ell n\ |k_2| - 4.71 \tag{6.5.9}$$

The correlation coefficient of Equations (6.5.8) and (6.5.9) appears to be satisfactory. From the graphs of Figures 6.44 and 6.45 and from Equations (6.5.6) and (6.5.7) it can be concluded that k_2

Table 3. Correlation of k and c coefficients with the flow and salinity parameters

Exp.	$\frac{\Delta\rho}{\rho+\Delta\rho}$	Re_{Fr}^2	$\frac{U}{V_1}$	a_2	a_3	K_2	K_3	Φ_2	Φ_3	C_2	C_3	β_2	β_3
1	2	3	4	5	6	7	8	9	10	11	12	13	14
P_{10}	7.9	12.2	1.140	-0.122	0.130	-0.42	0.39	6.91	9.00	1.38	-1.61	0.019	1.037
P_9	8.2	16.0	1.158	-0.123	0.143	-0.35	0.33	11.70	9.24	0.82	-1.98	0.009	1.100
P_7	8.7	25.4	1.163	-0.120	0.171	-0.34	0.24	11.72	12.82	1.58	-6.12	0.027	1.122
P_6	9.0	31.6	1.146	-0.078	0.141	-0.48	0.26	21.07	15.29	0.32	-4.40	0.158	1.054
P_5	9.3	37.4	1.208	-0.112	0.112	-0.32	0.32	21.72	16.16	1.92	-2.26	0.058	0.981
O_6	9.4	18.8	1.109	-0.099	0.175	-0.49	0.27	13.10	11.22	0.88	-4.23	0.098	1.160
P_4	9.7	40.7	1.202	-0.099	0.129	-0.43	0.26	28.94	19.10	-0.73	-3.77	0.085	1.030
N_4	9.5	28.6	1.077	-0.121	0.107	-0.35	0.39	18.15	18.06	0.25	-0.44	-0.016	1.006
P_2	9.8	45.0	1.136	-0.108	0.119	-0.31	0.26	23.42	17.06	1.39	-2.27	0.081	1.061
I_2	10.8	37.1	1.126	-0.111	0.118	-0.35	0.34	24.50	16.56	0.54	0.02	0.054	1.071
I_3	10.6	44.3	1.144	-0.110	0.143	-0.33	0.25	22.10	20.34	2.06	-4.31	0.051	1.075
I_4	10.5	46.4	1.113	-0.081	0.170	-0.45	0.23	40.20	17.39	-1.67	-5.83	0.117	1.170
N_1	10.3	39.5	1.098	-0.149	0.158	-0.27	0.25	30.70	17.80	2.24	-5.06	-0.040	1.137
N_3	10.1	31.9	1.074	-0.127	0.145	-0.34	0.31	15.29	19.36	1.05	-1.17	-0.041	1.156
O_3	10.7	27.3	1.129	-0.101	0.133	-0.43	0.33	24.01	13.86	0.85	-2.29	0.119	1.055
O_5	10.0	22.2	1.145	-0.093	0.152	-0.49	0.32	17.06	10.56	1.81	-1.57	0.168	1.184
P_1	10.0	64.3	1.128	-0.129	0.117	-0.26	0.29	35.88	23.04	2.33	-2.38	0.004	1.033
I_1	12.0	34.4	1.155	-0.110	0.126	-0.37	0.31	25.81	17.69	1.10	-3.04	0.078	0.993
O_1	11.1	42.7	1.136	-0.124	0.144	-0.32	0.26	33.64	20.07	-0.67	-2.97	-0.050	1.106
O_2	11.1	34.5	1.187	-0.131	0.113	-0.25	0.34	28.84	17.47	2.42	-2.68	-0.027	0.955
O_1	12.5	49.8	1.132	-0.107	0.131	-0.33	0.29	38.44	20.52	1.03	-3.08	-0.055	1.051
O_3	12.6	28.0	1.146	-0.145	0.151	-0.31	0.29	16.73	13.84	3.02	-4.74	-0.063	1.067
O_4	11.6	34.2	1.114	-0.123	0.135	-0.34	0.31	22.28	15.84	1.86	-2.91	0.056	1.048

$\Phi_2 = \left(\sqrt[3]{Re_{Fr}^2} / \sqrt{\delta u_1 / h_s} \right)^2$, $\Phi_3 = \left(\sqrt[3]{Re_{Fr}^2} / \sqrt{\delta u / h_o} \right)^2$

Table 3—Continued

1	2	3	4	5	6	7	8	9	10	11	12	13	14
O_5	11.3	30.8	1.102	-0.124	0.127	-0.34	0.32	20.25	14.59	1.95	-3.47	0.056	0.990
O_6	11.3	21.0	1.110	-0.148	0.162	-0.34	0.30	17.14	12.25	2.65	-2.71	-0.031	1.166
T_4	12.1	111.5	1.025	-0.128	0.103	-0.30	0.35	55.85	124.99	2.56	-0.24	0.025	0.996
CA_3	12.0	267.5	1.055	-0.118	0.111	-0.20	0.28	87.24	209.38	3.84	-4.13	0.013	0.925
L_2	16.6	23.3	1.152	-0.098	0.080	-0.48	0.54	17.72	12.11	1.45	0.06	0.153	0.943
L_6	17.3	60.7	1.142	-0.120	0.136	-0.31	0.29	41.86	26.73	2.08	-3.99	0.007	1.036
L_7	16.0	69.1	1.156	-0.075	0.151	-0.45	0.25	24.80	25.10	2.16	-5.30	0.139	1.070
L_9	16.8	70.8	1.123	-0.135	0.114	-0.20	0.33	35.78	37.09	4.76	-1.02	0.054	0.900
V_4	18.9	05.3	1.033	-0.090	0.154	-0.42	0.27	39.06	60.84	-0.37	-3.24	0.106	1.161
R	20.9	78.3	1.185	-0.100	0.151	-0.21	0.26	19.80	26.73	4.46	-3.50	-0.180	1.151
S_5	20.9	68.8	1.117	-0.143	0.152	-0.30	0.28	37.70	34.93	2.16	-4.12	-0.055	1.128
T_1	20.7	159.9	1.049	-0.209	0.134	-0.19	0.29	80.10	77.97	6.22	-3.52	-0.171	1.120
V_1	22.5	72.3	1.065	-0.166	0.138	-0.27	0.34	28.10	40.96	2.76	-1.56	-0.130	1.132
V_5	19.8	123.0	1.043	-0.197	0.127	-0.21	0.32	74.48	110.67	3.53	-3.39	-0.200	1.010
V_6	20.9	02.3	1.029	-0.215	0.196	-0.21	0.23	45.43	60.22	3.80	-5.20	-0.268	1.310
S_1	24.0	83.2	1.109	-0.114	0.122	-0.37	0.34	48.72	40.83	1.58	-2.07	0.041	1.000
S_2	24.1	62.6	1.118	-0.174	0.136	-0.25	0.32	28.62	25.60	3.34	-0.75	-0.107	1.143
S_4	23.8	133.5	1.086	-0.189	0.149	-0.21	0.27	56.70	63.52	5.32	-3.77	-0.203	1.136
O_4	25.1	44.4	1.132	-0.155	0.094	-0.30	0.40	25.50	18.32	2.18	-0.30	-0.106	0.960
O_5	23.5	28.7	1.156	-0.126	0.100	-0.42	0.52	15.44	15.76	1.37	0.08	-0.006	0.990
AA_1	23.9	527.1	1.030	-0.198	0.127	-0.17	0.26	193.20	240.87	9.73	-5.61	-0.215	1.030
AA_2	23.4	518.6	1.030	-0.161	0.125	-0.22	0.27	150.60	265.36	5.59	-5.29	-0.152	1.009
O_1	33.2	59.2	1.141	-0.132	0.104	-0.34	0.44	33.64	23.04	0.13	-0.35	-0.083	0.980
O_2	33.8	37.4	1.185	-0.113	0.132	-0.44	0.37	17.13	17.14	0.46	-2.96	-0.006	0.980
U_3	30.7	70.0	1.129	-0.116	0.124	-0.39	0.37	30.80	24.11	0.95	-2.42	0.010	1.092
V_2	32.0	247.5	1.052	-0.158	0.118	-0.24	0.33	129.73	105.68	3.78	-2.54	-0.095	1.037

Table 3—Continued

1	2	3	4	5	6	7	8	9	10	11	12	13	14
W_4	40.2	71.4	1.123	-0.147	0.139	-0.31	0.33	40,58	25.50	2.28	-1.88	-0.046	1.129
W_5	37.1	46.6	1.114	-0.80	0.148	-0.57	0.34	33.17	18,92	0.06	-1.79	0.141	1.159
W_6	30.7	27.8	1.126	-0.100	0.173	-0.52	0.34	20.61	13.25	0.69	-2.55	0.096	1.209
Y_1	32.5	382.8	1.090	-0.217	0.096	-0.14	0.36	113.42	102,41	11.31	-2.06	-0.256	0.990
Y_2	34.0	552.3	1.106	-0.111	0.096	-0.29	0.34	199,66	168,48	0.29	-2.83	-0.036	0.960
Y_4	35.7	470.6	1.067	-0.147	0.129	-0.23	0.26	162.82	199,66	5.40	-5.66	-0.060	1.038
Y_5	31.9	331.8	1.037	-0.139	0.106	-0.26	0.35	157.00	164,35	4.44	-2.03	0.010	1.007
Z_1	32.8	93.1	1.150	-0.091	0.137	-0.46	0.31	49.84	32.04	0.55	-3.30	0.118	1.030
Z_2	32.6	116.1	1.107	-0.004	0.148	-0.51	0.28	85,38	39,19	-0.70	-3.76	0.128	1.062
Z_3	35.5	107.1	1.122	-0.129	0.134	-0.33	0.32	93,32	31,25	2.30	-2.85	0.052	1.086
Y_3	34.4	775.1	1.037	-0.099	0.099	-0.32	0.32	179,02	578,40	2.81	-0.94	0.047	0.970
W_1	49.5	111.7	1.000	-0.065	0.126	-0.72	0.35	132,71	33,64	-0.30	-1.02	0.250	1.057
W_2	49.0	80.9	1.096	-0.086	0.128	-0.52	0.38	66,42	31,13	0.36	-1.20	0.150	1.057
W_3	47.5	55.1	1.157	-0.106	0.133	-0.51	0.37	35,28	22,56	0.02	-1.82	0.059	1.041
DA_1	93.0	181.1	1.133	-0.146	0.131	-0.29	0.32	59,14	49.84	1.62	-2.32	-0.120	1.070
DA_2	93.5	198.7	1.133	-0.063	0.111	-0.67	0.38	119,24	57,15	-0.70	-1.79	0.197	0.980
DA_3	90.0	208.9	1.094	-0.087	0.162	-0.49	0.27	125,22	77,09	1.04	-4.79	0.179	1.069
DA_4	85.8	181.3	1.143	-0.122	0.108	-0.36	0.39	89,30	49.00	2.15	-2.32	0.071	0.970
DA_5	82.4	212.1	1.135	-0.081	0.110	-0.52	0.30	86.86	51.84	1.04	-1.78	0.172	1.017
EA_1	81.1	1452.0	1.063	-0.095	0.131	-0.33	0.24	451,14	438,90	2.77	-8.14	0.117	0.970
EA_2	78.3	1033.0	1.006	-0.168	0.137	-0.20	0.24	260.18	158,73	8.40	-8.26	-0.022	1.086
EA_3	88.2	1796.0	1.035	-0.205	0.186	-0.16	0.17	478,73	539,63	10.00	-12.30	-0.224	1.194
EA_4	82.3	770.0	1.048	-0.160	0.116	-0.21	0.30	254.08	306,95	5.07	-4.65	-0.096	0.980
GA_1	70.4	762.0	1.100	-0.181	0.115	-0.19	0.29	204,20	140.66	8.54	-5.90	-0.115	1.010
GA_2	72.6	733.0	1.054	-0.135	0.147	-0.27	0.24	187.42	311.17	3.65	-8.24	-0.036	0.990

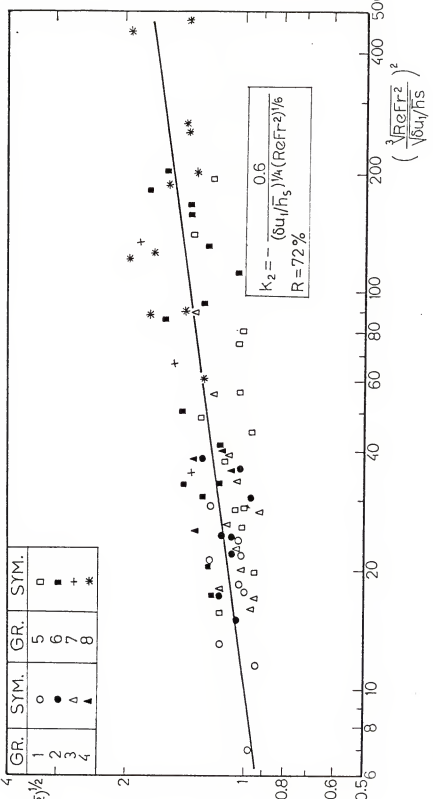

Figure 6.44 Correlation of k_2 with the flow and salinity parameters

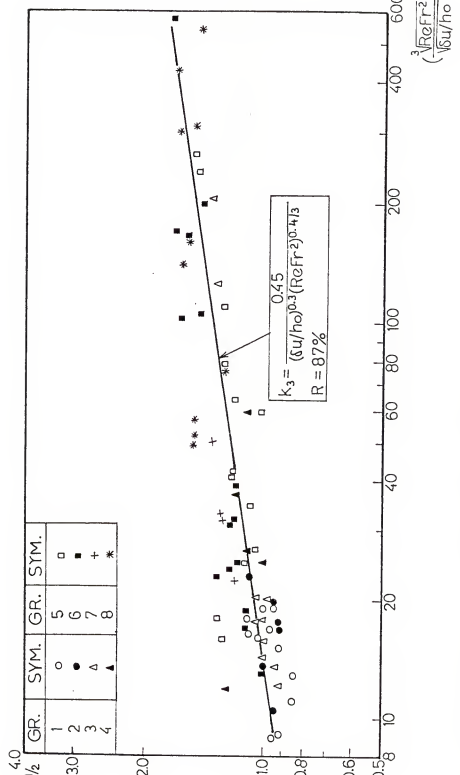

Figure 6.45 Correlation of k_3 with the flow and salinity parameters

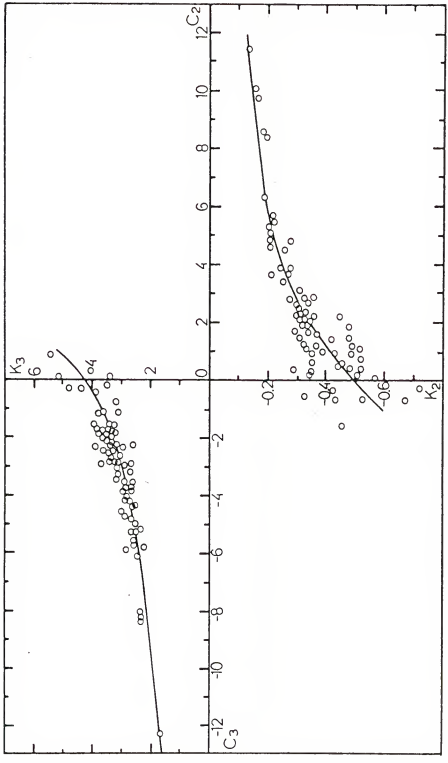

Figure 6.46 Correlation of k_2 and k_3 with c_2 and c_3

and k_3 are not constants but they depend on the flow and salinity parameters. Therefore, Csanady's conclusion [9] that k_3 is constant and equal to von Karman's universal constant is not correct. In the same way c_2 and c_3 depend on the same parameters, since they are expressed in terms of k_2 and k_3. The graphs of Figures 6.36 to 6.43 or the graphs of Figures 6.44 to 6.46 and Equations (6.5.2) and (6.5.3) clearly define the velocity distribution in the zones δu and δu_1. A first approximation of the velocity distribution in the zones δu and δu_1 is given by Equations (6.5.4) and (6.5.5), where k and c are constants. A better approach to the problem is obtained by the equations of Figures 6.36 to 6.43 where k and c are functions of $\Delta\rho/(\rho + \Delta\rho)$. These procedures can be readily applied to practical problems. Another approach is obtained by means of the Equations (6.5.2) and (6.5.3) through Equations (6.5.6) to (6.5.9).

CHAPTER VII
SUMMARY AND CONCLUSIONS

The dynamics of arrested saline wedges and, specifically, the functional dependence of the shear stresses at the interface and at the bed and the velocity distribution in the neighborhood of the interface have been experimentally investigated. The experiments were conducted in a special open flume equipped with all the accessories for the necessary measurements and control. A total of 74 experiments have been conducted for a wide range of values of the primary independent parameters. The relative density difference $\Delta\rho/(\rho + \Delta\rho)$ ranged between 8 $^{o}/_{oo}$ and 93 $^{o}/_{oo}$. The analysis of the experimental data of the present work confirmed an earlier derived law on the density distribution [34] of the form

$$\frac{\rho_{\ell} - \rho}{\rho + \Delta\rho} = \frac{1}{2}\left[1 - \tanh\left(\frac{y - h_s}{\delta/2}\right)\right] \tag{7.1}$$

The interfacial friction coefficients, f_i, have been computed by four different approaches:

1. From direct measurements of the velocity profiles and Reynolds stresses near the interface on the basis of the equation [Equation (6.4.8)]

$$\tau_{imax} = \left(\mu\frac{du}{dy} - \rho\overline{u'v'}\right)_{imax} = \frac{f_i\rho\overline{V_1^2}}{8} \tag{7.2}$$

where τ_{imax} is the maximum value of the shear stresses in the neighborhood of the interface.

2. Through the integration of the equations of motion in the vertical direction and subsequent averaging through a second integration in the horizontal direction over the actual intrusion length, L_0, making use of the measured velocity profiles, the shape of the interface and other pertinent quantities. This equation finally takes the form [Equation (3.4.16)]

$$\frac{T_i}{v_0^2} = \left[\frac{\left[\left[\frac{\Delta\rho}{\rho}\right] g h_{s0} + 2\beta(1 + \Delta\rho/\rho)\varepsilon^2 v_{10}^2\right] h_{10}\bar{h}_1 - 2\alpha V_0^2 h_0 \bar{h}_s}{2V_0^2 h_{10}(\lambda\bar{h}_1 + \bar{h}_s)}\right]$$

$$\cdot \frac{h_{s0}}{L_0} - \frac{0.0559}{b^{1.25}} h_0^2 \left(\frac{\nu}{V_0 h_0}\right)^{0.25} \cdot \left[\frac{\overline{(b + 2h_1)^{0.25}}}{h_1}\right]$$

$$\cdot \frac{\bar{h}_s}{(\lambda\bar{h}_1 + \bar{h}_s)} = \frac{f_i}{8} \cdot \overline{\left(\frac{V_1}{V_0}\right)^2} \qquad (7.3)$$

where bars indicate mean values of the corresponding parameters.

3. From Schijf and Schönfeld's equation [37] [Equation (3.2.17)]

$$f_i = \frac{2h_0}{L}\left[\frac{1}{5(Fr_0')^2} - 2 + 3(Fr_0')^{2/3} - \frac{6}{5}(Fr_0')^{4/3}\right] \qquad (7.4)$$

where Fr_0' is the densimetric Froude number upstream of the wedge.

4. From a simplification of Equation (7.3) for $\tau_0 = 0$, an assumption used by Schijf and Schönfeld [37] in their mathematical model. Equation (7.3) reduces then to the form (3.4.17)

$$\frac{T_i}{\rho \overline{V_0^2}} = \left[\frac{(\Delta\rho/\rho) g \overline{h}_1 h_{s0}}{2 V_0^2 h_0} - \frac{\alpha \overline{h_s}}{h_{10}}\right] \frac{h_{s0}}{L_0} \tag{7.5}$$

The bed friction coefficient, f_0, has been computed on the basis of a linear relation between interfacial and bed shear stresses, that is,

$$T_0 = (\lambda - 1) T_i = \frac{f_0 \rho \overline{V_1^2}}{8} \tag{7.6}$$

This relationship was utilized in the derivation of Equation (7,3). The analysis of the experimental data on the coefficients f_i and f_0 led to the following conclusions:

1. The best correlation of f_i and f_0 with the flow and salinity parameters has been obtained when these coefficients were plotted against the dimensionless parameter $ReFr^2 = 4\overline{V_1^3}/\nu g$ with $\Delta\rho/(\rho + \Delta\rho)$ as an independent parameter (Figures 6.23 to 6.32 and Figure 6.35). The values of f_0 are substantially lower than those of f_i. This conclusion and the derived functional

dependence of both coefficients on these two distinct parameters are drastically different from the results of all known previous studies, but in agreement with the author's earlier work [11] regarding f_i alone.

2. The graphs of Figures 6.23 to 6.30 give the variation of f_i with respect to $ReFr^2$ for different values of $\Delta\rho/(\rho + \Delta\rho)$. The lower curve of each graph is based on the approach given by Equation (6.4.8) or Equation (7.2) The agreement with the results based on Equation (3.4.16) or Equation (7.3) is very good. The upper curve is based on the approach given by Equation (3.4.17) or Equation (7.5) where τ_0 is considered equal to zero. The agreement with the results based on Schijf and Schönfeld's mathematical model [37] [Equation (3.2.17) or Equation (7.4)] is also very good. Figures 6.31 and 6.32 contain the summary of the lower curves, corresponding to $\tau_0 \neq 0$, and the upper curves corresponding to $\tau_0 = 0$ of Figures 6.23 to 6.30, respectively. From these graphs the error in the values of f_i can be readily estimated when the Schijf and Schönfeld mathematical model [37] is used. For example, for $ReFr^2 = 200$ and $\Delta\rho/(\rho + \Delta\rho) = 22.5\ ^0/_{00}$ the relative error is 54 percent of the real value.

3. The graph of Figure 6.34 gives the law of variation of the ratio of bed shear stresses to the interfacial shear stresses, T_0/T_i. It is observed that (a) the ratio T_0/T_i is independent of the density variation and (b) the above ratio is constant and equal to 0.4 for low values of

$ReFr^2$, especially for $ReFr^2 \leq 100$, while for $ReFr^2 > 100$, T_0/T_i is approximately given by the equation

$$\frac{T_0}{T_i} = \frac{2}{15} \ln (ReFr^2) - 0.26 \tag{7.7}$$

with a correlation coefficient of 95.2 percent.

4. The law of variation of f_0 with the flow and salinity parameters is given by the graph of Figure 6.35. The values of f_0 were calculated from the following equation:

$$f_0 = f_i(\lambda - 1) \tag{7.8}$$

which was derived from Equation (7.6) with T_i substituted by $f_i \rho \overline{V_1^2}/8$. The values of f_i and $\lambda - 1$ were taken from the graphs of Figures 6.31 and 6.34, respectively.

The laws given by the graphs of Figures 6.31, 6.34, and 6.35 can be easily applied to practical problems.

Considering the flow structure within the interfacial zone, the following results and conclusions have been obtained:

1. There exists a relatively thin core near the density interface within which the dimensionless velocity distribution is linear (Figures 6.10 and 6.11). This distribution is given by the equation

$$\frac{u - U/2}{U} = 5\left(\frac{y - y_0}{\delta u_2}\right) \tag{7.9}$$

The symbols have been defined in Figure 6.4. The linear law appears to be independent of salinity.

2. Outside of the linear zone the dimensionless velocity distribution follows a logarithmic law (Figures 6.12 to 6.19 and Figures 6.36 to 6.43) which can be expressed for the zone δu (Figure 6.4) by the equations

$$\frac{u}{U} = a_3 \ln \left(\frac{y - y_0}{\delta u} \right) + b_3 \tag{7.10}$$

or

$$\frac{u - U/2}{u_*} = \frac{1}{k_3} \ln \left(\frac{u_*(y - y_0)}{\nu} \right) + c_3 \tag{7.11}$$

and for the zone δu_1 (Figure 6.4) by the equations

$$\frac{u}{U} = a_2 \ln \left(\frac{y_0 - y}{5\delta u_1} \right) + b_2 \tag{7.12}$$

or

$$\frac{u - U/2}{u_*} = \frac{1}{k_2} \ln \left(\frac{u_*(y_0 - y)}{\nu} \right) + c_2 \tag{7.13}$$

where the values of the parameters a_3, a_2, b_3, b_2, and k_3, k_2, c_3, c_2 are given in Figures 6.12 to 6.19 and Figures 6.36 to 6.43, respectively, with each figure corresponding to a particular value of the relative density difference. In each of these graphs, and particularly in Figures A.6 to A.19 of the Appendix, two

intersected straight lines of different slopes can be distinguished in each of the two zones, δu and δu_1.

3. In the zone δu the intersection of the straight lines occurs at a relative distance $(y - y_0)/\delta u$ of approximately 0.15 (Figures 6.12 to 6.19 and Figures A.6 to A.12 of the Appendix). The first straight line corresponding to the logarithmic distribution immediately next to the linear zone and extending until the point where $(y - y_0)/\delta u = 0.15$, constitutes the "law of the interface" of the upper layer. This law is analogous to the wall law for homogeneous fluids and solid boundaries. In the zone δu_1 the intersection of the two straight line segments occurs at $(y_0 - y)/5\delta u_1 = 0.1$. The straight line immediately next to the linear zone and up to the previous point of intersection constitutes the law of the interface of the lower layer. The laws of the interface can be expressed by the following approximations:

   a. A first approximation is given by the equation

$$\frac{u - U/2}{u_*} = \frac{1}{0.37} \ln \left[\frac{u_*(y - y_0)}{\nu}\right] - 1.61 \qquad (7.14)$$

   for the zone δu, and by the equation

$$\frac{u - U/2}{u_*} = -\frac{1}{0.24}\,\ell n\left[\frac{u_*(y_0 - y)}{\nu}\right] + 4.04 \qquad (7.15)$$

for the zone δu_1. Here the parameters k_3, k_2, c_3, and c_2 of Equations (7.11) and (7.13) are taken constant and equal to the mean of their corresponding values from Figures 6.36 to 6.43.

b. A second approximation is given by the graphs of Figures 6.36 to 6.43, where the previous parameters appear to be functions of the relative density difference $\Delta\rho/(\rho + \Delta\rho)$.

c. A third approximation can be obtained from the graphs of Figures 6.44 to 6.46 where the parameters k_3, k_2, c_3, and c_2 are given as follows:

$$k_3 = \left[\frac{0.77}{(\delta u/h_0)(ReFr^2)^{0.4}}\right]^{1/3} \qquad (7.16)$$

$$k_2 = -\left[\frac{0.77}{\sqrt{\delta u_1/h_s}\,\sqrt[3]{ReFr^2}}\right]^{1/2}$$

and

$$c_3 = 9.50\,\ell n\,|k_3| + 7.97 \qquad (7.17)$$

$$c_2 = -6.37\,\ell n\,|k_2| - 4.71$$

It follows that there are two laws for the interface for each layer, respectively. The parameters k_3 and k_2 are not constant, as Csanady [9] claims, but functions of the flow and salinity parameters.

4. The straight line in the semilog plot, which is defined between the points of $(y - y_0)/\delta u = 0.15$ and $(y - y_0)/\delta u = 1$ for the zone δu and between the points $(y_0 - y)/5\delta u_1 = 0.1$ and $(y_0 - y)/5\delta u_1 = 0.22$ for the zone δu_1 defines the "outer region law" for each layer (Figures 6.12 to 6.19, 6.36 to 6.43, and A.6 to A.19). These laws are given as functions of the relative density $\Delta\rho/(\rho + \Delta\rho)$ by the corresponding graphs. A first approximation of the law is given by the equation

$$\frac{u - U/2}{u_*} = \frac{1}{0.45} \ln \left[\frac{u_*(y - y_0)}{\nu}\right] + 0.08 \qquad (7.18)$$

for the zone δu and by the equation

$$\frac{u - U/2}{u_*} = -\frac{1}{0.24} \ln \left[\frac{u_*(y_0 - y)}{\nu}\right] + 4.04 \qquad (7.19)$$

for the zone δu_1. The described laws define completely the dimensionless velocity distribution in the shear flow region around the interface of an arrested saline wedge.

APPENDIX

APPENDIX

When the theoretical analysis of section 3.3 is applied to the calculation of interfacial and bed shear stresses, the average velocity of the upper layer, $\overline{V_1}$, and its second power, $\overline{V_1^2}$, over the length of the arrested saline wedge must be taken from the following equations:

$$\overline{V_1} = \frac{1}{L}\int_{-L}^{0} V_1 dx = I_6 V_0 \tag{A.1}$$

and

$$\overline{V_1^2} = \frac{1}{L}\int_{-L}^{0} V_1^2 dx = I_5 V_0^2 \tag{A.2}$$

where

$$I_6 = \frac{5[12(Fr_0')^2 \ln (Fr_0')^{2/3} + 1 + 8(Fr_0')^2 - 9(Fr_0')^{8/3}]}{3[1 - (Fr_0')^{2/3}]^3 \cdot [6(Fr_0')^{4/3} + 3(Fr_0')^{2/3} + 1]}$$

and

$$I_5 = \frac{10[1 - 9(Fr_0')^{4/3} + 8(Fr_0')^2 - 4(Fr_0')^2 \ln (Fr_0')]}{3[1 - (Fr_0')^{2/3}]^3 \cdot [6(Fr_0')^{4/3} + 3(Fr_0')^{2/3} + 1]}$$

Figures A.1 to A.5 give the dimensional velocity and density distribution for some experiments of group 5 (Table 1), where characteristic

quantities of the pertinent parameters are defined. The data of these figures are summarized in Table 4. Each page of the table corresponds to one experiment which is numbered in column 1. In this table the calculated maximum value of the sum $\tau_{iv} + \tau_{it}$, where τ_{iv} are the viscous stresses and τ_{it} the Reynolds stresses, is tabulated. The interfacial coefficient, f_i, is calculated from $(\tau_{iv} + \tau_{it})_{max}$ [Equation (6.4.8)] and its value is tabulated in column 26 of Table 2.

In the graphs of Figures A.6 to A.19 the white circles correspond to experimental points and the black circles to interpolated points obtained from Figures A.1 to A.5. From Figures A.5 to A.12, the coefficients a_2, a_3, b_2, and b_3, of Equations (6.4.3) and (6.4.4), were calculated and tabulated in Table 3. In the same way, the coefficients k_2, k_3, c_2, and c_3 of Equations (6.5.2) and (6.5.3) were calculated and tabulated in Table 3.

Table 4. Geometrical and flow parameters of each experiment

Experim.	Depth	u	$\frac{y_o-y}{\varepsilon}$	$\frac{u}{U}$	$(u-\frac{U}{2})/u_*$	$\frac{u_*(y_o-y)}{\nu}$	
	cm	cm/sec					
1	2	3	4	5	6	7	8
±Δ S$_1$,	¤ 1.95	0.700	0.194	0.121	-9.13	19.52	$\frac{y_o-y}{\varepsilon}$ = 0.031
	2.00	0.850	0.181	0.147	-8.51	18.22	
h_s=2.57	2.10	1.120	0.153	0.193	-7.39	15.40	$\frac{-\overline{uv}}{u_{*o}^2}$ = 0.21
η=0.09	2.15	1.220	0.140	0.210	-6.97	14.07	
	2.20	1.380	0.126	0.238	-6.31	12.62	$\frac{du}{dy}$ = 5.844
h_s+η=2.66	* 2.25	1.683	0.112	0.290	-5.05	11.28	
δu=4.59	2.30	1.720	0.099	0.297	-4.90	9.96	u_*^2 = 0.0646
ε=3.65	2.35	1.850	0.085	0.319	-4.36	8.59	
	2.40	2.000	0.071	0.345	-3.73	7.14	
$y_o=h_s+\eta$	2.45	2.200	0.058	0.379	-2.90	5.80	$\frac{y_o-y}{\varepsilon}$ = 0.102
	2.50	2.330	0.044	0.402	-2.37	4.45	
U=5.80	2.55	2.500	0.030	0.431	-1.66	3.00	$\frac{-\overline{uv}}{u_{*o}^2}$ = 0.20
V_1=5.23			$\frac{y-y_o}{\delta u}$			$\frac{u_*(y-y_o)}{\nu}$	
ν=0.00874							$\frac{du}{dy}$ = 4.504
	2.85	3.580	0.041	0.617	2.82	5.13	
$ReFr^2$=83.2	2.90	3.700	0.052	0.638	3.32	6.56	u_*^2 = 0.0523
$\frac{\Delta\rho}{\rho+\Delta\rho}$=24.0‰	3.00	3.950	0.074	0.681	4.36	9.36	
	* 3.05	4.081	0.085	0.704	4.90	10.76	$\frac{y-y_o}{\delta u}$ = 0.040
	3.10	4.120	0.096	0.710	5.06	12.18	
	3.20	4.280	0.118	0.738	5.73	14.94	$\frac{-\overline{uv}}{u_{*o}^2}$ = 0.29
u_{*max}^2=	3.30	4.400	0.139	0.759	6.22	17.57	
=0.0646	* 3.35	4.503	0.150	0.776	6.65	19.00	$\frac{du}{dy}$ = 3.840
u_*^2=0.254	3.40	4.520	0.161	0.779	6.72	20.93	
	3.50	4.600	0.183	0.793	7.05	23.19	u_*^2 = 0.0522
f_i=0.0189	3.70	4.710	0.227	0.814	7.51	28.71	
	4.00	4.900	0.292	0.845	8.30	36.96	u_{*o}^2 = 0.0646
±±f_{ig}=0.0168	* 4.45	5.080	0.390	0.876	9.05	49.36	
±±u_{*g}=0.240	4.50	5.120	0.401	0.883	9.21	50.72	
	5.00	5.220	0.510	0.900	9.63	64.59	
	5.50	5.320	0.619	0.917	10.04	78.36	
	* 5.95	5.295	0.717	0.913	9.94	90.70	
	6.00	5.400	0.728	0.931	10.37	92.13	
	6.50	5.500	0.837	0.948	10.79	105.93	
	7.00	5.580	0.946	0.962	11.12	119.73	
	* 7.45	5.468	1.044	0.943	10.66	132.14	
	7.50	5.670	1.054	0.978	11.49	133.40	
	* 9.68	5.853	1.530	1.009	12.25	193.64	

± Symbol of the experiment

¤ Measured quantities

±± f_{ig} value of f_i from the graph and u_{*g} value of u_* from f_{ig}

Table 4—Continued

1	2	3	4	5	6	7	8
▲ S_2:	* 1.48	0.469	0.206	0.099	-9.25	24.78	
	1.60	0.500	0.182	0.105	-9.10	21.90	
	1.70	0.620	0.161	0.131	-8.52	19.37	$\frac{y_o-y}{\epsilon} = 0.048$
h_s=2.03	1.80	0.750	0.141	0.158	-7.89	16.96	
η=0.46	* 1.88	0.695	0.124	0.146	-8.16	14.92	$\frac{-\overline{uv}}{u_{*o}^2} = 0.23$
	1.95	0.950	0.110	0.200	-6.92	13.23	
h_s+η=2.49	2.00	1.050	0.100	0.221	-6.43	12.03	$\frac{du}{dy} = 3.506$
δu=5.91	2.10	1.200	0.080	0.253	-5.70	9.62	
ε=4.9	2.15	1.350	0.069	0.284	-4.98	8.30	$u_*^2 = 0.0386$
y_o=h_s+η	2.20	1.450	0.059	0.305	-4.49	7.10	
	* 2.28	1.699	0.043	0.358	-3.28	5.17	
U=4.75			$\frac{y-y_o}{\delta u}$			$\frac{u_*(y-y_o)}{\nu}$	$\frac{y-y_o}{\delta u} = 0.040$
V_1=4.25	2.70	3.250	0.035	0.684	4.25	5.08	
ν=0.00839	* 2.78	3.476	0.049	0.731	5.34	7.11	$\frac{-\overline{uv}}{u_{*o}^2} = 0.29$
$ReFr^2$=62.6	2.80	3.520	0.052	0.741	5.56	7.55	
	2.90	3.730	0.069	0.785	6.58	10.01	$\frac{du}{dy} = 2.730$
$\frac{\Delta\rho}{\rho+\Delta\rho}$=24.1%.	3.00	3.880	0.086	0.817	7.31	12.48	$u_*^2 = 0.0347$
	3.10	3.970	0.102	0.836	7.74	14.80	
	3.20	4.040	0.120	0.851	8.08	17.41	
	* 3.28	4.145	0.132	0.872	8.59	19.15	
	3.30	4.090	0.135	0.861	8.33	19.59	$u_{*o}^2 = 0.0403$
u_{max}^2=	3.40	4.130	0.152	0.869	8.52	22.06	
=0.0403	3.60	4.180	0.186	0.880	8.76	26.99	
u_*=0.201	3.80	4.200	0.220	0.885	8.86	31.92	
	4.00	4.220	0.253	0.887	8.96	36.71	
f_1=0.0178	* 4.48	4.298	0.333	0.905	9.33	48.32	
	4.60	4.300	0.354	0.905	9.34	51.37	
	5.00	4.340	0.421	0.913	9.54	61.09	
$f_{1\delta}$=0.0190	5.40	4.390	0.488	0.925	9.78	70.81	
$u_{*\delta}$=0.207	* 5.98	4.414	0.585	0.930	9.90	84.89	
	6.40	4.470	0.656	0.941	10.17	95.19	
	* 6.98	4.511	0.754	0.949	10.37	109.41	
	7.40	4.560	0.823	0.960	10.61	119.42	
	8.00	4.600	0.924	0.968	10.80	134.08	
	* 8.48	4.733	1.004	0.997	11.45	145.69	
	9.00	4.660	1.092	0.981	11.09	158.46	

Table 4—Continued

1	2	3	4	5	6	7	8
▲ S_4	* 1.92	0.486	0.234	0.092	-10.30	29.25	
	2.00	0.450	0.218	0.085	-10.48	27.25	$\frac{y_o-y}{c}$ = 0.048
	* 2.12	0.478	0.194	0.090	-10.34	24.25	
h_s=2.60	2.20	0.660	0.178	0.125	- 9.48	22.25	$\frac{-\overline{uv}}{u_{*o}^2}$ = 0.23
η=0.49	2.30	0.820	0.158	0.155	- 8.71	19.75	
h_s+η=3.09	2.40	0.920	0.138	0.174	- 8.24	17.25	$\frac{du}{dy}$ = 4.179
δu=7.93	* 2.52	0.896	0.114	0.169	- 8.35	14.25	
ε=5.00	2.60	1.300	0.098	0.245	- 6.43	12.25	u_{*o}^2 = 0.0440
y_o=h_s+η	2.70	1.480	0.078	0.279	- 5.57	9.75	
	2.75	1.600	0.068	0.302	- 5.00	8.50	
	* 2.82	1.946	0.054	0.367	- 3.35	6.75	$\frac{y-y_o}{\delta u}$ = 0.023
	2.85	1.950	0.048	0.368	- 3.33	6.00	
U=5.30			$\frac{y-y_o}{\delta u}$			$\frac{u_*(y-y_o)}{\nu}$	$\frac{-\overline{uv}}{u_{*o}^2}$ = 0.20
V_1=4.88							
ν=0.00840	3.30	3.200	0.027	0.604	2.62	5.35	$\frac{du}{dy}$ = 4.315
$ReFr^2$=133.5	3.40	3.460	0.039	0.653	3.86	7.73	
	3.50	3.650	0.052	0.689	4.76	10.31	u_{*o}^2 = 0.0440
$\frac{\Delta\rho}{\rho+\Delta\rho}$=23.8%	* 3.62	3.951	0.067	0.745	6.20	13.28	
	3.70	3.960	0.077	0.744	6.24	15.27	
	3.80	4.100	0.090	0.774	6.90	17.84	u_{*o}^2 = 0.0388
	4.00	4.350	0.115	0.821	8.10	22.80	
u_*^2max=	4.20	4.480	0.140	0.845	8.71	27.76	
=0.0440	4.30	4.540	0.153	0.857	9.00	30.33	
u_*=0.210	* 4.42	4.574	0.168	0.863	9.16	33.31	
f_1=0.0148	4.60	4.650	0.190	0.877	9.52	37.67	
	5.00	4.730	0.241	0.892	9.90	47.78	
	5.50	4.820	0.304	0.909	10.33	60.27	
	6.00	4.890	0.367	0.923	10.67	72.76	
f_{1g}=0.0143	6.50	4.960	0.430	0.936	11.00	85.25	
u_{*g}= 0.206	* 6.92	4.960	0.483	0.936	11.00	95.75	
	7.50	5.040	0.556	0.950	11.38	110.23	
	8.50	5.090	0.682	0.960	11.62	135.21	
	9.50	5.120	0.808	0.968	11.76	160.19	
	10.50	5.160	0.934	0.974	11.95	185.17	
	11.50	5.200	1.061	0.981	12.14	210.34	
	*12.42	5.167	1.177	0.975	11.99	233.34	
	*19.17	5.296	2.028	0.999	12.60		

Table 4—Continued

1	2	3	4	5	6	7	8
▲ U_q:	* 1.42	0.577	0.254	0.135	-7.97	24.37	$\frac{y_o-y}{\varepsilon} = 0.045$
	1.50	0.450	0.236	0.105	-8.62	22.64	
	1.60	0.550	0.212	0.129	-8.11	20.34	$\frac{-\overline{uv}}{u_{*o}^2} = 0.23$
h_s=2.35	1.70	0.650	0.188	0.152	-7.60	18.04	
η=0.14	* 1.82	0.713	0.160	0.167	-7.28	15.35	
$h_s+\eta$=2.49	1.90	0.840	0.140	0.196	-6.63	13.43	$\frac{du}{dy} = 3.510$
δu=6.93	2.00	0.950	0.117	0.222	-6.07	11.23	
ε=4.20	2.05	1.030	0.105	0.241	-5.66	10.07	$u_*^2 = 0.0378$
$y_o=h_s+\eta$	2.10	1.100	0.093	0.257	-5.31	8.92	
	* 2.12	1.087	0.088	0.254	-5.37	8.44	
	2.20	1.350	0.069	0.315	-4.03	6.62	
	2.25	1.470	0.057	0.343	-3.42	5.47	$\frac{y-y_o}{\delta u} = 0.023$
U=4.28	2.30	1.620	0.045	0.378	-2.65	4.32	
V_1=3.78							$\frac{-\overline{uv}}{u_{*o}^2} = 0.20$
v=0.00858			$\frac{y-y_o}{\delta u}$			$\frac{u_*(y-y_o)}{v}$	
$ReFr^2$=44.4	2.60	2.500	0.016	0.584	1.84	2.53	$\frac{du}{dy} = 2.511$
	2.70	2.720	0.030	0.636	2.96	4.75	
$\frac{\Delta\rho}{\rho+\Delta\rho}$=25.1%	* 2.72	2.767	0.033	0.646	3.20	5.22	$u_*^2 = 0.0282$
	2.80	2.850	0.045	0.666	3.62	7.12	
	2.90	2.950	0.059	0.689	4.13	9.34	
	3.00	3.030	0.074	0.708	4.54	11.71	$u_{*o}^2 = 0.0329$
u_*max=0.0378	3.15	3.170	0.095	0.749	5.26	15.04	
u_*=0.194	3.30	3.270	0.117	0.764	5.77	18.52	
	3.50	3.380	0.146	0.790	6.33	23.11	
f_1=0.0212	3.70	3.450	0.174	0.806	6.68	27.54	
	3.90	3.500	0.203	0.818	6.94	32.14	
	4.00	3.520	0.220	0.822	7.04	34.83	
f_g=0.0220	* 4.22	3.633	0.250	0.849	7.62	39.58	
u_*=0.198	4.50	3.630	0.290	0.848	7.60	45.91	
	5.00	3.710	0.362	0.867	8.01	57.31	
	5.50	3.760	0.433	0.879	8.27	68.54	
	6.00	3.820	0.506	0.893	8.57	80.10	
	7.00	3.940	0.651	0.921	9.18	103.53	
	* 7.22	3.965	0.682	0.926	9.31	107.97	
	8.00	4.050	0.795	0.946	9.74	125.85	
	9.00	4.150	0.940	0.970	10.26	148.81	
	* 9.48	4.174	1.012	0.975	10.38	160.21	

Table 4—Continued

1	2	3	4	5	6	7	8
Φ U_5:	* 1.56	0.569	0.192	0.160	-6.55	19.04	$\frac{y_o-y}{\varepsilon} = 0.028$
	1.60	0.520	0.183	0.146	-6.81	18.15	
	1.70	0.650	0.161	0.183	-6.11	15.97	
h_s=2.02	1.75	0.720	0.150	0.202	-5.73	14.88	$\frac{-\overline{uv}}{u^2_{*o}} = 0.20$
n= 0.42	1.80	0.750	0.139	0.211	-5.57	13.79	
h_s+n=2.44	* 1.86	0.614	0.126	0.172	-6.30	12.50	$\frac{du}{dy} = 3.480$
δu=5.91	1.90	0.850	0.117	0.239	-5.03	11.60	
ε=4.60	1.95	0.920	0.107	0.258	-4.65	10.61	$u^2_* = 0.0356$
y_o=h_s+n	2.00	1.020	0.096	0.287	-4.11	9.52	
	2.05	1.070	0.085	0.301	-3.84	8.43	
	2.10	1.150	0.074	0.323	-3.41	7.34	
	* 2.16	1.223	0.060	0.344	-3.01	5.95	$\frac{y-y_o}{\delta u} = 0.023$
	2.20	1.350	0.052	0.379	-2.32	5.16	
u=3.56	2.25	1.430	0.041	0.402	-1.89	4.07	$\frac{-\overline{uv}}{u^2_{*o}} = 0.20$
V_1=3.08	2.30	1.520	0.030	0.427	-1.41	2.98	
v=0.00858			$\frac{y-y_o}{\varepsilon}$			$\frac{u_*(y-y_o)}{\nu}$	$\frac{du}{dy} = 2.620$
$ReFr^2$=28.7							$u^2_* = 0.0263$
$\frac{\Delta\rho}{\rho+\Delta\rho}$=23.5%	2.55	2.120	0.019	0.596	1.84	2.42	
	2.60	2.220	0.027	0.624	2.38	3.44	
	2.70	2.400	0.044	0.674	3.35	5.61	
	2.80	2.520	0.061	0.708	4.00	7.77	$u^2_{*o} = 0.0290$
	* 2.86	2.611	0.071	0.733	4.49	9.05	
u_*max=0.0356	2.90	2.620	0.078	0.736	4.54	9.94	
u_*=0.189	3.00	2.690	0.095	0.756	4.92	12.11	
f_i=0.031	3.20	2.800	0.129	0.786	5.51	16.44	
	3.40	2.860	0.162	0.803	5.84	20.64	
	3.60	2.920	0.196	0.820	6.16	24.98	
	3.80	2.950	0.230	0.829	6.32	29.31	
f_{i_B}=0.0275	* 3.86	2.952	0.240	0.829	6.34	30.58	
	4.00	2.990	0.264	0.840	6.54	33.64	
u_{*_B}=0.181	4.50	3.070	0.349	0.862	6.97	44.47	
	5.00	3.130	0.433	0.879	7.30	55.17	
	5.50	3.200	0.518	0.899	7.68	66.01	
	6.00	3.230	0.602	0.907	7.84	76.71	
	* 6.36	3.257	0.663	0.915	7.98	84.49	
	7.00	3.320	0.772	0.933	8.32	98.38	
	8.00	3.380	0.941	0.949	8.65	119.91	
	9.00	3.460	1.110	0.972	9.08	141.45	
	* 9.56	3.534	1.205	0.993	9.48	153.55	

Table 4—Continued

1	2	3	4	5	6	7	8
↑ AA_1:	* 2,29	1,059	0,209	0,129	-11,02	36,97	$\frac{y_0-y}{\varepsilon}=0.048$
	2,40	0,900	0,189	0,110	-11,59	33,43	
	2,50	5,000	0,171	0,122	-11,23	30,25	$\frac{-\overline{uv}}{u_{*0}^2}=0.23$
h_s=3.17	2,60	1,200	0,153	0,146	-11,51	27,06	
η=0.28	* 2,69	1,418	0,137	0,173	- 9,72	24,23	
	2,80	1,700	0,117	0,207	- 9,70	20,70	$\frac{du}{dy}=6.094$
h_s+η=3.45	2,85	1,850	0,108	0,226	- 8,15	19,10	
δu=8.25	* 2,89	1,762	0,100	0,215	- 8,47	17,69	u_*^2=0.0690
ε=5.55	2,95	2,200	0,090	0,268	- 6,88	15,91	
	3,00	2,400	0,081	0,293	- 6,16	14,32	
y_0=h_s+η	3,05	2,550	0,072	0,310	- 5,62	12,74	
	3,10	2,800	0,063	0,341	- 4,71	11,14	$\frac{y-y_0}{\delta u}=0.040$
	* 3,19	3,363	0,046	0,410	- 2,67	8,14	
U=8.20	3,15	3,050	0,054	0,372	- 3,80	9,55	$\frac{-\overline{uv}}{u_{*0}^2}=0.29$
V_1=7.96	3,20	3,300	0,045	0,402	- 2,90	7,96	
							$\frac{du}{dy}=3.13$
v=0.00866			$\frac{y-y_0}{\delta u}$			$\frac{u_*(y-y_0)}{v}$	$u_*^2=0.0478$
$ReFr^2$=527.1	3,80	5,250	0,042	0,640	4,17	11,04	
$\frac{\Delta\rho}{\rho+\Delta\rho}$=23.9%	* 3,99	5,542	0,065	0,676	5,22	17,09	
	4,20	5,850	0,091	0,713	6,34	23,93	$u_{*0}^2=0.0705$
	4,40	6,100	0,115	0,744	7,25	30,24	
	4,80	6,500	0,164	0,793	8,70	43,12	
	5,00	6,650	0,188	0,811	9,24	49,43	
u_{*max}^2=0.0705	5,20	6,820	0,212	0,832	9,86	55,74	
u_*=0.266	5,49	7,020	0,247	0,856	10,58	64,94	
f_i=0.0089	5,60	7,100	0,261	0,866	10,87	68,63	
	6,00	7,300	0,309	0,890	11,59	81,25	
	6,40	7,480	0,358	0,910	12,25	94,13	
f_{ig}=0.0092	6,80	7,600	0,406	0,927	12,68	106,75	
	7,20	7,720	0,455	0,941	13,12	119,63	
u_{*g}=0.270	7,60	7,830	0,503	0,955	13,51	132,25	
	* 7,99	7,951	0,550	0,970	13,95	144,61	
	8,80	7,960	0,648	0,971	13,99	170,38	
	9,60	8,020	0,745	0,978	14,20	195,89	
	10,40	8,040	0,842	0,980	14,28	221,43	
	*29,39	8,181	3,144	0,998			

Table 4—Continued

1	2	3	4	5	6	7	8
Δ AA_2:	2,10	0,450	0,180	0,055	-13,27	36,55	$\frac{y_o-y}{\varepsilon}$ = 0,027
	2,20	0,680	0,164	0,083	-12,44	33,30	
	2,30	0,900	0,148	0,110	-11,64	30,05	$\frac{-\overline{uv}}{u_{*0}^2}$ = 0,19
h_s=3,00	*2,36	1,190	0,139	0,145	-10,58	28,22	
	2,40	1,100	0,132	0,134	-10,91	26,80	
n=0,24	2,50	1,400	0,117	0,171	- 9,82	23,76	$\frac{du}{dy}$ = 7,700
h_s+n=3,24	2,60	1,700	0,101	0,207	- 8,73	20,51	
δu=7,46	2,70	2,000	0,085	0,214	- 7,64	17,26	u_*^2 = 0,0799
ε=6,35	*2,76	2,127	0,076	0,259	- 7,17	15,43	
	2,80	2,350	0,069	0,287	- 6,36	14,81	
$y_o=h_s+\eta$	2,90	2,650	0,054	0,323	- 5,27	10,96	$\frac{y-y_o}{\delta u}$ = 0,040
	*2,96	2,848	0,045	0,347	- 4,55	9,14	
	3,00	3,080	0,038	0,376	- 3,71	7,72	$\frac{-\overline{uv}}{u_{*0}^2}$ = 0,29
U=8,20	3,05	3,300	0,030	0,402	- 2,91	6,09	
V_1=7,95			$\frac{y-y_o}{\delta u}$			$\frac{u_*(y-y_o)}{\nu}$	$\frac{du}{dy}$ = 3,446
ν=0,00860							
$Refr^2$=518,6	3,50	4,900	0,035	0,598	2,91	8,35	u_*^2 = 0,0508
	3,60	5,150	0,048	0,628	3,82	11,45	
$\frac{\Delta\rho}{\rho+\Delta\rho}$=23,4‰	*3,86	5,660	0,083	0,690	5,67	19,80	
	4,00	5,850	0,102	0,713	6,36	24,33	u_{*0}^2 = 0,0730
	4,40	6,250	0,155	0,762	7,82	36,97	
	4,80	6,650	0,209	0,811	9,27	49,86	
u_*^2max=0,0799	5,20	6,900	0,263	0,841	10,18	62,74	
	5,60	7,180	0,316	0,876	11,20	75,38	
u_*= 0,283	*5,85	7,326	0,351	0,893	11,73	83,73	
f_1=0,0101	7,20	7,700	0,531	0,940	13,09	126,67	
	8,00	7,900	0,638	0,963	13,82	152,19	
	8,80	8,000	0,745	0,976	14,18	177,72	
	*9,36	8,171	0,820	0,996	14,80	195,61	
f_{1g}=0,0093	9,60	8,020	0,853	0,978	14,25	203,48	
	10,40	8,030	0,960	0,979	14,29	229,0	
u_{*g}=0,271	*29,86	8,000	0,570	0,977	14,18		

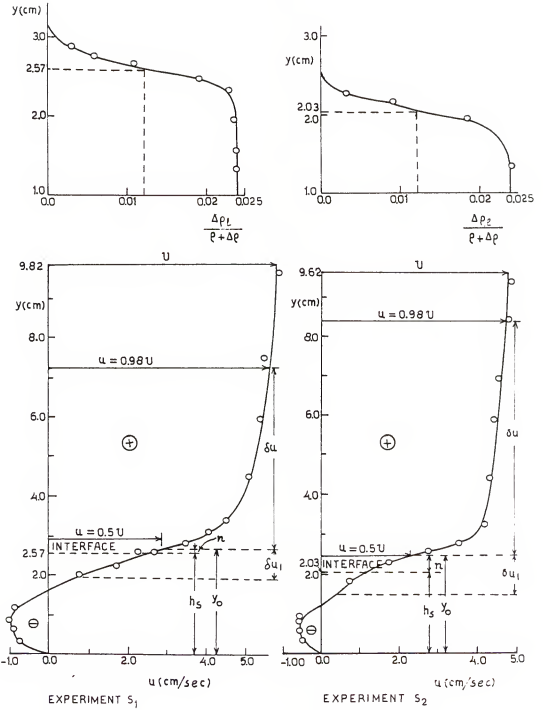

Figure A.1 Dimensional velocity distribution (experiments S_1 and S_2)

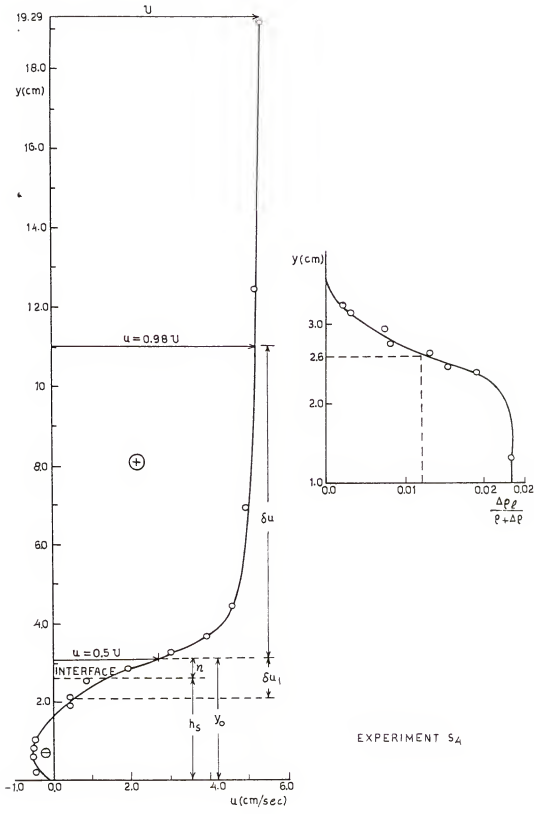

Figure A.2 Dimensional velocity distribution (experiment S_4)

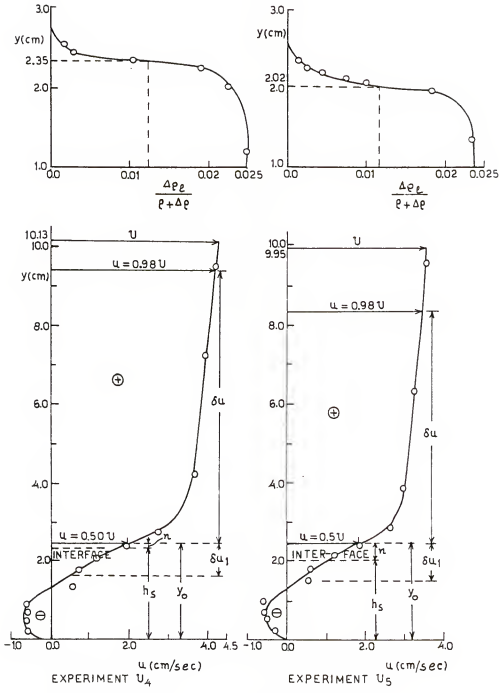

Figure A.3 Dimensional velocity distribution (experiments U_4 and U_5)

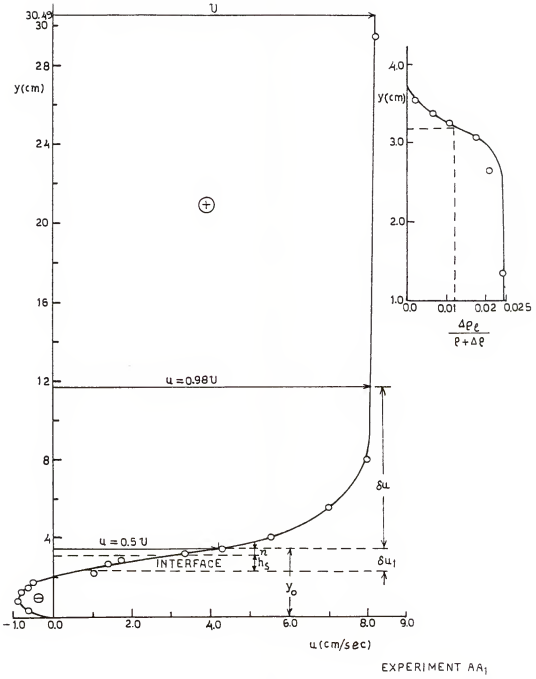

Figure A.4. Dimensional velocity distribution (experiment AA_1)

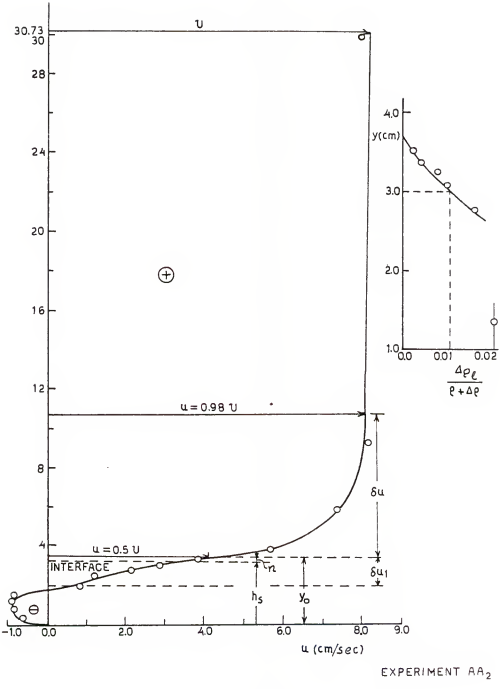

Figure A.5 Dimensional velocity distribution (experiment AA_2)

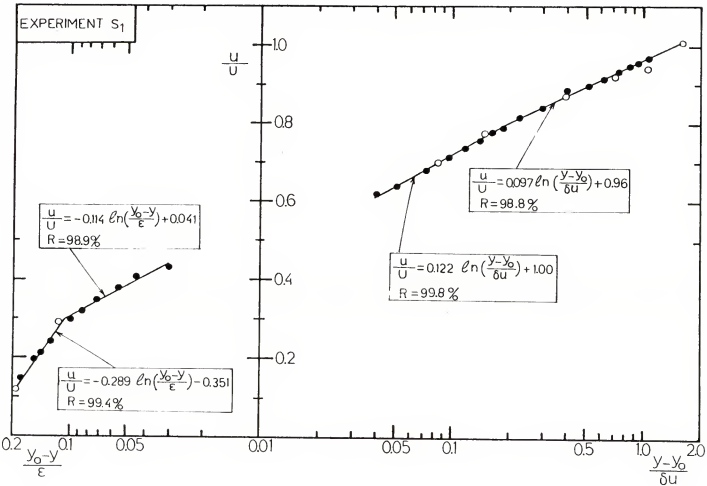

Figure A.6 Dimensionless velocity distribution outside of the linear zone (experiment S_1)

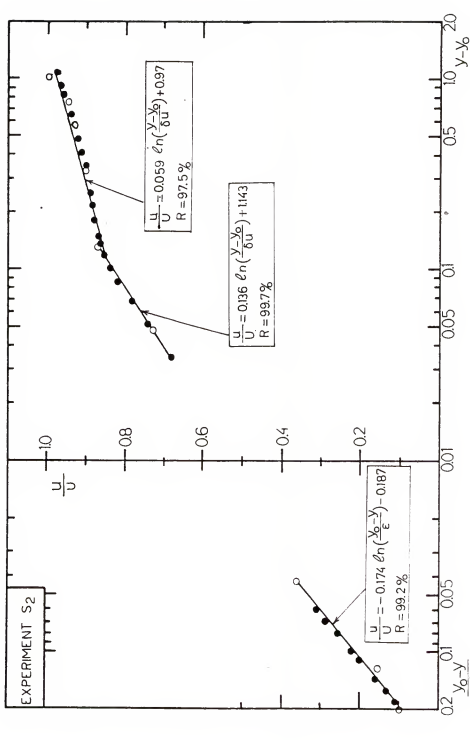

Figure A.7 Dimensionless velocity distribution outside of the linear zone (experiment S_2)

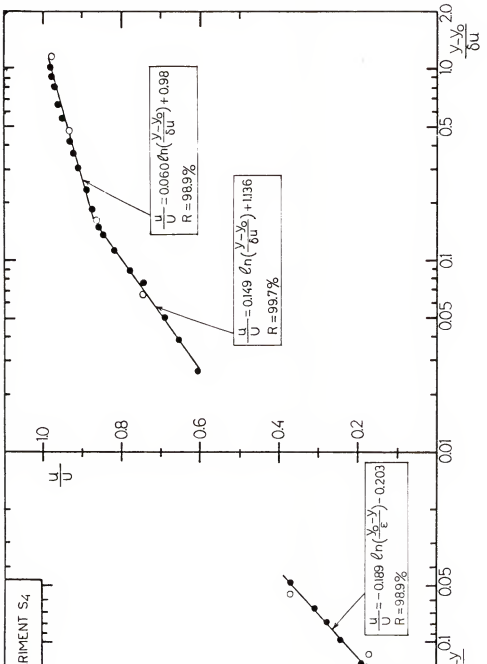

Figure A.8 Dimensionless velocity distribution outside of the linear zone (experiment S_4)

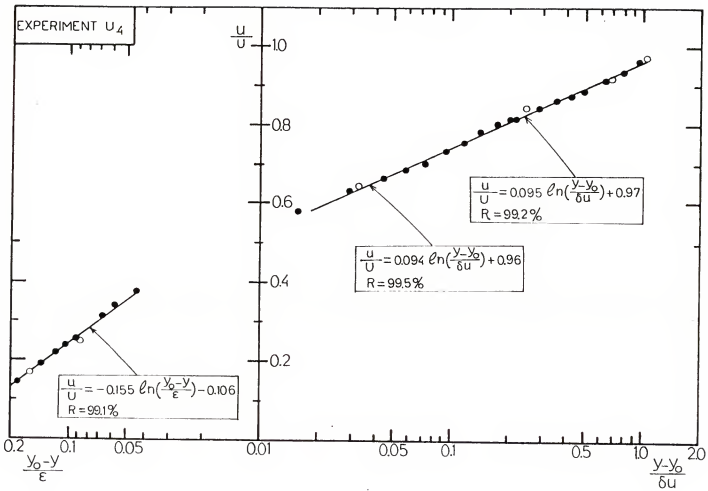

Figure A.9 Dimensionless velocity distribution outside of the linear zone (experiment U_4)

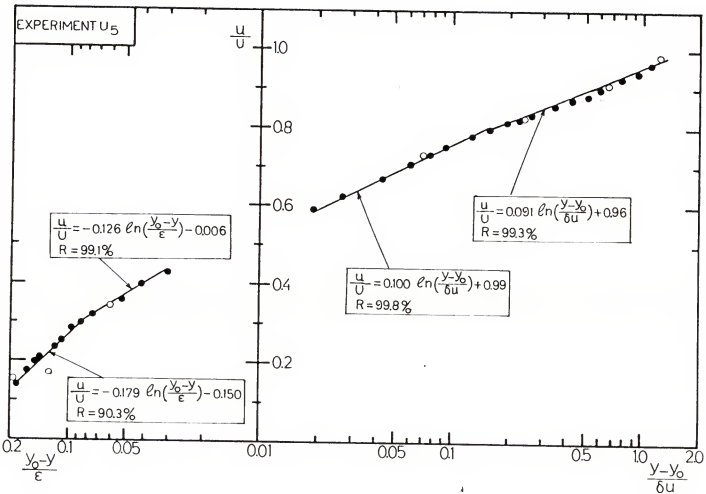

Figure A.10 Dimensionless velocity distribution outside of the linear zone (experiment U_5)

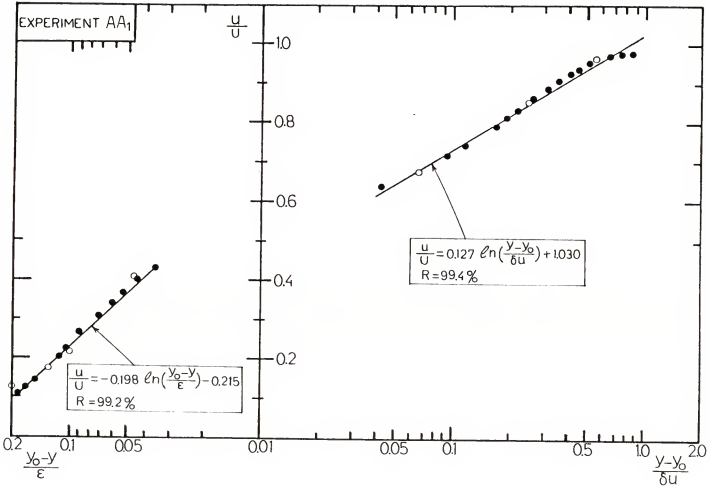

Figure A.11 Dimensionless velocity distribution outside of the linear zone (experiment AA_1)

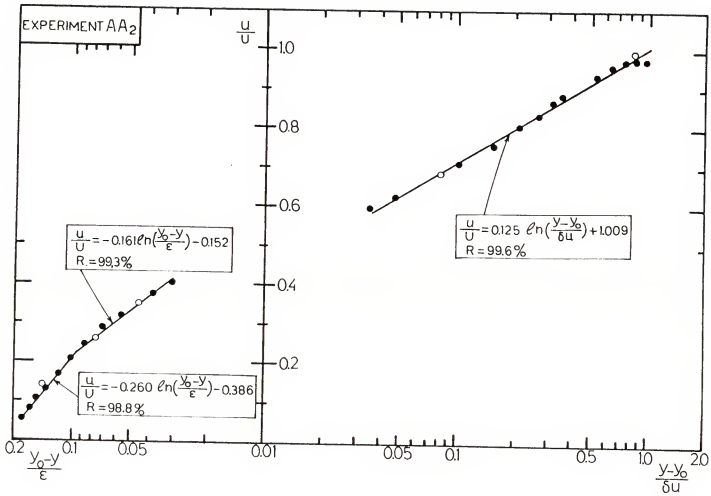

Figure A.12 Dimensionless velocity distribution outside of the linear zone (experiment AA_2)

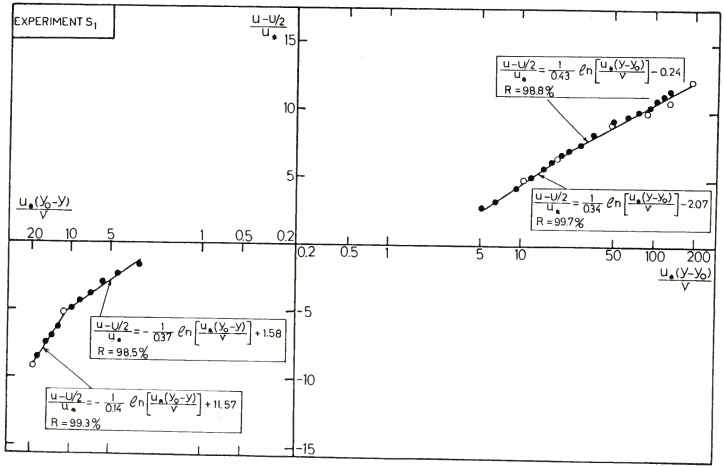

Figure A.13 Dimensionless velocity distribution outside of the linear zone (experiment S_1)

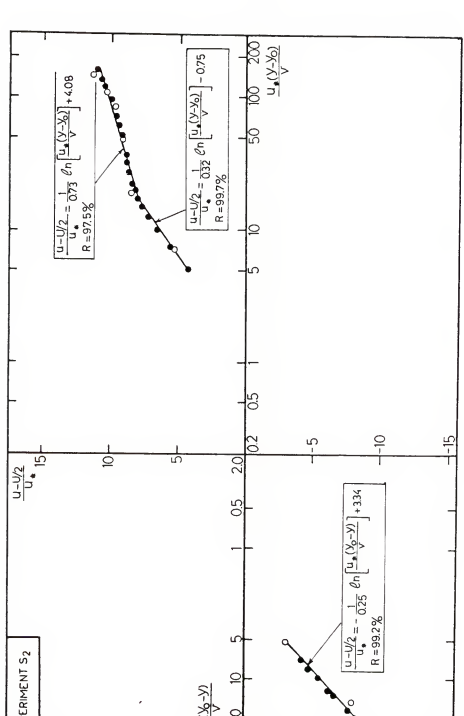

Figure A.14 Dimensionless velocity distribution outside of the linear zone (experiment S_2)

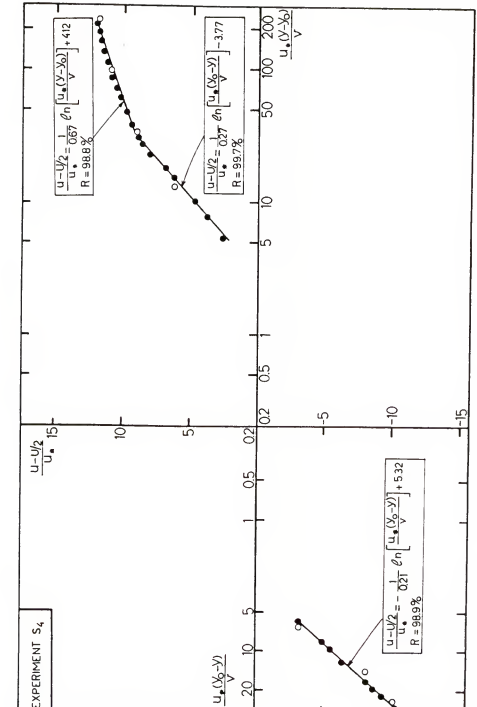

Figure A.15 Dimensionless velocity distribution outside of the linear zone (experiment S_4)

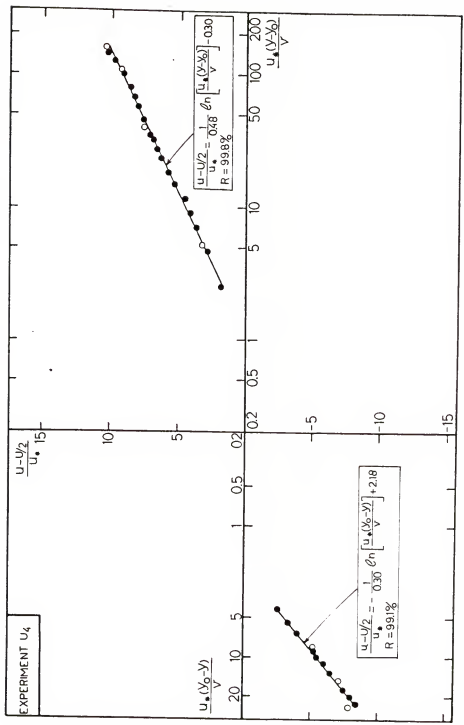

Figure A.16 Dimensionless velocity distribution outside of the linear zone (experiment U_4)

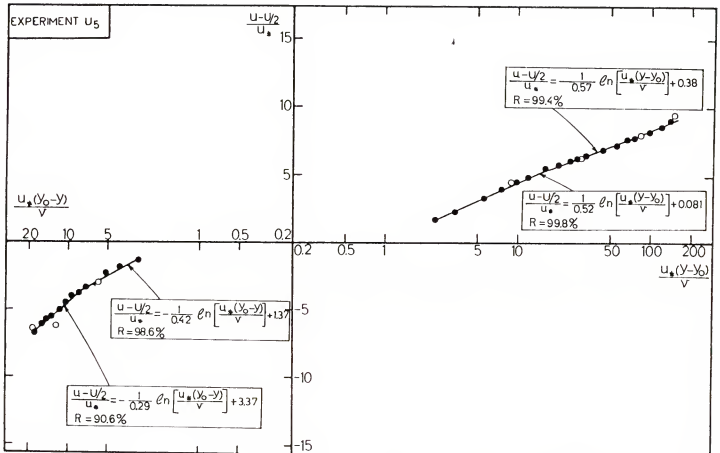

Figure A.17 Dimensionless velocity distribution outside of the linear zone (experiment U_5)

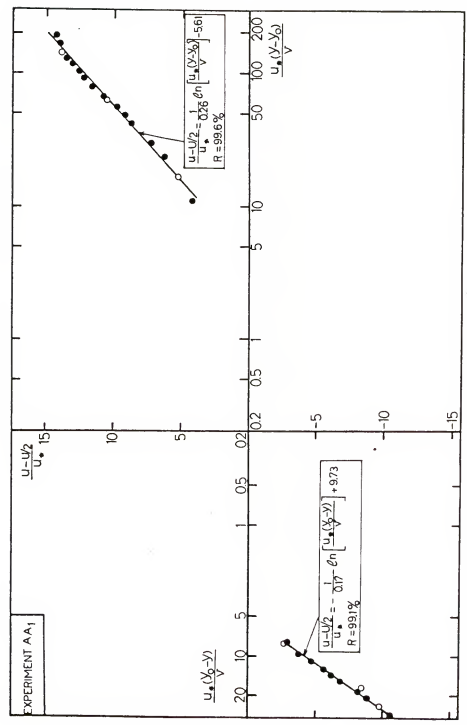

Figure A.18 Dimensionless velocity distribution outside of the linear zone (experiment AA_1)

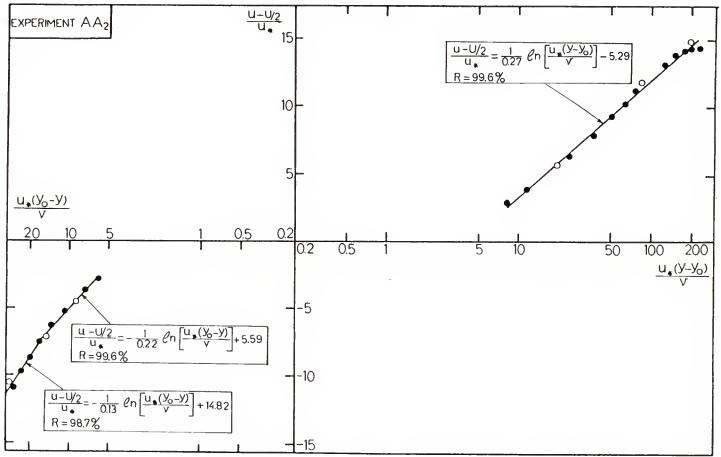

Figure A.19 Dimensionless velocity distribution outside of the linear zone (experiment AA_2)

REFERENCES

1. Abraham, G., and Eysink, W. D., "Magnitude of Interfacial Shear in Exchange Flow," J. of Hydr. Res., I.A.H.R., Vol. 9, No. 2, 1971, pp. 125-151.

2. Abraham, G., Karelse, M., and van Os, A. G., "On the Magnitude of Interfacial Shear of Subcritical Stratified Flows in Relation with Interfacial Stability," J. of Hydr. Res., I.A.H.R., Vol. 17, No. 4, 1979, pp. 273-286.

3. Anisimova, E. P., and Speranskaya, A. A., "Turbulence in Stratified Flows," Proc., International Symposium on Stratified Flows, Novosibirsk, U.S.S.R., 1972, pp. 473-481.

4. Averkiev, A. G., and Kind, K. J., "Etudes Experimentales de Certaines Characteristiques des Courants de Densité," A.I.R.H. Congres, Leningrad, U.S.S.R., 1965, pp. 1-13.

5. Barr, D. I. A., "Densimetric Exchange Flow in Rectangular Channels, I: Definitions, Review, and Relevance to Model Design; II: Some Observations of the Structure of Lock Exchange Flow," La Houille Blanche, No. 7, 1963, pp. 739-766.

6. Barr, D. I. A., "Densimetric Exchange Flow in Rectangular Channels, III: Large Scale Experiments," La Houille Blanche, No. 6, 1967, pp. 619-633.

7. Bata, G. L., "Recirculation of Cooling Water in Rivers and Canals," Journal of the Hydraulics Division, A.S.C.E., Vol. 83, Proc. Paper No. 1265, 1957, pp. 1-27.

8. Bata, G. L., and Knezevich, B., "Some Observations on Density Currents in the Laboratory and in the Field," Proc., Minn. Intern. Hydr. Conv., September 1953, pp. 387-400.

9. Csanady, G. T., "Turbulent Interface Layers," Journal of Geophysical Research, Vol. 83, No. C5, 1978, pp. 2329-2342.

10. Delft Hydraulics Laboratory, "Momentum and Mass Transfer in Stratified Flows," Report on Literature Study, No. R880, Delft, The Netherlands, 1974.

11. Dermissis, V., "A Study of the Interfacial Friction Coefficient in a Two-Layered Fluid System," (in Greek), Doctoral dissertation, Aristoteles University of Thessaloniki, Greece, 1977.

12. Dermissis, V., and Partheniades, E., "Interfacial Resistance in Stratified Flows," Proc., 15th Annual Meeting of the Society of Engineering Sciences, Gainesville, Florida, 1978, pp. 387-392.

13. Georgiev, B. V., "Some Experimental Investigation on Turbulent Characteristics of Stratified Flows," Proc., International Symposium on Stratified Flows, Novosibirsk, U.S.S.R., 1972, pp. 507-515.

14. Grubert, S. P., "Experiments on Arrested Saline Wedge," Journal of the Hydraulics Division, A.S.C.E., Vol. 106, No. HY6, 1980, pp. 945-960.

15. Harleman, D. R. F., "Stratified Flows," in Handbook of Fluid Dynamics, ed. by V. L. Streeter, McGraw-Hill, New York, 1961, Chapter 26.

16. Harleman, D. R. F., and Stolzenbach, K. D., "Fluid Mechanics of Heat Disposal from Power Generation," Annual Review of Fluid Mech., Vol. 4, 1972, pp. 7-32.

17. Hino, M., Hung, N. S., and Nakamura, K. I., "Entrainment and Friction at the Interface of Salt Wedge," 2nd International Symposium on Stratified Flows, Trondheim, Norway, 1980.

18. Iwasaki, T., "On the Shear Stress at the Interface and Its Efffects in the Stratified Flow," Proc., 9th Coastal Engineering Conference, Lisbon, Portugal, 1964, pp. 879-892.

19. Iwasaki, T., and Abe, T., "Turbulence in the Weakly Mixing Zone of the Interface," Proc., International Symposium on Stratified Flows, Novosibirsk, U.S.S.R., 1972, pp. 251-259.

20. Jeffreys, H., "On the Formation of Water Waves by Wind," Proc., Roy. Soc., Ser. A., No. 110, 1926, pp. 241-247.

21. Keulegan, G. H., "Interfacial Instability and Mixing in Stratified Flows," J. Res. Nat. Bur. Stand., Vol. 43, Nov. 1949, pp. 487-500.

22. Keulegan, G. H., "Significant Stresses of Arrested Saline Wedges," Nat. Bur. Stand. Rept. No. 4267, August 1955.

23. Keulegan, G. H., "The Motion of Saline Fronts in Still Water," Nat. Bur. Stand. Rept. No. 5831, April 1958.

24. Keulegan, G. H., "The Mechanics of an Arrested Saline Wedge," in Estuary and Coastline Hydrodynamics, ed. by A. T. Ippen, McGraw-Hill, New York, 1966, Chapter 11.

25. Linden, P. F., "Mixing in Stratified Fluids," Geophys. Astrophys. Fluid Dynamics, Vol. 13, 1979, pp. 3-23.

26. Lofquist, K., "Flow and Stress Near an Interface between Stratified Liquids," The Phys. of Fluids, Vol. 3, No. 2, 1960, pp. 158-175.

27. Macagno, E. O., and Rouse, H., "Interfacial Mixing in Stratified Flows," Trans., A.S.C.E., Vol. 127, Paper No. 3289, 1962, pp. 102-127.

28. Partheniades, E., Discussion of "Salinity Intrusion Effects in Estuary Shoaling," by D. R. F. Harleman and A. T. Ippen, Journal of the Hydraulics Division, A.S.C.E., Vol. 96, No. HY1, Proc. Paper No. 6988, 1970, pp. 264-269.

29. Partheniades, E., "Salinity Intrusion in Estuaries and Its Effects on Shoaling," in River Mechanics, ed. by H. W. Schen, Vol. II, H. W. Schen, Fort Collins, Colorado, 1971, Chapter 26.

30. Partheniades, E., and Dermissis, V., "Interfacial Friction Coefficient in a Two-Layered Stratified Flow," Proc., 16th Coastal Engineering Conference, Hamburg, Germany, Vol. 3, Ch. 170, 1978, pp. 2778-2797.

31. Partheniades, E., Dermissis, V., and Mehta, A. J., "On the Shape and Interfacial Resistance of Arrested Saline Wedges," Proc., 15th Congress of I.A.H.R., Sao Paulo, Brazil, Vol. I, 1975, pp. 157-164.

32. Plate, E., and Friedrich, R., "The Stability of an Interface in Stratified Channel Flow," Proc., 15th Congress of I.A.H.R., Sao Paulo, Brazil, Vol. II, 1975, pp. 9-21.

33. Polk, E. M., Benedict, B. A., and Parker, F. L., "Cooling Water Density Wedges in Streams," Proc., A.S.C.E., Vol. 97, No. HY10, 1971, pp. 1639-1652.

34. Powell, G. M., "The Structure of Velocity and Density Interfaces in a Weakly Turbulent Stratified Shear Flow," Doctoral dissertation, University of Florida, Gainesville, Florida, 1979.

35. Pui, N. K., and Gartshore, I. S., "Measurements of the Growth Rate and Structure in Plane Turbulent Mixing Layers," J. Fluid Mech., Vol. 91, part 1, 1979, pp. 111-130.

36. Riddell, J. F., "Densimetric Exchange Flow in Rectangular Channels, IV: The Arrested Saline Wedge," La Houille Blanche, Vol. 25, No. 4, 1971, pp. 317-330.

37. Schijf, J. B., and Schönfeld, J. C., "Theoretical Considerations on the Motion of Salt and Fresh Water," Proc., Minn. Intern. Hydr. Conv., Minneapolis, Minnesota, 1953, pp. 321-333.

38. Sheppard, D. M., and Doddington, H. W., "Laboratory Instrument for Measuring Electrical Conductivity in Stratified NaCl Solutions," Rev. Sci. Instrum., Vol. 48, No. 3, 1977, pp. 287-289.

39. Sherenkov, I. A., Netjukhailo, A. P., and Telezhkin, E. D., "Research Investigation of Transfer Process in Two-Dimensional Stratified Flow," I.A.H.R. Congress, Paris, France, Paper No. A26-1, 1971, pp. 217-225.

40. Shi-Igai, H., "On the Resistance Coefficient at the Interface between Salt and Fresh Water," Trans., Japan Society of Civil Engineers, No. 123, Nov. 1965, pp. 27-31.

41. Shi-Igai, H., and Kono, T., "On the New Formula on the Shape of Saline Wedges," Tech. Paper of Dept. of Civil Engineering, Tokyo Inst. of Tech., No. 1, March 1966, pp. 14-20.

BIOGRAPHICAL SKETCH

Vassilios Dermissis was born in Trikala, Greece, in February 1942. In 1959, after high-school graduation in Trikala, he was accepted and registered as an undergraduate student at the University of Athens, Greece, at the Department of Physics and Mathematics. In 1964 he graduated from the aforementioned university with a degree in mathematics. For the next two years he served in the Greek Army as an officer. After that, he taught mathematics at a high school. In 1967, he was admitted and registered for 1968 at the University of Thessaloniki, Greece, in the Civil Engineering Department of the School of Engineering. In 1972, he graduated with a degree in civil engineering. During his studies at the University of Thessaloniki, he was teaching mathematics in high schools and since 1970 he had an assistantship at the University of Thessaloniki, teaching water supply and sewerage systems, open channel flow, and river mechanics. Since 1974 he started working on stratified flows and in 1978 after completion of the requirements he received his doctoral degree in civil engineering at the University of Thessaloniki, Greece, and he became a lecturer at the same university. From June 1977 to September 1979 he was a graduate research assistant at the Department of Engineering Sciences and Mechanics at the University of Florida in Gainesville, Florida. In 1982, he received the professorial (Dozent) degree in civil engineering at the

University of Thessaloniki, Greece, and in 1983 he became an assistant professor at the same university. During the last eight years he has published as an author or co-author more than a dozen papers, in both Greek and English.

He is married and they have a ten-year-old daughter.

I certify that I have read this study and that in my opinion it conforms to acceptable standards of scholarly presentation and is fully adequate, in scope and quality, as a dissertation for the degree of Doctor of Philosophy.

Emmanuel Partheniades, Chairman
Professor of Engineering Sciences

I certify that I have read this study and that in my opinion it conforms to acceptable standards of scholarly presentation and is fully adequate, in scope and quality, as a dissertation for the degree of Doctor of Philosophy.

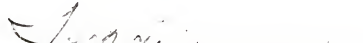

Joseph L. Hammack, Jr.
Professor of Engineering Sciences

I certify that I have read this study and that in my opinion it conforms to acceptable standards of scholarly presentation and is fully adequate, in scope and quality, as a dissertation for the degree of Doctor of Philosophy.

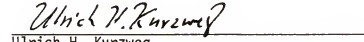

Ulrich H. Kurzweg
Professor of Engineering Sciences

I certify that I have read this study and that in my opinion it conforms to acceptable standards of scholarly presentation and is fully adequate, in scope and quality, as a dissertation for the degree of Doctor of Philosophy.

Bernard M. Leadon
Professor of Engineering Sciences

I certify that I have read this study and that in my opinion it conforms to acceptable standards of scholarly presentation and is fully adequate, in scope and quality, as a dissertation for the degree of Doctor of Philosophy.

Lawrence E. Malvern
Professor of Engineering Sciences

I certify that I have read this study and that in my opinion it conforms to acceptable standards of scholarly presentation and is fully adequate, in scope and quality, as a dissertation for the degree of Doctor of Philosophy.

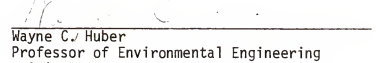

Wayne C. Huber
Professor of Environmental Engineering Sciences

I certify that I have read this study and that in my opinion it conforms to acceptable standards of scholarly presentation and is fully adequate, in scope and quality, as a dissertation for the degree of Doctor of Philosophy.

Knox Millsaps
Professor and Chairman of Engineering Sciences

This dissertation was submitted to the Graduate Faculty of the College of Engineering and to the Graduate School, and was accepted as partial fulfillment of the requirements for the degree of Doctor of Philosophy.

April 1984

Dean, College of Engineering

Dean for Graduate Studies and Research